CIDER 2019 Lecture Notes: Magma Ascent in Conduits and Dikes

Helge M. Gonnermann, *Earth, Environmental and Planetary Sciences, Rice University*

Contents

1. Introduction

Magma ascent in conduits and dikes encompasses a plethora of complicating and mutually interdependent *parts*. A deeper understanding of magma ascent can be facilitated by numerical modeling. Although all models are wrong, in that they (hopefully) are a simplified or idealized representation of some parts of the natural *system*, models can be used to advance our understanding of how different *parts* affect one another and thereby affect magma ascent. Consequently, these lecture notes will take a *modeling centric* point of view.

The *system* that I will be considering herein is flowing (ascending) magma between its last storage reservoir prior to eruption and the (Earth's) surface. For the most part the magma pathway, which I will also refer to as the *conduit*, will be assumed fixed in geometry. Because we know too little about conduit geometry at depth, the conduit is often treated in a rather simplified and idealized manner. For example most magma ascent models assume a *conduit* that is equivalent to cylindrical pipe that may change in diameter with depth or a narrow slot of uniform width, which may change in the flow direction. Such assumptions have two advantages: (1) we don't pretend that we know more about conduit geometry than we do; and (2) we can reduce the mathematical aspects of modeling magma flow to a one-dimensional problem. That being said, recent models have explored feedbacks between magma flow and conduit geometry, for example by considering conduit walls that deform elastically in response to magma pressure or due to mechanical or thermal erosion/deposition by/of the flowing magma.

Another major challenge in magma ascent are the different scales that must be taken into consideration. Throughout these lecture notes I will use the following definition: *magma = mixture of silicate melt + exsolved magmatic volatiles (gas), usually as bubbles + crystals.* Thus, if we want to consider our *conduit system* overall, we have to consider processes that occur at the scale of $\sim 10^{-8}$ m, like bubble or crystal nucleation for example, and at the same time account for magma flow at the conduit scale at widths of ~1-10 m and lengths of $\sim 10^3 - 10^4$ m. This range of spatial scales represents a major challenge for understanding and integrative modeling of magma ascent.

2. Eruption styles

Magma ascent can result in a variety of *eruption styles*, which can be categorized based on observable quantities and underlying conditions. Any analysis or modeling of magma ascent in volcanic conduits and dikes needs to be motivated by well defined *objectives* and assumptions, which inform any analysis or modeling. The most fundamental distinction between volcanic eruptions is between *effusive*, that is non-explosive, and *explosive* eruptions. A key process in explosive eruptions is the *fragmentation*, or break-up, of magma. Fragmentation can occur at some depth within the conduit or close to the surface and remains an active area of research. A second broad distinction is between *basaltic* (*basic*) and *silicic* (*acidic*) eruptions, with a trend from basic to acidic magmas corresponding to decreasing temperatures, increasing viscosities, and decreasing temperatures. A second distinction is between explosive eruptions that are due to the interaction of meteoric water with magma, called *phreatomagmatic*, and eruptions that do not involve external water.

THE ROLE OF VISCOSITY

Viscosity affects magma ascent and eruption style in several fundamental ways:

- Can gas bubbles coalesce easily to form large bubbles (> 1 cm)?
- Can gas bubbles rise independently of the melt phase or are the *stuck* in the melt?
- Does magma fragment and how?
- Can bubbles grow easily or will the pressure of the gas inside bubbles remain high while the overall pressure decreases?

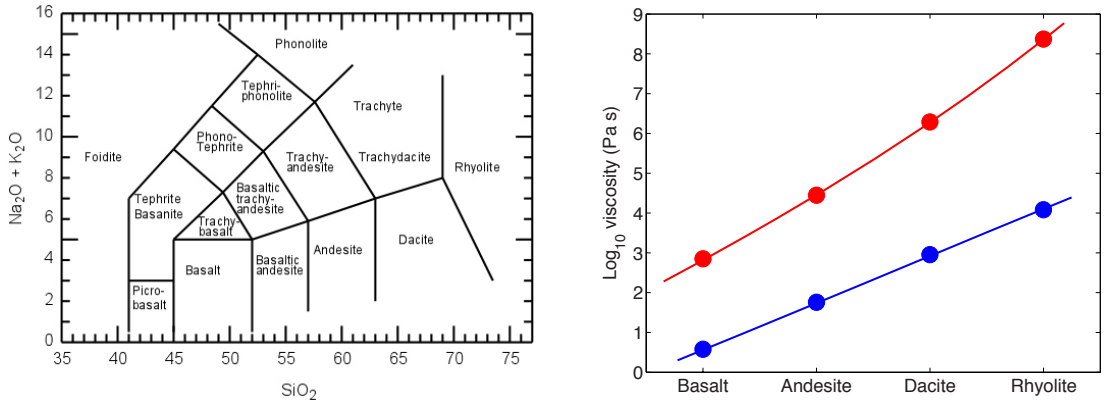

Figure 1

Left: Compositional fields of volcanic rocks in terms of total alkalis and silica, after Le Bas et al. [1986]. Units are wt.%. Basic rocks are from 45-52 wt.% SiO_2, ultrabasic are for < 45 wt.% SiO_2, acid are for > 63 wt.% SiO_2, and intermediate are for 52-63 wt.% SiO_2. **Right:** Viscosities of dry (0.1 wt.% H_2O, red) and wet (4 wt.% H_2O, blue) magmas from the Medicine Highlands (Medicine Lake Volcano), California (compositions from Eichelberger [1975]). Viscosity model of Hui and Zhang [2007] with assumed temperatures of 900, 1000, 1100, 1200 ^oC for rhyolite, dacite, andesite, basalt, respectively.

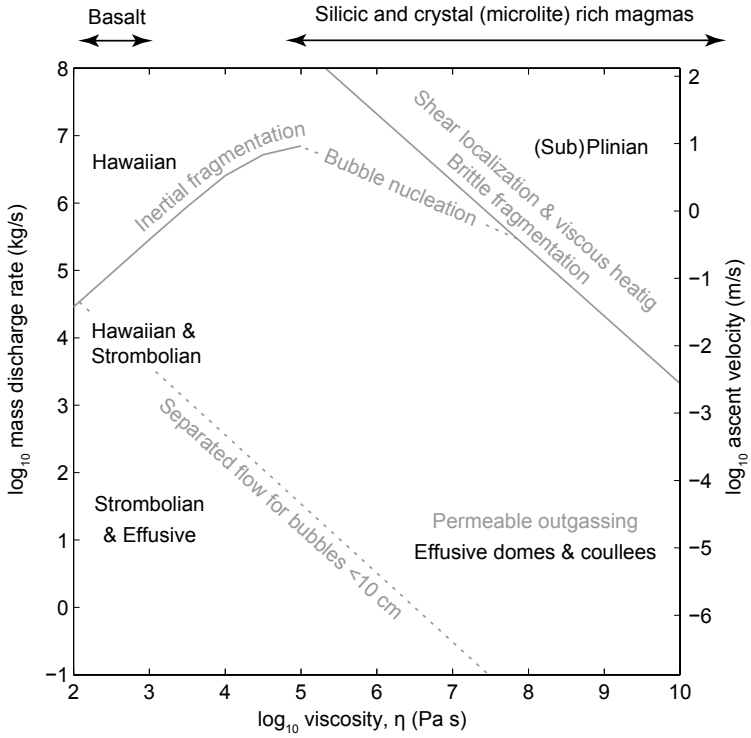

Figure 2

Figure 4.10 of Gonnermann and Manga [2013] summarizing the processes and mechanisms that govern the flow of magma in the volcanic conduit. Neglecting unsteady effects, discharge rate and viscosity control what processes have sufficient time to be dominant and affect eruption style.

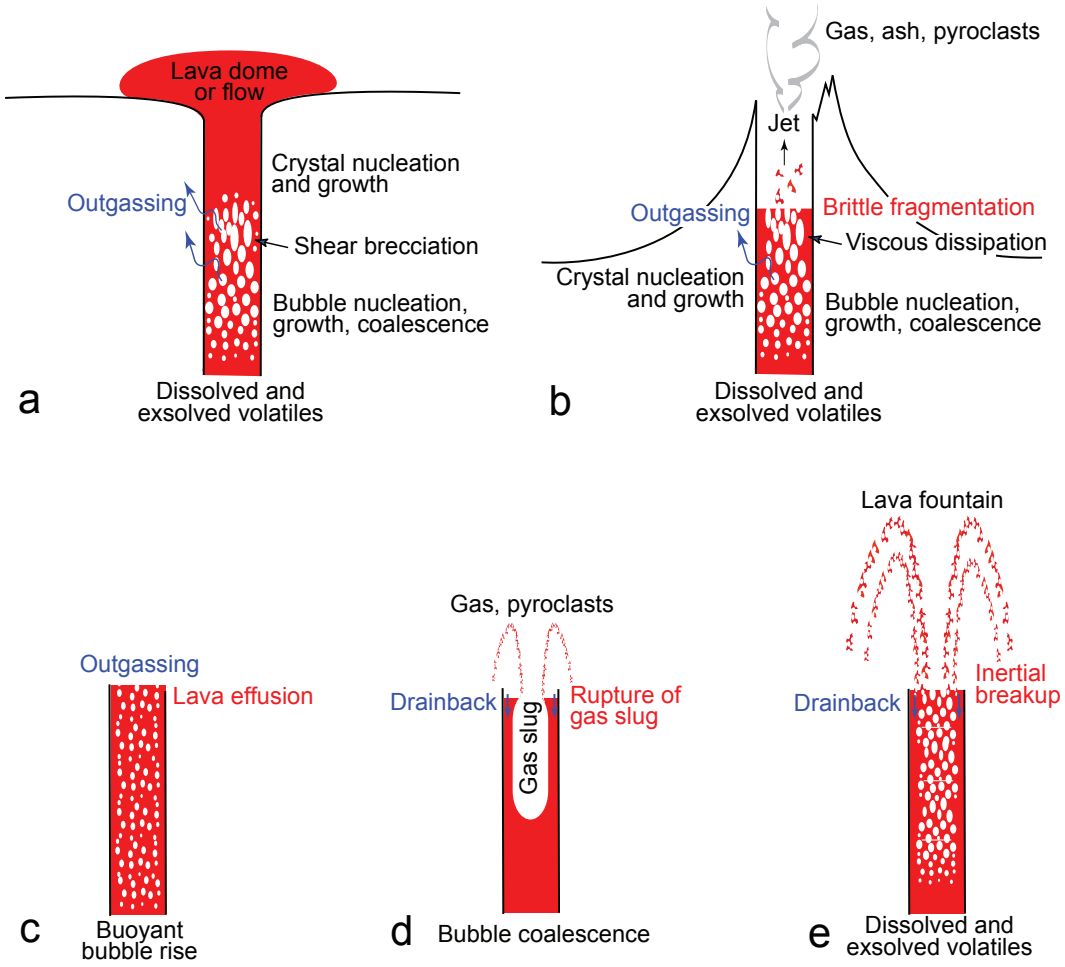

Figure 3

Figure 1 of Gonnermann and Manga [2013]. Schematic illustration of conduit processes. (a) In effusive eruptions of silicic magma (high viscosity & slow ascent rate) gas may be lost by permeable flow through porous and/or fractured magma. (b) During (sub)plinian eruptions bubble walls rupture catastrophically at the fragmentation surface and the released gas expands rapidly as the flow changes from a viscous melt with suspended bubbles to gas with suspended pycroclasts. (c) Extensive loss of buoyantly rising bubbles occurs during effusive eruptions of low-viscosity magma. (d) Coalesce and accumulation of buoyant bubbles, followed by their rupture at the surface, produces strombolian explosions. (e) Bubbles remain coupled to the melt in hawaiian eruptions, which are characterized by lava fountaining and hydrodynamic fragmentation.

2.1. Sizes of volcanic eruptions

The *Volcanic Explosivity Index (VEI)* attempts to describe different aspects of an eruption by a single number. Related scales are the *magnitude scale* and the *intensity scale*. The magnitude scale is defined as: $\text{magnitude} = \log_{10}(\text{erupted mass, kg}) - 7$, and the intensity scale is defined as $\text{intensity} = \log_{10}(\text{mass eruption rate, kg/s}) + 3$.

TABLE 13.1 Categories of the Volcanic Explosivity Index

Index	0	1	2	3	4	5	6	7	8
Bulk tephra volume (m^3)	$<10^4$	$<10^6$	$<10^7$	$<10^8$	$<10^9$	$<10^{10}$	10^{11}	$<10^{12}$	$>10^{12}$
Eruption plume column height (km)	<0.1	0.1–1	1–5	3–15	10–25	>25			
Qualitative description	Gentle	Effusive	Explosive		Cataclysmic, paroxysmal				
Stratospheric injection	None	None	None	Possible	Certain				
Percentage of known eruptions in the past 10,000 years	13	16	49	14	5	2	<1	<0.1	0
Typical recurrence interval	Days to weeks			0.3 years	3 years	20 years	80 years	500 years	7×10^5 years

Based on Newhall and Self (1982), Mason et al. (2004), Siebert et al. (2010), and Brown et al. (2014).

Figure 4

The Volcanic Explosivity Index (VEI) from Encyclopedia of Volcanoes, Second Edition, Table 13.1.

2.2. Eruptions of high-viscosity magma

- Dacite, rhyolite.
- Effusive silicic forming domes and coulees.
- Vulcanian, characterized by intermittent individual explosions at time intervals for minutes to years
- Subplinian
- Plinian and Ultraplinian

2.2.1. Effusive to explosive eruption of high-viscosity magma. High viscosity magma, such as andesite, dacite and rhyolite, may erupt effusively and/or explosively. Effusive eruptions may produce lava flows and domes with volumes of up to several km^3, whereas explosive eruptions may range from individual explosions (i.e., Vulcanian eruptions) to sustained explosive activity of variable intensity (i.e., subplinian, Plinian, ultraplinian).

FACTORS AFFECTING ERUPTION STYLE

Factors that affect eruption style and feed back upon one another are:

- Excess pressure in the magma chamber to overcome friction and force the magma up the volcanic "conduit". If this excess chamber pressure is small, relative to the pressure loss associated with magma flow, the magma may only ascend slowly, or perhaps not at all.
- Buildup of *overpressure* of gaseous bubbles to the point of exceeding the tensile strength of the magma, causing it to fragment. This may be possible if the magma ascends faster than bubbles can grow and allow the contained gases to decompress.
- Dissipation of gas pressure within bubbles by permeable gas flow, if the magma attains sufficient vesicularity and if magma ascent is sufficiently slow.
- Very large increases in magma viscosity as water exsolves at decreasing pressures.
- Very large increases in magma viscosity as the magma crystallizes, usually important if the magma ascends slowly.

2.2.2. Effusive eruption of high-viscosity magma. High-viscosity magma may erupt effusively if the excess chamber pressure (pressure in excess of magma-static or litho-static pressure) exceeds the frictional pressure

loss during magma ascent. In most cases effusive activity follows explosive eruptive activity, presumably because excess chamber pressure has been mostly depleted by magma withdrawal from the chamber during explosive activity. There are, however, eruptions where magma effusion is the principal eruptive style or where it is intermittently disrupted by Vulcanian explosive activity. It is thought that open-system magma degassing plays an important role in dissipating gas overpressure and thereby modulating explosive potential during effusive eruptions.

Figure 5

Little Glass Mountain rhyolite dome/flow (Medicine Lake Volcano, California) with Mount Shasta in the background.

Effusive eruption of high-viscosity magma usually produces lava domes or coulees. They may have stead or episodic growth, with emplacement times ranging from a few hours to many decades. Effusion rates may vary from less than 1 $m^3\ s^{-1}$ to more than 100 $m^3\ s^{-1}$. Some large domes have lava flows associated with them, which are referred to as *coulees*. Although lava domes grow slowly, they can become unstable and (partially) collapse. This exposes hot and pressurized magma from the interior to atmospheric conditions and can result in explosions and pyrcolastic density currents, both due to the explosion and from the collapsing part of the dome. Examples are Mount Unzen, Japan, and Soufriére Hills Volcano, Montserrat. These explosions have resulted in large numbers of deaths during the 20th century (e.g., 29,025 fatalities at Mt. Pelée, Martinique in 1902; approx. 1,000 fatalities at Santiaguito, Guatemala in 1929; 44 fatalities at Mt. Unzen, Japan in 1991; and 19 fatalities at Soufriére Hills, Montserrat in 1997).

The extruding magma can be highly crystalline and instead of flowing up the upper parts of the conduit, become extruded along shear fractures along the conduit perimeter. Consequently, dome structures can vary from steep-sided (Peléean or spiny domes) to more flattened and pancake-like. The surface structure of lava domes can be quite complex and include 10 to 15 m deep explosion pits, compression ridges, and crease structures. It has also been found that domes may be density-stratified, with more vesicular magma "trapped" beneath magma of low vesicularity (often containing large volumes of obsidian). This unstable stratification may result in the diapiric rise of some of part of the buoyant vesicular magma.

Figure 6

1060 C.E. eruption of Medicine Lake Volcano, California producing Glass Mountain rhyolite Plinian fall and flow.

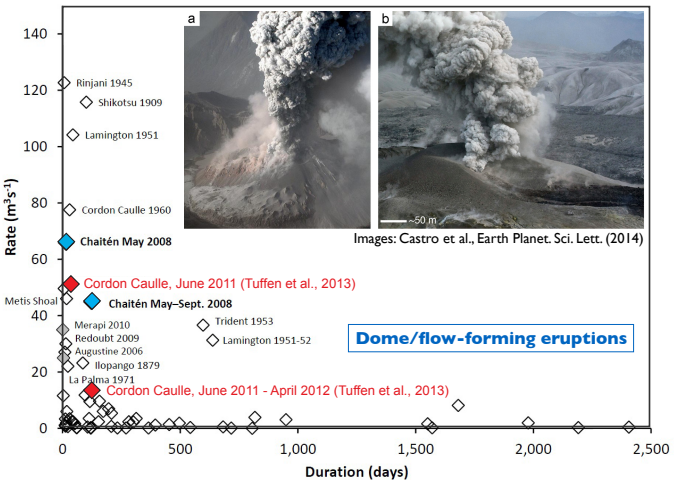

Figure 7

Modified after Pallister et al., J. Volcanol. Geotherm. Res., 2013. Images are from (a) Chaitén, Chile (2008) and (b) Cordón Caulle (2011/12) eruptions, showing simultaneous explosive-effusive activity following a Plinian eruptive phase.

2.2.3. Intermittent explosive eruption of high-viscosity magma. Vulcanian eruptions appear to fall between effusive and sustained explosive eruptive activity. One model for Vulcanian eruptions requires the formation of a high density and relatively impermeable plug in the upper parts of the volcanic conduit, perhaps even capped by a dome. This may sufficiently reduce magma ascent rates to where excess pressure builds up within the conduit and to where this plug/dome weakens over time until it fails catastrophically, resulting in Vulcanian explosions. A more detailed discussion of Vulcanian eruptions will be provided in a separate chapter.

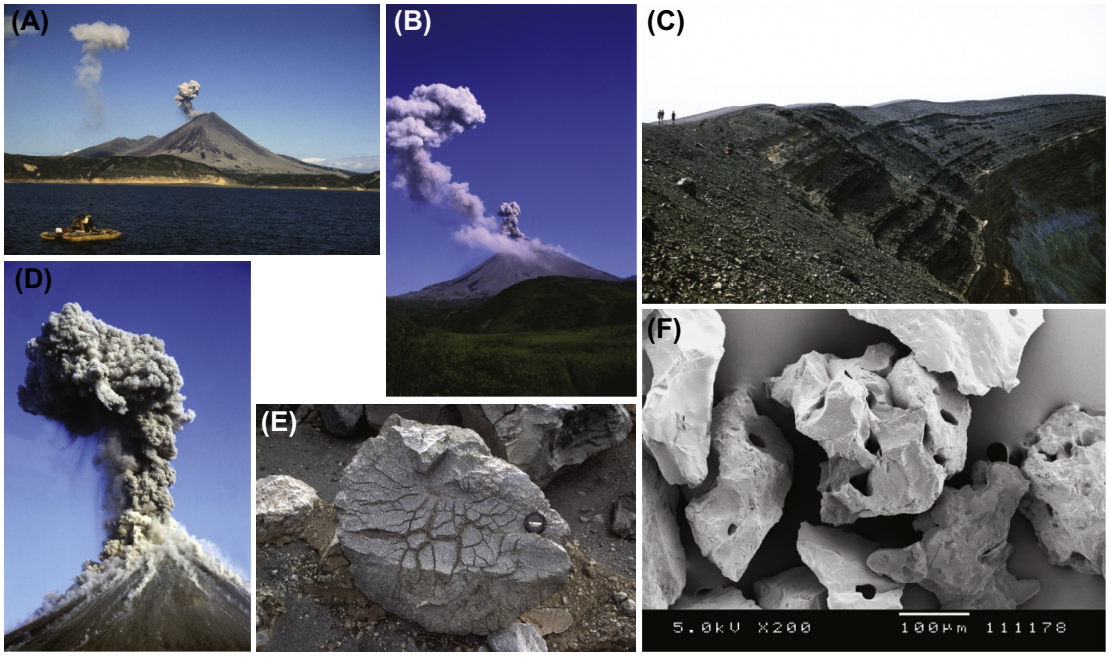

FIGURE 28.1 A) 1996 and (B) 2005 eruptions of Karymsky volcano. These consisted of frequent moderately strong explosions with few ballistics. Eruption cloud is approximately 1 km above the crater. Eruption clouds of previous explosions that occurred minutes before are drifting downwind; (C) Inner slope of the crater of Vulcano, Aeolian Islands, Italy. Multiple layers of bombs and lapilli were deposited by numerous transient explosions of the 1888−1890 eruptions; (D) Strongest Vulcanian-type explosions of Karymsky volcano, July 2004. Quickly rising eruption cloud is more than 1 km above the vent. Final height of the eruption cloud will be approximately 3 km. Massive ballistic fallout forms multiple hot avalanches on the volcano slope. A curtain of ash fallout is visible on the lee side of the eruption cloud; (E) Bread-crust bomb of Karymsky volcano, 1999. Lens cap is 6 cm across; (F) Scanning electron microscope image of ash particles of Karymsky volcano eruptions in 2003. Blocky sharp-edged particles with no/few gas bubbles indicate fragmentation of degassed highly viscous magma. *All photos by A. Belousov.*

Figure 8

Figure 28.1 from Encyclopedia of Volcanoes Second Edition.

2.2.4. Sustained explosive eruption of high-viscosity magma. Plinian type eruptions (including subplinian and ultraplinian) are characterized by the formation of high, convective eruption columns of magmatic gases, entrained ambient air and pyroclastic material. Dispersal by winds can be over large areas. During an eruption the style and *intensity* of the eruption can change within minutes, hours or days. Any period during which a given style is sustained is referred to an *eruption phase*. Pauses in explosive activity during a single eruption define *eruptive episodes*. Typically explosive eruptions are classified through their *pyrocalstic fall deposits*, that is the pyroclastic material that settles out from the eruption column. During explosive eruptions there may be sudden, violent explosions projected laterally or vertically, these are called *blasts*.

Pyroclastic fall deposits are different from *pyroclastic flow deposits*, which form as a consequence of *pyroclastic density currents*. The latter tend to be thickest in valleys and show sedimentary structures, such as cross bedding, whereas the former simply drape topography. Pyroclastic fall and flow deposits are frequently interstratified. Deposits from individual *eruption phases* are often identifiable based on grain-size stratification and ash layers between deposits from successive phases or *episodes*. Another term that is used for welded or unwelded, pumiceous, ash-rich pyroclastic density current deposits is *ignimbrite*, a term

that was formerly used for strongly welded deposits only. The term ignimbrite is essentially synonymous with *ash-flow tuff*.

TABLE 1 Main Features of Plinian-Type Eruptions

Type of eruption	*Subplinian*	*Plinian*	*Ultraplinian or ignimbritic*
Magnitude (kg)	$\approx 10^{11}$	10^{11}–10^{13}	$>10^{13}$
Intensity (kg/s)	$\approx 10^{6}$	10^{6}–10^{8}	$>10^{8}$
Column height (km)	<20	20–35	>35
Thickness half-distance (b_1, km)	0.5–4	2–10	>10
Clast half-distance (b_c, km)	1–3	3–8	8–15
Main phases	Unsteady sustained, convective column	Steady sustained convective column	Sustained fountaining
Associated eruptive styles	Surge generation, dome extrusion	Partial or total column collapse	Convective column with increasing flow rate
Dominant fallout deposits	Thinly stratified	Massive to variously graded	Generally reversely graded
Dominant flow deposits	Surges and small sized pumice and scoria flows	Pumice and ash flows	High and low-grade ignimbrites
Fall/flow vol. ratio	>1	>1	≪1
Typical magma composition	Mildly evolved (dacitic, phonotephritic)	Highly evolved (rhyolitic, trachytic, phonolitic)	Highly evolved (rhyolitic, trachytic)

Figure 9

Table 1 from Encyclopedia of Volcanoes chapter "Plinian and subplinian eruptions".

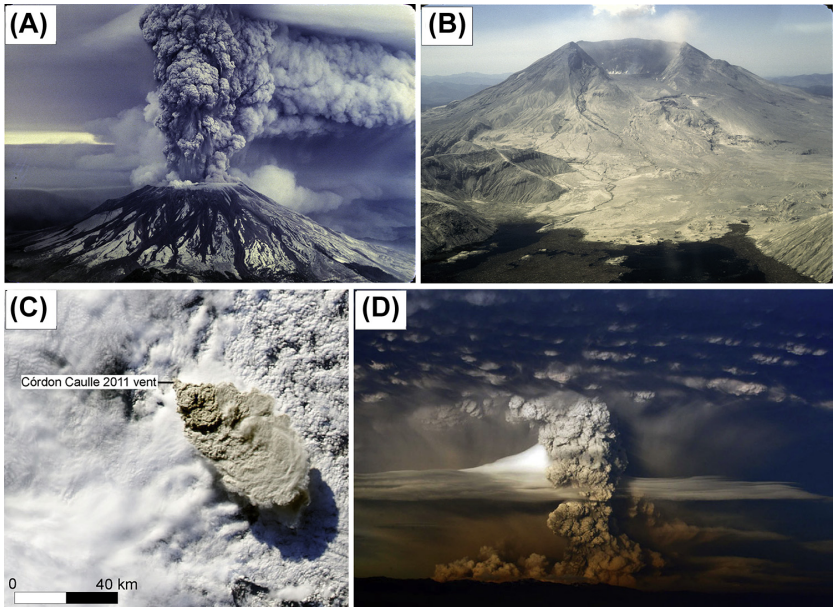

FIGURE 29.1 Eruption columns of plinian and suplinian eruptions. Mount St. Helens (USA) during (A) and immediately after (B) the 1980 eruption; (C) and (D) 2011 eruption of Puyehue-Córdon Caulle (Chile). Note in (D) contemporaneous convective and collapsing regimes with pyroclastic flow generation. *Photos (A) and (B) are by Richard G. Bowen, courtesy of the Bowen family. Picture (C) is courtesy of NASA.*

Figure 10

Figure 29.1 from Encyclopedia of Volcanoes 2nd Edition.

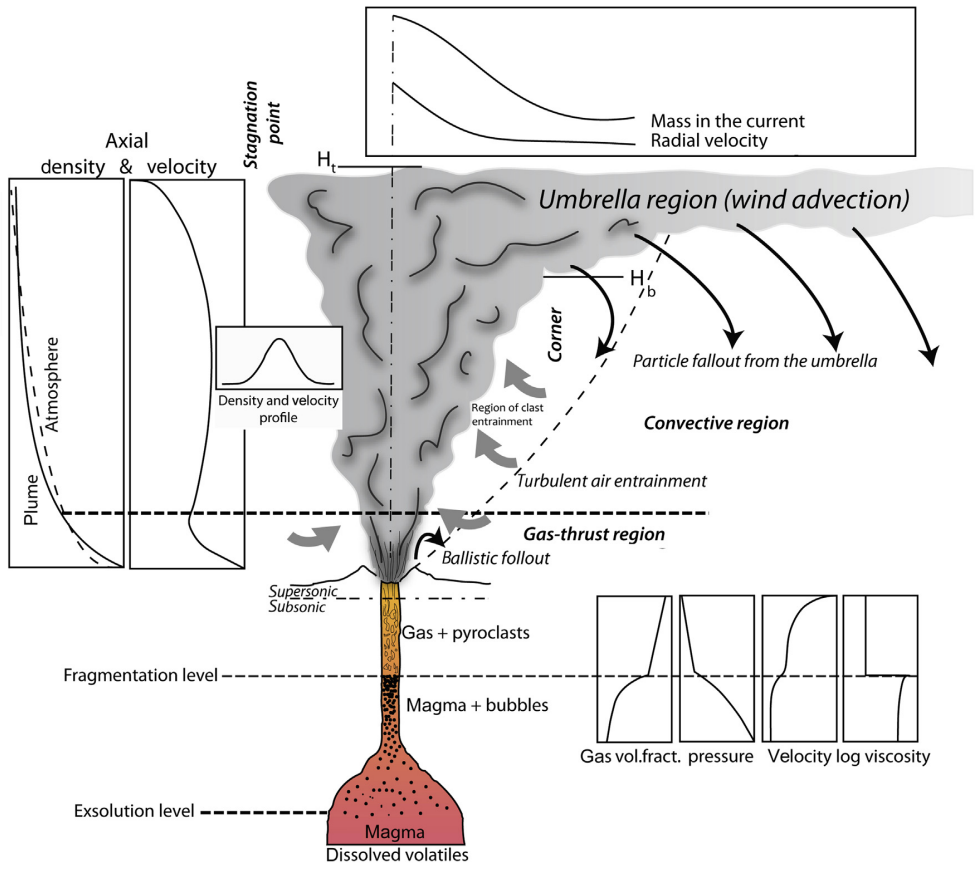

FIGURE 29.2 General scheme of eruptive regimes for a strong plume, and variation of physical parameters during plinian eruptions.
Figure 11

Figure 29.2 from Encyclopedia of Volcanoes 2nd Edition.

2.3. Eruptions of low-viscosity magma

MAIN CHARACTERISTICS OF LOW VISCOSITY ERUPTIONS

- Basalt.
- Magma flows easily, even if pressure gradients are small.
- Bubbles move independently of the melt.
- Bubbles can grow easily.
- Effusive, forming lava flows.
- Strombolian, intermittent individual explosions, often at time intervals of minutes.
- Hawaiian or also called fire fountain eruptions.
- Subplinian.

2.3.1. Effusive eruption of low-viscosity magma. Effusion of low viscosity lava usually results in lava flows. It is not uncommon to have simultaneous lava effusion at the base of cinder cones during Strombolian or Hawaiian fountaining activity.

2.3.2. Explosive eruption of low-viscosity magma. Basaltic explosive volcanism takes place over a range of scales and styles, from weak discrete *Strombolian explosions* ($10^2 - 10^3$ kg s^{-1}) to sustained *Hawaiian*

fountaining. Stromboli is the type location for mildly explosive Strombolian eruptions, which from 1999 to 2008 persisted at a rate of approximately 9 per hour, but were briefly interrupted in 2003 and 2007 by vigorous paroxysmal eruptions. Kilauea volcano, Hawaii, is a reference case for Hawaiian style fountaining activity. Both Strombolian and Hawaiin fountaining produce tephra cones, pyroclastic fall deposits. Hawaiian fountaining will also produce lava flows and/or lava lakes. Within the context of eruption styles, there is little doubt that a defining characteristic of Strombolian eruptions is the rapid and voluminous ascent of exsolved gas relative to a very low ascent rate of the melt phase. In contrast, Hawaiian, subplinian and Plinian eruptions require a more sustained and higher rate of magma supply to the conduit system.

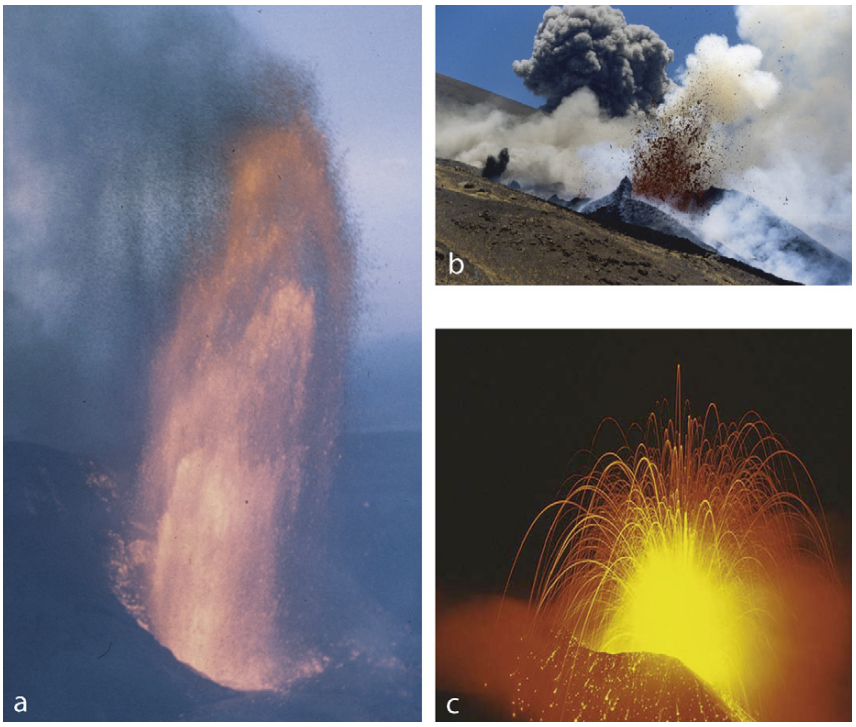

Figure 12

Figure 1 from Houghton and Gonnermann [2008] illustrating the diversity of basaltic explosive volcanism. (a) Kilauea Iki 1959, Episode 3. High fountaining eruption on 29 November 1959. Photograph Jerry Eaton. (b) Etna 20 July 2001 showing three contrasting styles of eruption from vents on the 2001 eruption fissure. In the foreground weak Strombolian explosions from the principal vent at 2100 m elevation. Weak phreatomagmatic activity occurs from an adjacent vent to the left (west). In the background the initiation of a more powerful phreatomagmatic explosion with subplinian dispersal at the 2500 m vent. Photograph Bruce Houghton. (c) Typical moderate intensity explosion of Stromboli, 23 July 2007. Photograph Tom Pfeiffer.

For sustained eruptions, and on time scales longer than or equal to eruptive episodes, changes in eruption intensity may be the manifestation of variations in magma supply from depth to the "shallow" magmatic plumbing system. For magma to erupt at the surface, sufficient excess pressure of magma within the source reservoir is required to overcome magma-static and dynamic pressure losses. Much of this excess pressure, or potential energy, is probably derived from volatiles. It is therefore likely that magma withdrawal, during eruptions and/or eruptive episodes, will result in pressure variations and, hence, variations in magma supply rate from shallow storage reservoirs to the conduit system and contrasts in eruption style. The ensuing dynamical coupling between magma source and conduit has been considered within various contexts for basaltic magmas.

In the case of fissure eruptions the large cross-sectional area of the vent results in comparatively high discharge rates at relatively low magma ascent rates. Conduit geometry may also play an important role in facilitating bubble accumulation, potentially of importance in Strombolian style eruptions. However, because of the poor constraints on conduit geometry, little work has been done on detailed assessments of its effect on the dynamics of basaltic eruptions in general

Volatiles are important, because exsolved gases are less dense than the melt, but more compressible. The former imparts buoyancy, whereas the latter can be viewed as potential buoyancy or potential energy.

Buoyancy from volatile exsolution ultimately allows magma to erupt. The relative importance of pre-eruptive volatile content versus syneruptive loss of volatiles is a key question to understanding the dynamics of explosive basaltic eruptions. However, to what extent systematic variations in pre-eruptive volatile content correlate with eruptive behavior remains largely unexplored within the broader context of eruption dynamics or explosivity. The most abundant volatiles in basalt magmas are H_2O, CO_2 and S. Volatile solubility in silicate melts is primarily pressure dependent, with secondary dependence on temperature and on melt composition, including other volatile species.

Bubble rise depends primarily on size, volume fraction and melt viscosity. Bubble size and volume fraction are expected to increase during ascent due to continued volatile exsolution, decompression and coalescence, which by themselves may affect flow dynamics. It is known that small perturbations in gas-liquid flow systems can lead to huge oscillations in flow rates and flow regimes. In the engineering literature four basic gas-liquid flow regimes have been identified: bubble flow, slug flow, churn flow and annular flow (Figure 13). While these flow regimes occur over a wide range of conditions, inconsistencies and open questions remain, especially in terms of applicability to basaltic eruptions, where length scales, viscosities and pressures exceed the conditions of most experimental investigations. Nonetheless, the general principles of gas-liquid flows should be instructive for the understanding of magmatic systems. For gas-liquid flow in vertical columns with low gas flow rates and small bubbles relative to the conduit

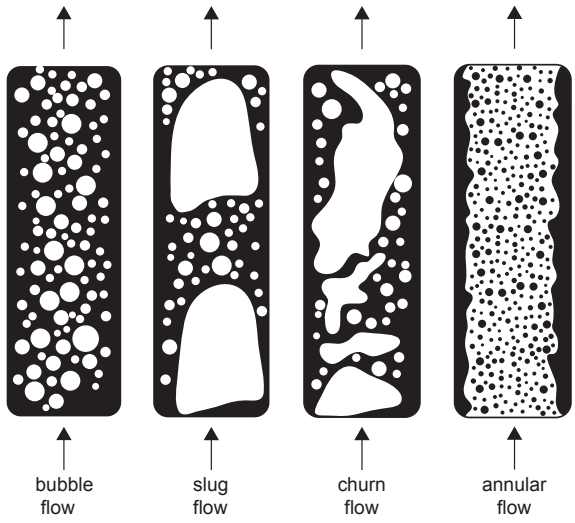

Figure 13

Figure 17 from Houghton and Gonnermann [2008] showing the flow regimes for vertically rising bubbly liquids after Taitel et al. (1980) and Guet and Ooms (2006).

diameter, bubbles are more or less randomly dispersed and move upward through the liquid phase without much dynamical interaction. This is called the bubbly flow regime. At higher gas flow rates, bubble number density is no longer uniformly distributed and hydrodynamic interactions can potentially affect the dynamics along the entire length of the conduit system. Originally it was thought that collisions between bubbles result in coalescence and ultimately to large bubbles of comparable size to the diameter of the conduit. These are generally referred to as gas slugs and the associated flow regime is called cap or slug flow. It was suggested that dispersed bubbly flow could be maintained if there is sufficient bubble break-up due to liquid turbulence to balance bubble coalescence (Taitel et al., 1980). More recently it was found that the transition to slug flow occurs simultaneously throughout the liquid column, implying that bubble coalescence and break-up are not the underlying mechanisms responsible for this flow transition. Instead, the bubble-to-slug transition may be associated with instabilities that form dynamically within the flow. In some conditions, bubbly flow passes directly to churn flow, which typically occurs at higher gas flow rates than slug flow. Void-fraction time series from laboratory experiments of slug and cap flow are suggestive of Strombolian eruptions, due to bubble coalescence or bubble accumulation, the latter perhaps enhanced or facilitated geometrically within the magmatic plumbing system.

Churn flow occurs at higher gas flow rates than slug flow. Unlike slug flow, it is characterized by neither phase being continuous, and by highly unsteady behavior. At gas flow rates that are at least 10 times larger than liquid flow rates, churn flow passes to annular flow, where the gas phase essentially occupies

almost the entire conduit and is surrounded by a relatively thin annulus of liquid along the conduit walls. Both churn and annular flow produce more sustained and vigorous flow conditions than slug flow. For churn and annular flow, the gas phase is continuous, albeit heterogeneously and somewhat intermittently, on length scales that approach the diameter of the conduit. It has been suggested that magma flow in the volcanic conduit during Hawaiian style eruptions is associated with annular flow, where it is assumed that annular flow is the consequence of bubble accumulation and coalescence at the roof of a shallow magma storage reservoir. More or less continuous collapse of this "foam" is then thought to give rise to a relatively continuous, high gas flux into the conduit system, capable of sustaining Hawaiian style magma jets for durations of hours. An alternative model suggest that for small bubbles and/or high magma ascent rates bubbles are unable to move appreciably relative to the melt phase, i.e., melt and bubbles are coupled. Consequently, the gas phase is dispersed throughout the magma producing a highly vesicular magma with relatively small bubbles. At some point the magma "disrupts" or "fragments" hydrodynamically, analogous to the breakup of a jet of water.

3. Approaches to modeling of magma ascent

The conventional approach to describing the *conduit system* is based on the continuum mechanics approach.

3.1. Conduit models in a nutshell

Solve the conservation equations for the values of the dependent variables as a function of depth (and if unsteady calculations as a function of time).

VARIABLES AND PARAMETERS

- Commonly used dependent variables:
  - Magma velocity, u
  - Magma pressure, p
  - Magma temperature, T
- Commonly calculated quantities:
  - Dissolved volatile concentration, c (from p)
  - Volume fraction of exsolved volatiles, ϕ_g (from c and T)
  - Volume fraction of crystals, ϕ_x (from c and T)
  - Magma density, ρ
  - Magma viscosity, μ (from c, T, ϕ_g, ϕ_x)
- Commonly specified values at inlet
  - Conduit size (e.g., radius, a)
  - Mass flow rate, Q ($u = Q/\pi a^2 \rho$)
  - Pressure
  - Dissolved volatile concentration
  - Volume fraction of bubbles and bubble number density
  - Volume fraction of crystals
  - Temperature
- Commonly specified values at exit
  - Pressure or choked flow

3.2. Further considerations

3.2.1. Phases. From here on we shall distinguish between three *phases*:

- Melt (subscript m)
- Exsolved volatiles/gas (subscript g)
- Crystals (subscript x)

3.2.2. Conservation equations for each phase.

- Conservation of mass
- Conservation of momentum
- Conservation of energy

3.2.3. Constitutive relations / micro-mechanical.

- Volatile solubility (e.g., H_2O, CO_2, S, halogens)
- Crystal nucleation
- Crystal growth
- Bubble nucleation
- Bubble growth
- Magma rheology
  - Dependence on composition
  - Dependence on volatile (H_2O) content
  - Dependence on temperature
  - Dependence on deformation rate
  - Dependence on bubbles
  - Dependence on crystals
- Open system with respect to gas
- Fragmentation

3.2.4. Typical simplifications.

- Geometry: in reality 3D, but often reduction to 2D or 1D
  - Neglect or approximate shear deformation and non-Newtonian rheology
  - Neglect viscous dissipation (shear heating)
- Isothermal: neglects viscous dissipation, volume changes, latent heat of vaporization/crystallization
- Steady state
- Highly parameterized crystallization
- No bubble nucleation
- No bubble coalescence
- Equilibrium solubility and bubble growth
- Treat magma as a mixture with average properties, as opposed to modeling each phase explicitly:
  - Homogeneous flow
  - Neglect pressure difference between gas and melt
  - Neglect potential separation of gas and melt phases due to bubble buoyancy or permeable gas flow
- Parameterized viscosity
- Parameterized fragmentation

3.2.5. The major classes of 1D conduit models.

- Steady homogeneous.
- Steady two-phase (gas-melt) with equal pressure for gas and melt.
- Steady homogeneous with diffusive bubble growth at the sub-grid scale.
- Transient two-phase (gas-melt) with different pressures for gas and melt.

3.2.6. Conduit geometry. Magma pathways, such as dikes, sills or volcanic *conduits* are in most cases probably not uniform cylindrical pipes or rectangular channels. If we knew the exact shape of magma pathways, we could and perhaps should model the flow of magma in it's three-dimensional complexity. Almost always, however, we have insufficient information to do so. Instead we have to resort to modeling magma flow through simplified (idealized) pathways of which cylindrical conduits (i.e., pipes) and narrow rectangular channels (i.e., dikes) are end members. Often we assume that such *conduits* remain uniform in shape and size throughout the flow domain, although in reality they probably change in size and shape along the flow direction and/or over time.

Most models are based on the approach of treating magma pressure as a dependent variable. For such models an exception to an assumed constant conduit size is the flaring of conduits in the shallow subsurface, due to the *choked* flow condition during explosive eruptions. In this case the pressure at the exit (surface) may be greater than atmospheric and also a dependent variable, as opposed to being specified (Figure 14). This will be discussed in more detail in the section on compressible flow. There is a class of models, however, going back to the work of Wilson [e.g., Wilson 1980b,a], that approaches the entire problem in terms of calculating the conduit size (diameter) for an assumed pressure profile - for example, near lithostatic - between reservoir and surface.

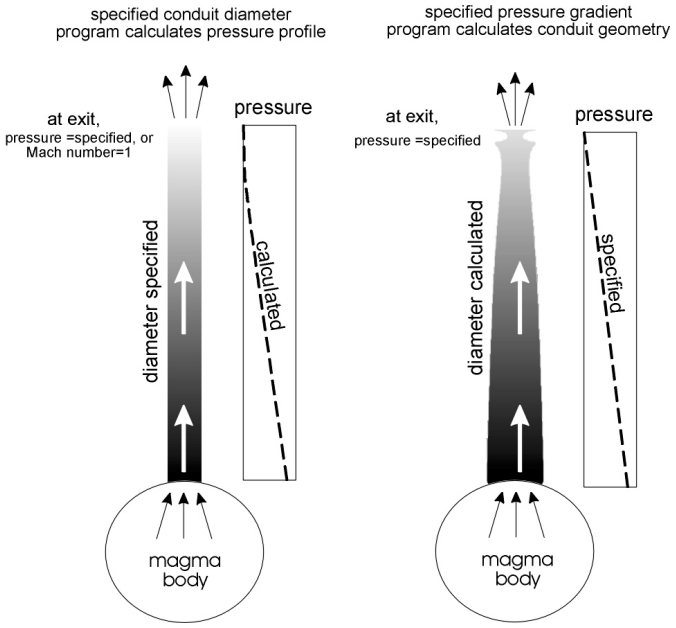

Figure 14

Figure 1 of Mastin and Ghiorso [2000] illustrating two options for calculating flow properties as a function of depth. **Left:** Conduit size (diameter) is specified and pressure is calculated. **Right:** Pressure is specified and conduit size is calculated.

There are also studies that explicitly explore the effect of a variable conduit size or shape with depth that is prescribed a priori. And there are studies that explore the effect of a change in conduit size due to erosion by the ascending magma, as well as due to elastic deformation of the wall rock by magma pressure. For the most part this subsequent discussion will assume an idealized conduit shape. This allows us to treat the flow as one-dimensional, accounting for potential complications such as non-laminar flow and non-Newtonian rheology through careful parameterization.

3.2.7. Steady flow. Another common simplification is that magma ascent is steady, which means that nothing changes over time. This assumption may be justified if changes with respect to time are slow, relative to the time it takes for magma to traverse the flow domain. For example, it may be justified to model a sustained explosive eruption as steady if the eruption overall changes (evolves) over hours and magma transit times between storage reservoir and surface are of the order of minutes. The same may

be justified for an effusive eruption if the time it takes for magma to travel between reservoir and surface is much shorter than the time over which eruptive activity changes significantly. In either case, small fluctuations in eruptive activity, such as discharge rate, are not accounted for, presumably because they are insignificant in terms of the questions that are being addressed by the modeling. As such, transitions in eruptive behavior - including the initiation of an eruption or its cessation - cannot be addressed through steady models. Nevertheless, steady models do allow an assessment of conditions that are associated with individual sustained eruptive periods.

3.2.8. Fully developed flow. Another aspect that tends to be neglected, in part because of the lack of observational constraints, is the transition region where magma enters the *conduit*. In this entry region, where the flow develops, assumptions about the velocity profile and viscous pressure losses based on a *fully developed flow* does not apply in a strict sense. Depending on model objectives, neglecting the region where the flow develops may be justified because it only represents a short distance relative to the entire pathway being modeled.

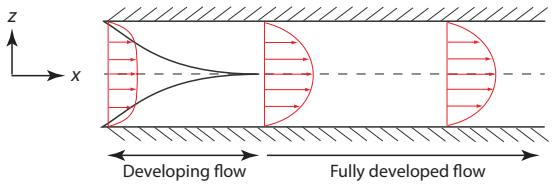

Figure 15

Schematic diagram illustrating the developing laminar flow profile at the entrance to a pipe.

SUMMARY OF MAIN COMPLICATIONS THAT MAY BE INCLUDED

- Volatiles other than H_2O
- Bubble nucleation
- Non-equilibrium bubble growth
- Bubble coalescence
- Two-phase gas-melt flow (bubble rise, permeable gas flow, outgassing)
- Crystallization
- Non-Newtonian magma rheology
- Fragmentation
- Shear heating
- Variable conduit size
- Unsteady

4. Steady homogeneous magma ascent in 1D

KEY POINTS

- Homogeneous flow: The gas phase is not treated separately from the melt phase. Instead average properties are assumed and equations for the *mixture* are solved. Gas and melt move together.
- Friction factor: Gradients in pressure (larger than magmastatic) balance viscous stresses and cause magma flow. Viscous forces can be parameterized using a *friction factor*.
- Conservation of momentum: This equation is integrated to give pressure as a function of depth.
- Mach number: The ratio of the flow velocity to the speed of sound within the material (fluid).
- Choked flow: If the magma fragments, the flow velocity of the gas-pyroclast mixture can reach the speed of sound, but it cannot exceed the speed of sound. Instead the conduit widens up toward the surface.

This is the simplest end-member for modeling of magma ascent. We assume that the magma can be treated as a single fluid with properties that account for the presence of bubbles and crystals, but without modeling gas and crystal as a separate phase. This assumes that the gas (bubbles) and crystals move with the magma, which may be justified if the melt viscosity and/or the magma ascent velocity are large. In the jargon of multi-phase fluid dynamics such flows are referred to as *homogeneous*.

4.1. Assumptions

For the details of how the conservation equations are derived I refer the interested reader to the lecture notes on *Conservation Equations*. Assuming the flow to be laminar and solely in the z-direction implies the following:

$$\begin{aligned} \partial/\partial t &= 0 \\ \partial/\partial \theta &= 0 \\ \tau_{zz} &= 0 \\ u_r &= 0 \\ u_\theta &= 0 \\ \partial P/\partial r &= 0 \\ \partial P/\partial \theta &= 0 \\ g_r &= 0 \\ g_\theta &= 0 \end{aligned} \tag{1}$$

4.2. Conservation of mass

Given these assumptions, conservation of mass is given by

$$\frac{\partial}{\partial z}\left(\rho u_z A\right) = 0, \tag{2}$$

where mass conservation was derived for a segment of the conduit whose cross-sectional area, A, may change with z.

4.3. Conservation of momentum - Part I

For conservation of momentum only the z-component of the Navier Stokes equation is non-zero, resulting in

$$\rho u_z \frac{\partial u_z}{\partial z} = -\frac{\partial P}{\partial z} - \frac{1}{r}\frac{\partial}{\partial r}\left(\mu r \tau_{rz}\right) - \frac{\partial}{\partial z}\left(\mu \tau_{zz}\right) - \rho g_z, \tag{3}$$

where

$$\tau_{rz} = -\mu \frac{\partial u_z}{\partial r} \tag{4}$$

and

$$\tau_{zz} = -2\mu \frac{\partial u_z}{\partial z} + \left(\frac{2}{3}\mu - \kappa \right) \frac{\partial u_z}{\partial z}. \tag{5}$$

Here κ is called the *dilational* or *bulk* viscosity. In most conduit models τ_{zz} is neglected and the effect of viscosity in the momentum balance is considered in terms of shear stresses τ_{rz} in the case of laminar flow. If the flow is turbulent, viscous stresses are accounted for using a *friction factor*.

4.4. Friction factor

4.4.1. Friction factor for a cylindrical conduit. For a steadily driven flow of a fluid of constant density in a straight conduit of uniform cross section or around a submerged object that has an axis of symmetry parallel to the flow direction, there is a force, $\mathbf{F}$, that points in the opposite direction as the average fluid velocity, u. This force is proportional to a characteristic area, A, and a characteristic kinetic energy, K, per unit volume [Bird et al. 1960]

$$F = AKf_F, \tag{6}$$

with the proportionality constant, f_F, called the *Fanning friction factor*. For flow in conduits A is usually taken to be the wetted surface of the conduit, $A = 2\pi aL$, and

$$K = \frac{1}{2}\rho u^2 \tag{7}$$

Here F/A can be viewed as the shear stress at the conduit wall, τ_w, due to the moving fluid, so that

$$\tau_\mathrm{w} = \frac{1}{2}\rho u^2 f_F. \tag{8}$$

Generally it is not $\mathbf{F}$ that is measured in experiments, but rather the difference in non-hydrostatic pressure, $\Delta p = (p_1 - p_0)$ over some length of conduit, L, hence,

$$\mathbf{F} = \pi a^2 \Delta p. \tag{9}$$

Equating these two equations for $\mathbf{F}$ gives

$$\frac{\Delta p}{L} = \frac{2\rho u^2}{D} f_F, \tag{10}$$

where D is the conduit radius. For time-averaged flow $f_\mathrm{F} = f_\mathrm{F}(\mathrm{Re}, L/D)$, where $\mathrm{Re} = \rho u D/L$ is the Reynolds number. The dependence of f_F on L/D arises form the development of the velocity distribution as the fluid enters the conduit, which occurs over lengths of $\approx (0.03D\mathrm{Re})$. For conduits that are much longer, $f_\mathrm{F} = f_\mathrm{F}(\mathrm{Re})$. For laminar flow in a cylindrical conduit, that is $\mathrm{Re} < 2100$,

$$f_\mathrm{F} = \frac{16}{\mathrm{Re}}. \tag{11}$$

Unfortunately there is an alternate definition of the friction factor, called the *Darcy-Weissbach friction factor* denoted as f_D, and the two are easily confused. Note that

$$f_\mathrm{D} = 4f_\mathrm{F} = \frac{64}{\mathrm{Re}} \tag{12}$$

for laminar flow in a cylindrical conduit.

For turbulent flow there is no simple analytical expression, but rather formulas have been developed based on extensive experimental data, which are conveniently summarized in the *Moody Chart*, shown in Figure 17.

As already mentioned, there are a number of formulations for the friction factor under turbulent flow conditions. One of the better known ones is the Colebrook equation [Colebrook 1939] given by

$$\frac{1}{\sqrt{f_D}} = -2.0 \log_{10} \left(\frac{\epsilon/D}{3.7} + \frac{2.51}{\mathrm{Re}\sqrt{f_D}} \right), \tag{13}$$

where ϵ is the surface roughness, that is the average height of deviations from a smooth wall. It is important to emphasize that the data upon which most friction factor equations are based are for fully developed steady flow in a circular pipe. It is justifiable to use these friction factors for unsteady flows, if the flow is changing slowly.

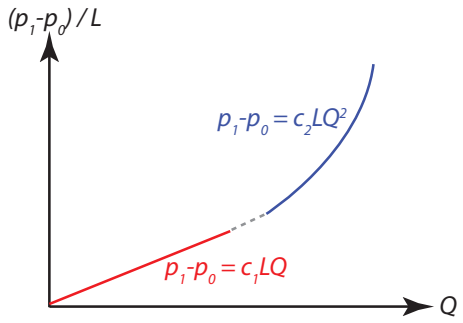

Figure 16

The pressure drop, $p_1 - p_0$, in a horizontal pipe of length, L, at different flow rates, Q. If flow rates are low, pressure gradient is directly proportional to flow rate. In this case the flow is laminar. For intermediate flow rates, the results are irreproducible and alternate "randomly" between low and high flow rate scalings. This is the transitional regime from laminar to turbulent flow. At high flow rates, the pressure gradients is approximately proportional to the square of the flow rate. This is the turbulent flow regime.

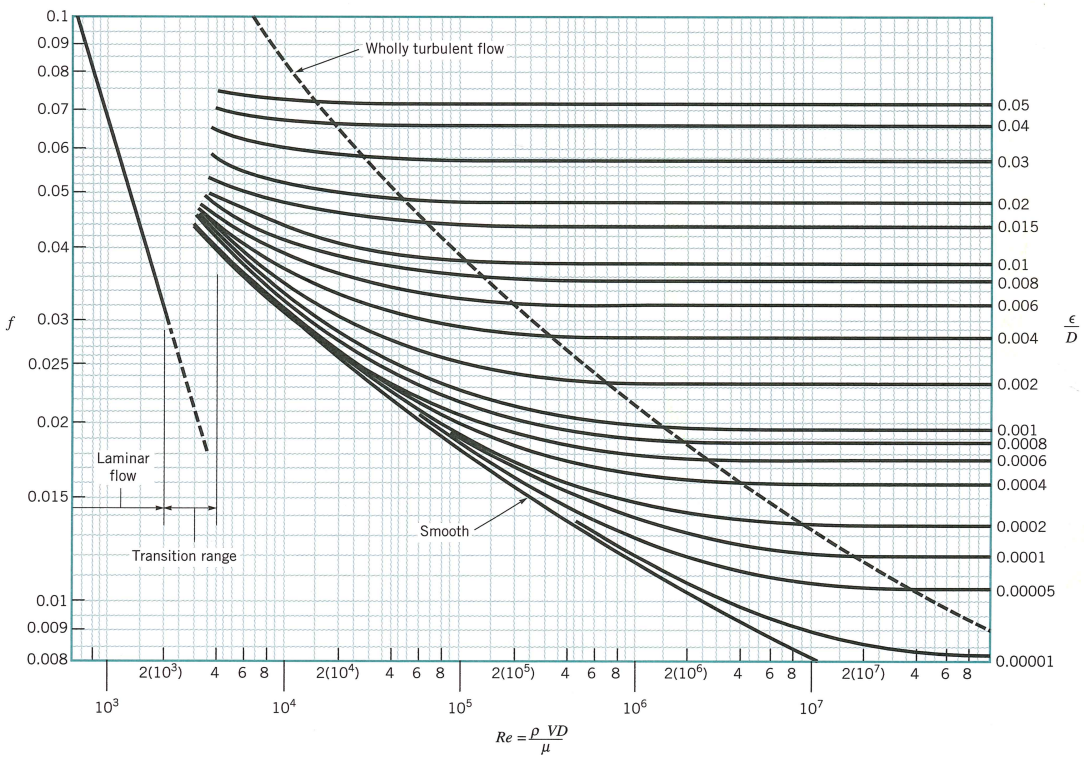

Figure 17

Figure 8.20 of Munson et al. [1998]. The Moody chart, which gives the friction factor, f_D, as a function of Reynolds number, Re, and relative roughness, ϵ/D for round pipes.

4.4.2. Friction factor for non-cylindrical conduits. For laminar flow in a rectangular fracture of large aperture

$$\frac{f_{\text{fracture}}}{f_{\text{pipe}}} \approx 12\frac{(a+b)}{a} \tag{14}$$

is often used, where b is the half-width of the fracture and a the half-length perpendicular to the width. More general formulations exist, for example Muzychka and Yovanovich [2009] suggest for rectangular conduits

$$f_F \mathrm{Re}_{\sqrt{A}} = \frac{12}{\sqrt{b/a}\,(1+b/a)\,[1-(192\,b/a\pi^5)\tanh\{\pi a/2b\}]}. \tag{15}$$

with limits

$$f_F \, \mathrm{Re}_{\sqrt{A}} \approx \begin{cases} 14.13, & b/a \to 1 \\ \dfrac{12}{\sqrt{b/a}}, & b/a \to 0. \end{cases} \tag{16}$$

Here the Reynolds number is based on the length scale $\sqrt{A}$, which is the square root of the conduit's cross-sectional area, A. For elliptical conduits Muzychka and Yovanovich [2009] suggest

$$f_F \mathrm{Re}_{\sqrt{A}} = \frac{2\pi^{3/2}\left[1+(b/a)^2\right]}{\sqrt{b/a}\,\mathbf{E}\left\{\sqrt{1-(b/a)^2}\right\}}, \tag{17}$$

where $\mathbf{E}\{\cdot\}$ denotes the complete elliptical integral of the second type, and

$$f_F \, \mathrm{Re}_{\sqrt{A}} \approx \begin{cases} 14.18, & b/a \to 1 \\ \dfrac{11.14}{\sqrt{b/a}}, & b/a \to 0. \end{cases} \tag{18}$$

For fully developed turbulent flows in non-circular conduits (ducts) Duan et al. [2012], for example, suggest the following equation

$$f_F = \left[3.6 \log\left(0.2047\left(\frac{\epsilon}{\sqrt{A}}\right)^{10/9} + \frac{6.115}{\mathrm{Re}_{\sqrt{A}}}\right)\right]^{-2}. \tag{19}$$

This formulation appears robust to within 6% of experimental data across a wide range of conduit shapes and aspect ratios.

FRICTION FACTOR IN PRACTICE

In modeling of magma flow the Reynolds number may vary substantially during any given simulation. Furthermore, there tends to be substantial uncertainty about the shape, size and roughness of the conduit. Therefore a convenient approximation to f is

$$f = f_0 + f^*. \tag{20}$$

In the case of cylindrical conduits, for example, $f_0 = 64/\mathrm{Re}$ (for Darcy-Weisbach), $f_0 = 16/\mathrm{Re}$ (for Fanning), and f^* is take as the asymptotic value at large Re for some assumed value of wall roughness.

4.5. Conservation of momentum - Part II

Substituting the friction factor into Equation (3) and dropping the subscript z gives

$$\rho u \frac{du}{dz} = -\frac{dP}{dz} - \frac{\rho u^2 f_F}{a} - \rho g, \tag{21}$$

where a is the radius of the (spherical) conduit and u is the average vertical velocity. Note that we no longer need to use partial derivatives. Expanding the continuity equation in terms of du/dz and substituting in the momentum equation gives upon rearranging

$$-\frac{dP}{dz} = \rho g + \frac{\rho u^2 f_F}{a} - \frac{\rho u^2}{A}\frac{dA}{dz} - u^2\frac{d\rho}{dz} \tag{22}$$

It is important to note that we have assumed that du/dz, is not negligible, which has implications for τ_{zz}. The last term in Equation (22) allows for the expansion of the ascending magma due to bubble nucleation and/or growth, although in principle it could also account for the compaction of magma due to differential motion of the gas phase relative to the melt. We can rewrite this term as

$$\frac{d\rho}{dz} = \left(\frac{\partial \rho}{\partial P}\right)_{\mathrm{S}} \frac{dP}{dz}, \tag{23}$$

where the partial derivative $(\partial\rho/\partial P)_S$ is taken at constant entropy. In the simplest case of homogeneous mixture of gas bubbles dispersed in the melt (or vice versa) the value of $(\partial\rho/\partial P)_S$ can be obtained from volatile solubility and the equation of state for the gas phase. An important definition is

$$\left(\frac{\partial\rho}{\partial P}\right)_S \equiv \frac{1}{c^2}, \tag{24}$$

where c is the sound speed of the gas-liquid mixture (see lecture notes on Compressible Flow for more details). We thus rewrite Equation (22) as

$$-\left(1-\frac{u^2}{c^2}\right)\frac{dP}{dz} = -\left(1-M^2\right)\frac{dP}{dz} = \rho g + \frac{\rho u^2 f_F}{a} - \frac{\rho u^2}{A}\frac{dA}{dz}, \tag{25}$$

where $M \equiv u/c$ is the *Mach number*. This equation can be integrated to give pressure as a function of depth, where u can be obtained from the assumed constant mass flow rate of Equation (2) and if dA/dz is zero or known otherwise. During explosive eruptions the flow of the gas pyroclast mixture above fragmentation is a *compressible flow*, for which there are constraints on the Mach number, discussed next.

4.6. Compressible flow

4.6.1. Energy equation. For further details on the derivation of the Energy equation, see *Lecture Notes: Conservation Equations*. The first law of thermodynamics states that the change in the internal energy of a closed system is equal to the amount of heat supplied to the system, minus the amount of work done by the system on its surroundings. For a control volume fixed in space it is given by

$$\underbrace{\frac{d}{dt}\int \rho\left(e+\frac{u^2}{2}\right)dV}_{\text{Change in stored energy}} + \underbrace{\int\left(e+\frac{u^2}{2}\right)\rho u_j dA_j}_{\text{energy flux out}} = \underbrace{\int u_i\tau_{ij}dA_j}_{\text{rate of work done on surface}} - \underbrace{\int \mathbf{q}\cdot d\mathbf{A}}_{\text{heat flux in}}, \tag{26}$$

where e **is the internal energy** per unit mass, which in the Lecture Notes on Conservation Equations was denoted as U_e, and $u^2/2$ **is the kinetic energy** per unit mass. $\mathbf{q}$ is the heat flux across surface area $\mathbf{A}$. The first term on the left-hand side represents the change of *stored energy*, which is the sum of internal and kinetic energies within the control volume. The second term on the left-hand side represents the flux of energy out of the control volume. The first term on the right-hand side represents the rate of work done on the control surface (i.e., shear stress due to *friction*). The second term on the right hand side represents heat input *through* the control *surface*.

Assuming steady state ($d/dt = 0$) and defining $\dot{m} = \rho_1 u_1 A_1 = \rho_2 u_2 A_2$ gives

$$\int\left(e+\frac{u^2}{2}\right)\rho u_j dA_j = \dot{m}\left[e_2+\frac{1}{2}u_2^2 - e_1 - \frac{1}{2}u_1^2\right]. \tag{27}$$

Neglecting frictional stresses

$$\int u_i\tau_{ij}dA_j = u_1p_1A_1 - u_2p_2A_2. \tag{28}$$

Neglecting any external heat addition or loss (i.e., adiabatic), we obtain

$$e_2+\frac{1}{2}u_2^2 - e_1 - \frac{1}{2}u_1^2 = \frac{1}{\dot{m}}\left[u_1p_1A_1 - u_2p_2A_2\right] \tag{29}$$

Defining the specific volume $v \equiv 1/\rho$, which has units of m^3/kg gives

$$\frac{uA}{\dot{m}} = v \tag{30}$$

and

$$e_2+\frac{1}{2}u_2^2 - e_1 - \frac{1}{2}u_1^2 = p_1v_1 - p_2v_2. \tag{31}$$

Here p_1v_1 is the work done (per unit mass) by the surroundings in pushing fluid into the control volume. Similarly, p_2v_2 is the work done by the fluid inside the control volume on the surroundings by pushing fluid out of the control volume.

ENTHALPY AND CONSERVATION OF ENERGY

Defining enthalpy as

$$h \equiv e + pv, \tag{32}$$

gives for the conservation of energy (under aforementioned assumptions)

$$h_2 + \frac{1}{2}u_2^2 = h_1 + \frac{1}{2}u_1^2. \tag{33}$$

This equation states that the sum of enthalpy and kinetic energy remains constant in an adiabatic (no heat leaves or enters the system) flow. Relative to a *static* system, in a flowing system *flow work*, pv, is required to push matter across the surface of a control volume.

4.6.2. Effect of friction in constant-area conduits. Define the following: $M_{\text{upstream}} \equiv M_1$ and $M_{\text{downstream}} \equiv M_2$. Assuming steady state, the equations of mass, momentum and energy conservation are given by

$$p_1 u_1 = p_2 u_2 \tag{34}$$

$$p_1 + \rho_1 u_1^2 = p_2 + \rho_2 u_2^2 + p_1 f \tag{35}$$

$$h_1 + \frac{1}{2}u_1^2 + h_1 q = h_2 + \frac{1}{2}u_2^2, \tag{36}$$

where f is a dimensionless friction parameter and q is a dimensionless heating parameter. Assuming a perfect gas and using the relations $c = \sqrt{\gamma RT}$ and $M = u/c$ and $p = \rho RT$

$$\rho u^2 = p\gamma M^2. \tag{37}$$

Thus, writing the momentum equation in terms of M gives

$$p_1\left(1 + \gamma M_1^2 - f\right) = p_2\left(1 + \gamma M_2^2\right), \tag{38}$$

or

$$\frac{p_1}{p_2} = \frac{\left(1 + \gamma M_2^2\right)}{\left(1 + \gamma M_1^2 - f\right)}. \tag{39}$$

Furthermore, using the relations $c = \sqrt{\gamma RT}$ as well as $M = u/c$ with $p = \rho RT$ and $h = \gamma p/\rho(\gamma - 1)$ gives

$$u^2 = \gamma M^2 RT = \gamma M^2 p/\rho = h(\gamma - 1)M^2 \tag{40}$$

and thus

$$h_1\left(1 + \frac{\gamma - 1}{2}M_1^2 + q\right) = h_2\left(1 + \frac{\gamma - 1}{2}M_2^2\right), \tag{41}$$

or

$$\frac{h_1}{h_2} = \frac{1 + (\gamma - 1)M_2^2/2}{1 + (\gamma - 1)M_1^2/2 + q}. \tag{42}$$

Conservation of mass,

$$\frac{\rho_1}{\rho_2} = \frac{u_2}{u_1}, \tag{43}$$

together with the equation of state give

$$\frac{p_1 RT_2}{p_2 RT_1} = \frac{u_2}{u_1} \tag{44}$$

or

$$\frac{p_1}{p_2} = \frac{u_2}{u_1}\frac{\gamma RT_1}{\gamma RT_2} = \frac{u_2}{u_1}\frac{c_1^2}{c_2^2} = \frac{u_1}{u_2}\frac{M_2^2}{M_1^2}. \tag{45}$$

Using $h = \gamma p/\rho(\gamma - 1)$, together with conservation of mass gives

$$\frac{h_1}{h_2} = \frac{\rho_2 p_1}{\rho_1 p_2} = \frac{u_1 p_1}{u_2 p_2} \tag{46}$$

and substituting from the previous relation

$$\frac{h_1}{h_2} = \frac{\rho_2 p_1}{\rho_1 p_2} = \frac{u_1^2 M_2^2}{u_2^2 M_1^2} \tag{47}$$

or

$$\left[\frac{h_1}{h_2}\right]^{1/2} = \frac{u_1}{u_2}\frac{M_2}{M_1}. \tag{48}$$

Combining the expressions for h and p with our momentum and energy equations gives

$$\frac{u_1}{u_2} = \frac{M_1^2}{M_2^2}\frac{\left(1+\gamma M_2^2\right)}{(1+\gamma M_1^2 - f)} \tag{49}$$

and

$$\frac{u_1}{u_2} = \frac{M_1}{M_2}\left[\frac{1+(\gamma-1)M_2^2/2}{1+(\gamma-1)M_1^2/2+q}\right]^{1/2}. \tag{50}$$

Combining both equations gives

$$\frac{M_1^2}{M_2^2}\frac{\left(1+\gamma M_2^2\right)}{(1+\gamma M_1^2 - f)} = \frac{M_1}{M_2}\left[\frac{1+(\gamma-1)M_2^2/2}{1+(\gamma-1)M_1^2/2+q}\right]^{1/2} \tag{51}$$

or

$$\frac{M_2}{M_1} = \left[\frac{\left(1+\gamma M_2^2\right)}{(1+\gamma M_1^2 - f)}\right]\cdot\left[\frac{1+(\gamma-1)M_1^2/2+q}{1+(\gamma-1)M_2^2/2}\right]^{1/2}. \tag{52}$$

Bringing M_2 to the left-hand side and assuming q and f are specified, along with M_1, gives

$$\frac{M_2^2\left[1+(\gamma-1)M_2^2/2\right]}{\left(1+\gamma M_2^2\right)^2} = \frac{M_1^2\left[1+(\gamma-1)M_1^2/2+q\right]}{\left(1+\gamma M_1^2 - f\right)^2} \equiv A \tag{53}$$

This is a biquadratic equation for M_2 with the solution

$$M_2^2 = \frac{-(1-2A\gamma) \pm \left[1-2A(\gamma+1)\right]^{1/2}}{(\gamma-1)-2A\gamma^2}, \tag{54}$$

which is plotted in Figure 18 for $q = 0$. For an equivalent figure in terms of q with $f = 0$, the reader is referred to Kundu & Cohen, *Fluid Mechanics*, or other texts dealing with compressible flow.

Case: $M_1 < 1$ For $M_1 < 1$, friction requires that p decreases with x. As p decreases, so does ρ, which requires that u increases. Consequently, M increases as well.

Once subsonic always subsonic

- It is not possible to go from $M_1 < 1$ to $M_2 > 1$, because it requires that entropy decreases.
- For volcanic eruptions it stands to reason that at depth $M < 1$, therefore at the exit (vent) $M \leq 1$. In the case of $M = 1$ the flow is called *choked*.

Case: $M_1 > 1$ For $M_1 > 1$ two solutions are possible: One for which $1 < M_2 < M_1$. In this case u decreases, whereas p and ρ increase downstream. The other solution is $M_2 < 1$. The two solutions coalesce when $M_2 = 1$, at which the flow is choked.

Supersonic to subsonic

- Pass from $M_1 > 1$ to $M_2 < 1$ via $M_2 = 1$.
- At $M_2 = 1$ the maximum mass flow rate is reached.

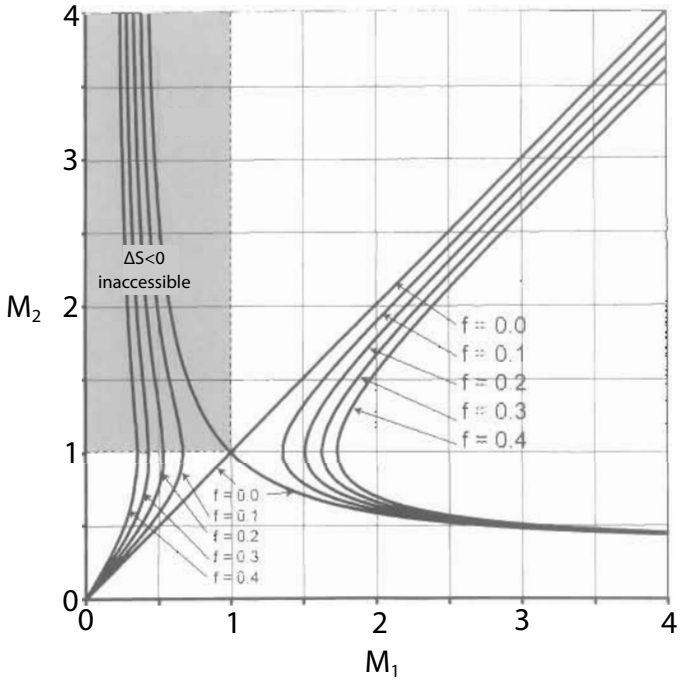

Figure 18

Flow in a constant-area duct with friction, f as parameter and $q = 0$. Upper left shaded quadrant is inaccessible because the change in entropy is < 1. Copied from Kundu & Cohen, *Fluid Mechanics*.

4.7. Conservation of momentum - Part III

In most volcanically realistic cases $M < 1$ at depth, but $M \to 1$ as the magma reaches shallow depths, low pressures and correspondingly high gas fractions. To avoid physically unrealistic solutions or singularities as $M \to 1$, the right hand side of Equation (25) must approach zero, which leads to the following condition

$$\rho g + \rho u^2 \frac{f_F}{a} = \frac{\rho u^2}{A}\frac{dA}{dz} = \frac{2\rho u^2}{a}\frac{da}{dz} \tag{55}$$

or equivalently

$$\frac{da}{dz} = \frac{1}{2}\left(\frac{ga}{u^2} + f\right). \tag{56}$$

Because the right-hand side of Equation (56) is always positive, the vent must be widening in the upward direction as $M \to 1$. The flow, if it does indeed approach $M = 1$ at the vent is called *choked*. Depending on pressure at the based of the conduit and pressure losses within the conduit, the exit pressure may be greater than atmospheric. In this case the erupting gas-pyroclast mixture will equilibrate to atmospheric pressure above the vent through a series of shock waves.

CHOKED FLOW

- Choked flow refers to an upward widening conduit with $M = 1$ at the exit.
- If exit pressure is greater than 1 atm, there will be expansion waves above the vent.

4.8. The speed of sound for a gas-pyroclast mixture

The speed of sound of a multiphase mixture (i.e., gas, liquid, solid) is given by

$$c^2 = \frac{K}{\rho}, \tag{57}$$

where K is the bulk modulus. For a multiphase fluid consisting of gas, melt and crystals of volume fractions ϕ_g, ϕ_m and ϕ_x, respectively,

$$\frac{1}{K} = \frac{\phi_g}{K_g} + \frac{\phi_m}{K_m} + \frac{\phi_x}{K_x}. \tag{58}$$

For and ideal gas the isothermal and isentropic bulk moduli are, respectively,

$$K_T = P \tag{59}$$

and

$$K_S = \gamma P. \tag{60}$$

Neglecting compressibility of melt and crystals (i.e., $K_m = K_x = \infty$) and assuming isothermal conditions the speed of sound of a gas-pyroclast mixture can be approximated as

$$c^2 \approx \frac{P}{\rho\phi_g}. \tag{61}$$

Note that the ideal gas law can also be expressed in terms of mass and volume fractions of the gas, n_g and ϕ_g, respectively. In other words

$$\rho P V_g = \frac{m_{\text{total}}}{V_{\text{total}}} P V_g = \rho m_{\text{H}_2\text{O}} R_{\text{H}_2\text{O}} T, \tag{62}$$

or

$$\phi_g = \frac{\rho n_g R_{\text{H}_2\text{O}} T}{P}, \tag{63}$$

where $R_{\text{H}_2\text{O}} = 462$ J kg^{-1} K^{-1} is the gas constant for H_2O gas. Thus,

$$c \approx \frac{P}{\rho\sqrt{n_g R_{\text{H}_2\text{O}} T}}. \tag{64}$$

5. Volatiles

Magmatic volatiles are arguably the most important aspect to volcanic eruptions. At depth prior to eruption, where magma pressure is high, volatile solubility is high and the silicate melt contains within its molecular structure volatile elements. As pressure decreases solubility decreases and magmatic volatiles nucleate bubbles and diffuse into existing bubbles. This process will be referred to at *volatile exsolution* or *vesiculation*. Moreover, I shall refer to exsolved magmatic volatiles, which will exist as a supercritical fluid phase and usually in the form of bubbles, as *exsolved voatiles* or *gas* or fluid phase. Mass balance requires the calculation of magma density ρ. Because the magma consists of melt (perhaps crystals) as well as bubbles, magma density is given by

$$\rho = (1 - \phi - \phi_x)\rho_m + \phi_x\rho_x + \phi\rho_g, \tag{65}$$

where ϕ is the volume fraction of exsolved volatiles (gas, bubbles) and ϕ_x is the volume fraction of crystals, which for the time being we shall assume to be zero. Note that

$$\phi_m + \phi + \phi_x = 1, \tag{66}$$

where ϕ_m is the volume fraction of melt. Calculation of ϕ requires that we know the mass fraction of volatiles the have exsolved from the melt as well as its volume, that is the gas density. The former can be obtained from solubility equations and the latter from an equation of state.

5.1. Observational constraints on magmatic volatiles

The mass of magmatic volatiles can be measured using remote sensing techniques. Sulfur dioxide (SO_2) is the easiest of the main magmatic volatiles to measure in volcanic plumes, because its concentration is relatively high compared to ambient atmospheric values [Wallace et al. 2003].

REMOTE SENSING OF MAGMATIC VOLATILES

- Aircraft-based gas analyzers and sensors for CO_2 and H_2S analysis.
- Ground-based and airborne ultraviolet (UV) correlation spectrometer (COSPEC) for SO_2.
- Ground-based and airborne miniature UV spectrometers for SO_2.
- The satellite based Total Ozone Mapping Spectrometer (TOMS) for SO_2 (Figure **??**).
- Satellite based infrared (IR) sensors for SO_2 (e.g., the Moderate Resolution Imaging Spectroradiometer (MODIS) carried by NASAs Earth Observing System (EOS) Terra and Aqua satellites, the Advanced Spaceborne Thermal Emission and Reflection Radiometer (ASTER) on EOS/Terra).
- High Resolution Infrared Sounder (HIRS) on NOAA's polar-orbiting satellites for detection of larger SO_2 clouds in the upper troposphere and stratosphere.
- H_2O, HCl, HF, CO_2 and several other species using Fourier-Transform Infrared (FTIR) spectroscopy.
- Airborne direct measurement of CO_2, SO_2 and H_2S by extraction sampling of plumes (Figure **??**).

Constraints on the pre-eruptive volatile content based on volatile measurements of the erupted volcanic glass are much lower than the pre-eruptive volatile content, because volatile solubility depends on magma pressure and, hence, most volatiles will have exsolved from the melt by the time it quenches to become volcanic glass.

Melt (glass) inclusions have been extensively used to provide constraints on per-eruptive volatile contents. When crystal growth is "imperfect", small amounts of melt becomes trapped within the growing crystal (Figure 19). If the magma erupts and cools rapidly, melt inclusions quench to glass. Because the crystal that contains the melt inclusion may act as a pressure vessel, it is possible that the trapped melt does not degas during eruption and retains the original dissolved volatiles. Over the past few decades measurements of H_2O, CO_2, S, Cl and F in melt inclusions using infrared and Raman spectroscopy, electron microprobe, as well as secondary ion mass spectrometry (SIMS) have resulted in a fairly extensive database of volatile content in melt inclusions [Wallace 2005]. It should, however, be noted that it has been found that some volatile elements, such as hydrogen, can diffuse within relatively short time scales (hours) through the host crystal and, thus, skew measured volatile contents of melt inclusions [Lloyd et al. 2012]. Frequently a large number of melt inclusion measurements are analyzed together in conjunction with models of volatile solubility to assess minimum bounds on volatile content for a specific eruption. However, because of the relatively high pressures under which deep submarine basalts erupt, H_2O (and some other volatile) contents in glasses from submarine ocean-island basalts (OIBs) and mid-ocean ridge basalts (MORBS) can provide direct constraints on volatile contents of the parental magmas.

MINERAL/MELT PARTITIONING OF VOLATILES

Volatiles are typically incompatible in the mineral phase relative to the melt phase. Therefore volatiles are enriched in the melt phase. For example, a melt will contain approximately 10 (100) times the concentration of H_2O than the mantle from which originated after 10% (1%) partial melting of the mantle rock (Figure 20).

5.1.1. CO_2. CO_2 content of magmas is difficult to constrain, because CO_2 is the least soluble of the major volatiles and results in glasses and melt inclusions with lower CO_2 concentrations than the parental magma (H_2O bearing melts with 0.6-1.3 wt.% CO_2 would become vapor-saturated at depths of about 20-50 km). Measured H_2O and CO_2 in melt inclusions in conjunction with H_2O-CO_2 solubility relations suggests that evolved arc magmas contain several wt.% of CO_2, much of which was probably exsolved pre-eruptively as a consequence of vapor-saturated fractional crystallization [Wallace 2005, and references therein].

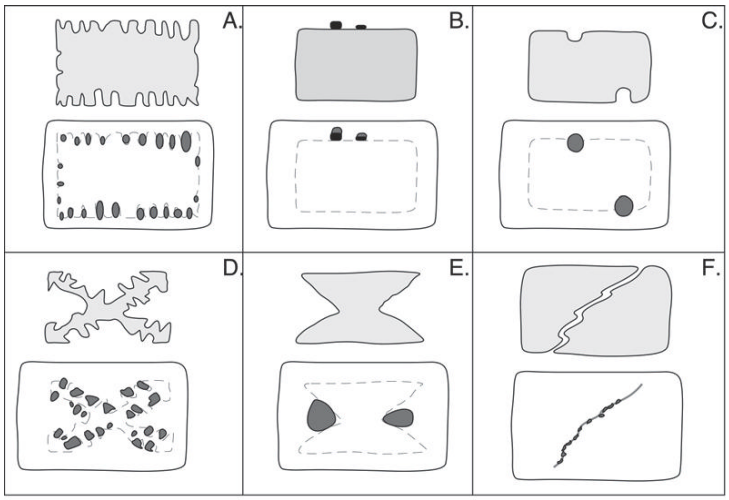

Figure 19

Figure 7 of Kent [2008]. Schematic illustrations of common melt inclusion formation mechanisms relevant to basaltic rocks. Top and bottom images in each panel represent early and later phases in crystal growth. (A) crystal growth following a period of rapid mineral dissolution. (B) Inclusions forming where other minerals abut the host-melt interface, inclusions are associated with mineral inclusions that did not crystallize from the trapped inclusion. (C) Defects at the crystal interface limit localized growth rates. Inclusions are randomly distributed within the host. (D) Textural equilibration and overgrowth following rapid dendritic growth, inclusions are controlled by crystallographic orientations. (E) Overgrowth of skeletal or hopper crystals, inclusions form in symmetric locations. (F.) Healing of melt-filled fractures, inclusions are typically small and define a surface. These may be referred to as secondary inclusions, following common fluid inclusion nomenclature. Modified from Roedder (1979).

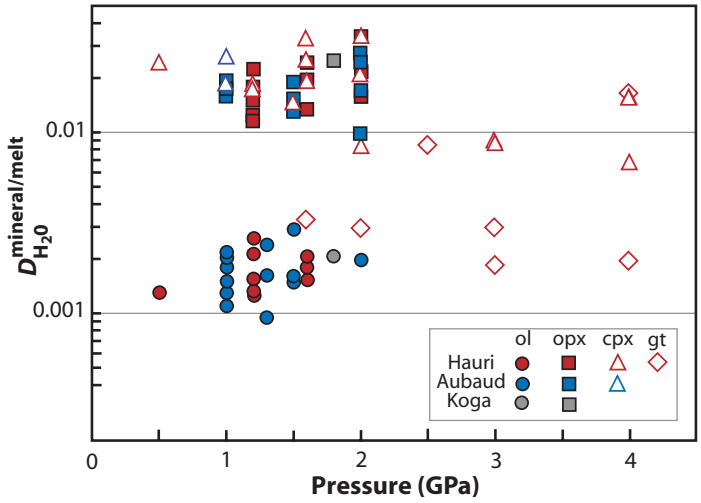

Figure 20

Figure 2 of Hirschmann [2006]. Experimental partition coefficients of H_2O for nominally anhydrous upper mantle minerals (olivine, pyroxenes, and garnet) coexisting with basaltic melt determined by SIMS as a function of pressure [see Hirschmann 2006, for data references].

PRE-ERUPTIVE LOSS OF CO_2

Evolved arc magmas may already contain, or have lost, significant amounts of volatile bubbles prior to eruption (Figure 23). In contrast, the CO_2 content of undegassed MORBs and OIBs appears to be about 1 wt.% or less [Gonnermann and Mukhopadhyay 2007, and references therein]).

H_2O IN BASALTS

Basalt magmas show a wide range of water contents ranging from < 0.5 wt.% to 6-10 wt.% , with non-arc basalts generally being considerably dryer (e.g. Hawaii up to 1 wt.%) than arc basalts, where water content can be highly variable (Figure **??**).

5.1.2. H_2O. Submarine basaltic glasses from back-arc basins tend to have lower H_2O contents than arc basalts, consistent with the hypothesis that slab input of H_2O to the mantle wedge decreases with increasing slab depth (and hence distance from the trench) [Wallace 2005, and references therein]. Silicic magmas also show a wide range of water contents ranging from about 1-6 wt.% [Wallace 2005, and references therein] (Figure 22).

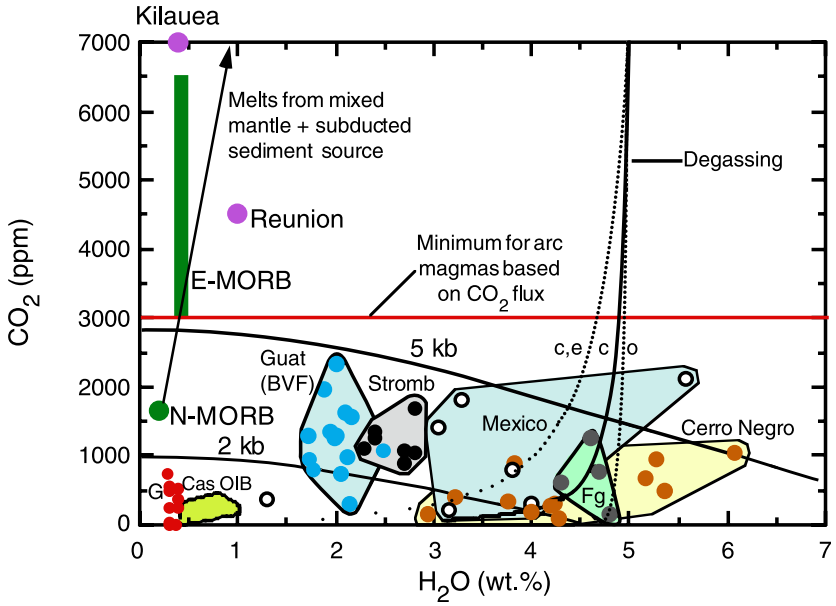

Figure 21

Figure 3 of Wallace [2005]. H_2O vs. CO_2 for melt inclusions from arc basalts. The minimum value estimated for primary CO_2 in arc magmas is $\sim$ 3000 ppm and is derived using the global arc CO_2 flux (Hilton et al., 2002) and the maximum estimated value for flux of magma from mantle to crust in arcs (Crisp, 1984). Arrow shows the H2O and CO2 contents of model basaltic magmas derived from an NMORB mantle source that has been enriched by bulk addition of subducted sediment. The sediment CO_2/H_2O ratio used is the global average from Hilton et al. (2002). Degassing curves are shown for a magma with 5 wt.% H_2O and 7000 ppm CO_2 (calculated using Newman and Lowenstern, 2002). Curves are shown for open-system (o) and closed-system (c) degassing. Also shown is a degassing path for magma that starts with 3 wt.% excess vapor (c,e).

5.1.3. Clorine and Fluorine. Measurable Cl and F are also present in volcanic gases with Cl concentrations in the range of 100s to 1,000s ppm in arc and back-arc magmas [Wallace 2005, Churikova et al. 2007]. Because S is less soluble than Cl, which in turn is less soluble than F [Carroll and Webster 1994] , these gases have also been used to constrain magma degassing [Metrich et al. 2004, Allard et al. 2005, Burton et al. 2007, Edmonds and Gerlach 2007].

5.1.4. Sulfur. H_2S and SO_2 are after water and carbon dioxide the most abundant matmatic volatiles [e.g., Giggenbach 1996]. S concentrations are at a minimum several 1,000s ppm in arc and back-arc magmas and sulfur plays an important role for monitoring of active volcanoes via remote-sensing [Wallace et al. 2003, and references therein].

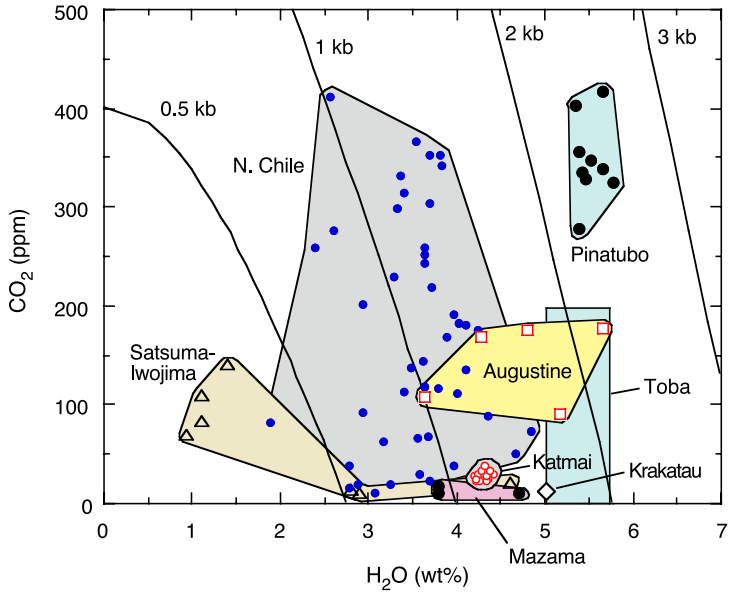

Figure 22

Figure 8 of Wallace [2005]. H_2O vs. CO_2 for melt inclusions from arc dacites and rhyolites. Vapor saturation isobars are shown for 0.5, 1, 2, and 3 kb pressure.

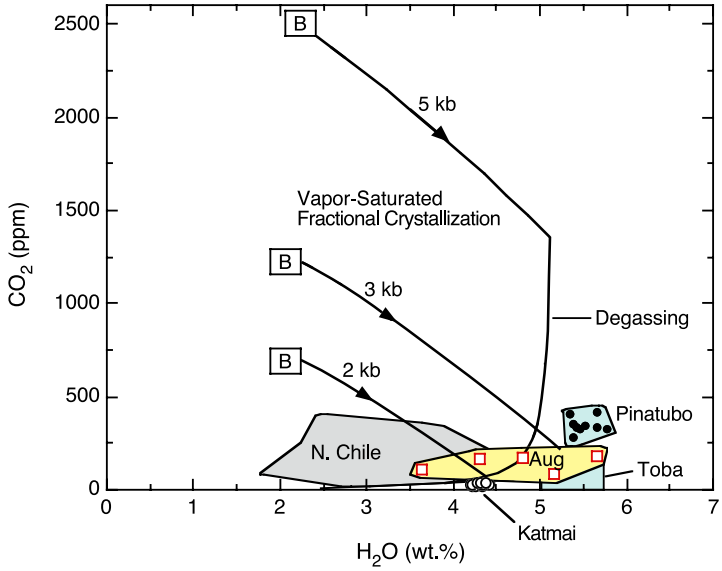

Figure 23

Figure 9 of Wallace [2005]. H_2O vs. CO_2 variations during formation of differentiated magma from basaltic parents (B) by vapor-saturated fractional crystallization at 2, 3, and 5 kb pressure. Approximately 60-70% fractional crystallization is necessary to drive residual liquids from an initial H_2O of 2.25 to 4.5 wt.%. Degassing curve shows the degassing path for magma formed by fractional crystallization at 5 kb, and is calculated for a closed system. If intermediate to silicic magma in arcs is formed primarily by fractional crystallization from a mafic parent at middle to upper crustal pressures (2-5 kb), then the parental melts must generally have H_2O at the lower end of the range shown in Figure 21 to account for the H_2O-CO_2 relations of silicic arc magmas. The reason for this is that **during isobaric fractional crystallization of vapor-saturated magma, H_2O increases in the residual liquid, but CO_2 is preferentially lost to the vapor phase because of its lower solubility**. Significant amounts of H_2O will not be degassed from such differentiating magmas until CO_2 is largely degassed from the melt, at which point the melt becomes saturated with nearly pure H_2O vapor and no additional increase in H_2O occurs with further crystallization.

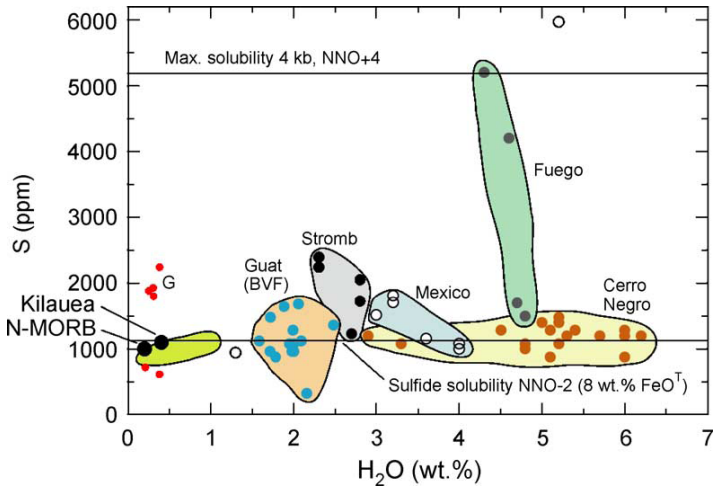

Figure 24

Figure 5 of Wallace [2005]. H2O vs. S for melt inclusions from arc basalts. Data sources and abbreviations as in Figure 21. Saturation limit was calculated using the thermodynamic model of Wallace and Carmichael (1992) updated to incorporate the temperature dependence from Mavrogenes and ONeill (1999).

THE EXCESS SULFUR PROBLEM

- Comparison of remote sensing and petrologic measurements indicates that measured SO_2 fluxes from erupting volcanoes often exceed the amount of SO_2 dissolved in the magma prior to eruption by one to two orders of magnitude (Figure 25).
- Excess sulfur is best explained by the presence of an exsolved pre-eruptive C-O-H-S fluid phase (bubbles), perhaps accumulated in the apical regions of magma reservoirs.
- During isobaric fractional crystallization of vapor-saturated magma, H_2O increases in the residual melt, but CO_2 is preferentially lost to a fluid phase (bubbles), because of its lower solubility. Similarly, S preferentially partitions into a fluid phase in low-temperature silicic magmas.

This excess sulfur problem is thought to be the consequence of an exsolved S-bearing volatile phase accumulating within the magmatic system prior to eruption [e.g., Keppler 1999]. "All andesitic, dacitic, and rhyolitic eruptions in arc environments have excess S emissions, but basaltic eruptions from hot spot volcanoes (e.g., Hawaiian, Iceland) generally do not. Persistently degassing, open-vent systems like Masaya and Stromboli show very large excesses of S released compared with the volume of lava or tephra actually erupted. Based on isotopic and other data, the ultimate source of S and CO_2 in the vapor phase is likely to be from mafic magma, as it is well established that silicic magma reservoirs are created and sustained through long-term intrusion of mantle-derived basaltic magma into the crust" [Wallace 2005, and references therein].

5.2. Solubility

WATER AND VISCOSITY

Volatile species play a central role in governing the ascent and eruption of magma. Dissolved gases, in particular water, have large effects on melt viscosity, whereas exsolved gases (bubbles) allow for significant magma compressibility and buoyancy, which ultimately make eruption possible [Parfitt et al. 1993, Pyle and Pyle 1995, Woods and Cardoso 1997].

Decompression during magma ascent reduces volatile solubility, leading to bubble nucleation and bubble growth by volatile exsolution and expansion [Sparks 1978, Proussevitch et al. 1993, Gonnermann and

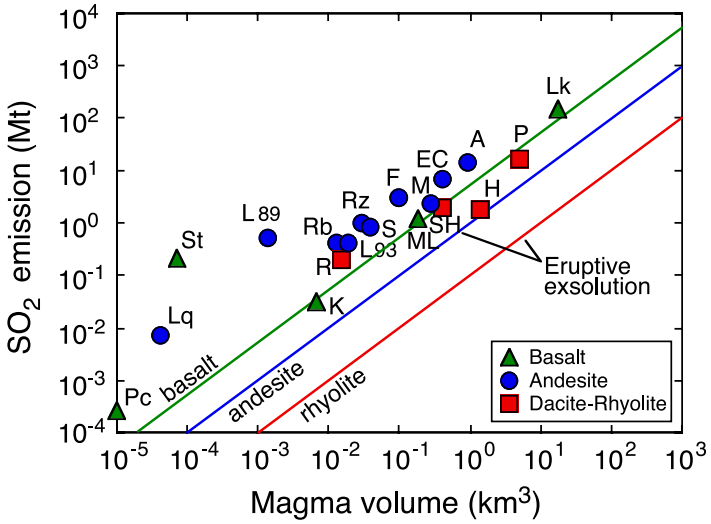

Figure 25

Figure 12 of Wallace [2005]. Volcanic SO_2 emissions, in megatons (1 Mt=10^{12} g), vs. total volume of erupted magma. SO_2 emissions were measured using remote sensing methods. Most of the remote sensing data are from TOMS, except for Etna, Fuego, Kilauea, Lonquimay, Pacaya and Stromboli (COSPEC), Agung (stratospheric optical depth measurements), and Laki (atmospheric turbidity data). Uncertainties of ±50% for both SO_2 emission and eruptive volume are less than to slightly greater than the size of the symbols. Uncertainties in SO_2 emission data are generally considered to be about ±30% for the TOMS data and $\pm 20 - 50\%$ for COSPEC. Data are shown for the following eruptions: (A) Agung, 1963; (EC) El Chichon, 1982; (F) Fuego, 1974; (H) Cerro Hudson, 1991; (K) Kilauea, annual average; (L89) Lascar, 1989; (L93) Láscar, 1993; (Lk) Laki, 1783-1784; (Lq) Lonquimay, 1989; (ML) Mauna Loa, 1984; (M) Mount St. Helens, 1980; (Pc) Pacaya, 1972; (P) Pinatubo, 1991; (Rb) Rabaul, 1994; (R) Redoubt, 1989-1990; (Rz) Ruiz, 1985; (S) Spurr, 1992; (St) Stromboli, annual average. References to data sources can be found in Wallace et al. [2003]. *Shown for comparison are predicted relationships between SO_2 emission and eruptive volume for rhyolitic, andesitic, and basaltic melts calculated by assuming that the only SO_2 released during the eruption is from S that is originally dissolved in silicate melt.* Note that the SO_2 emissions for all eruptions, with the exception of Mauna Loa, Kilauea, and Laki, are at least one order of magnitude greater than predicted for the appropriate bulk composition by syneruptive degassing of dissolved S only.

Manga 2007]. Volatile exsolution also promotes crystallization, which in turn affects bubble growth and rheology – there is a complex feedback between decompression, exsolution, and crystallization [Turner and J. 1960, Tait et al. 1989, Metrich and Rutherford 1998, Metrich et al. 2001, Del Carlo and Pompilio 2004, Simakin and Salova 2004]. The occurrence and dynamics of explosive eruptions are mediated by the initial volatile content of the magma, and the ability of gases to escape from the ascending magma. In the subsequent subsections I briefly review aspects of volatile behavior that are pertinent to the modeling of volcanic eruptions and, for example, the review by Zhang et al. [2007] provides an excellent summary on the subject.

5.2.1. H_2O solubility. The fundamental criterion for chemical equilibrium is that the partial molal Gibbs free energy of each substance, or its chemical potential, μ, be the same in every phase at equilibrium. Vurnham and Davies (1974) expressed chemical potentials for water solubility in silicate melt in terms of water fugacity, f_w^m, as

$$d\mu_w^m = RTd\ln f_w^m, \tag{67}$$

or in terms of activity

$$\ln\left(f_w^m/f_w^0\right)_{P,T} = \ln a_w^m, \tag{68}$$

where f_w^0 is the fugacity of pure H_2 at P and T [Burnham 1994, and references therein]. The observed linear relationship between f_w^m or a_w^m and $(X_w^m)^2$, the square of mole fraction of dissolved H_2O, is generally interpreted as a dissolution-type reaction whereby H_2O dissociates into two mols of products, presumably OH^- [Burnham 1994] (Figure 26).

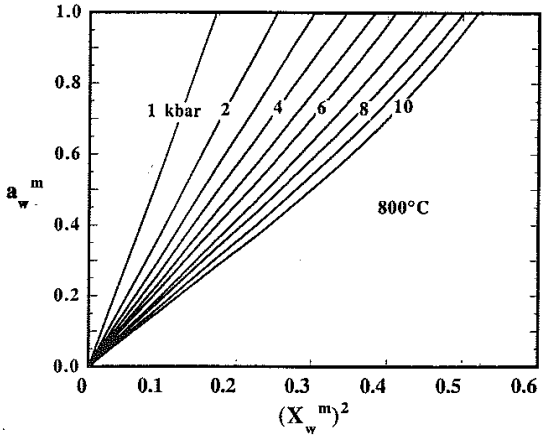

Figure 26

Figure 2 of [Burnham 1994, and references therein]. a_w^m, the activity of H_2O in silicate melts as a function of the square of its mole fraction, $(X_w^m)^2$ and pressure (kbar) at 800 °C.

Based on these experimental findings, a Sievert's law analogue was proposed for the solubility of water in silicate melts (valid for $X_w^m < 0.5$)

$$a_w^m = k_H \left(X_w^m\right)^2, \tag{69}$$

where k_H is analogous to the constant in Henry's Law.

WATER SOLUBILITY: SQUARE ROOT OF PRESSURE

Equivalently, it is found that the solubility of water, S (equivalent to dissolved mole fraction or activity of hydrous species), is proportional to the square root of partial pressure of coexisting water vapor, p_{H_2O}, or fugacity, f_{H_2O} [McMillan 1994]

$$S \propto \sqrt{p_{H_2O}}. \tag{70}$$

This observation, of course, also supports a water dissolution model involving the dissociation of H_2O into hydroxylated species in the melt, either a consequence of changes in the water solubility mechanism and/or changes in the partial molar volumes of aqueous fluid and hydrous melt species [McMillan 1994].

$$H_2O(\text{vapor}) + O^{2-}(\text{melt}) = 2OH^-(\text{melt}), \tag{71}$$

in addition to the dissolution of molecular water. It should be noted that, above approximately 50 MPa, the relationship between S and p_{H_2O} does not follow a simple linear trend. Burnham [1975] proposed a water dissolution model whereby Si-O or Al-O linkages are broken (hydrolized) as depicted inf Figure]reffig-mcmillan-1994-2

However, infrared spectroscopic, as well as nuclear magnetic resonance (NMR) studies have since shown the presence of molecular (undissociated) H_2O in silicate glasses (Figure **??**). At water contents below approximately 1 wt.%, a dissolution mechanism involving only hydroxyl (-OH) groups is a good approximation. However, for higher water contents both hydroxyl groups and molecular H_2O are present. These findings led to a *water speciation* model developed by Stolper and coworkers.

Two "classical" water solubility models are by Burnham and by Stolper [Holloway and Blank 1994, and references therein]. The latter of these models also requires the use of a water speciation model, which is often calibrated to experimental data for albite.

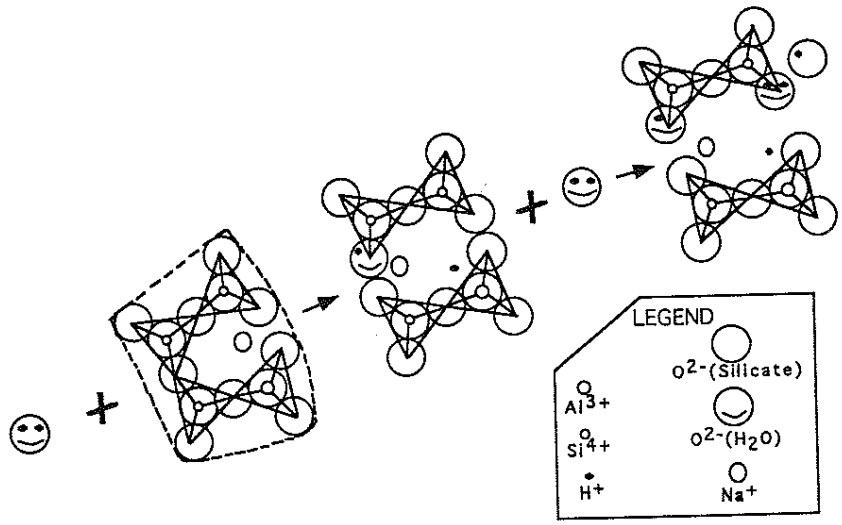

Figure 27

Figure 2 of McMillan [1994] depicting the water dissolution mechanism in albite proposed by Burnham [1975], where the H_2O molecule is represented by the happy face.

A SIMPLE WATER SOLUBILITY MODEL

A simple solubility model often used for rough calculations is provided by [Dobran 2001, on page 221 in] as

$$w_{\text{sat}} = K_s p^{1/n}, \tag{72}$$

with $K_s = 4.1 \times 10^{-6}$ (6.8×10^{-8}) and $n = 2$ (1.43) for rhyolite (basalt) and for CO_2 in basaltic melts $K_s = 4.4 \times 10^{-12}$ and $n = 1$.

5.2.2. CO_2 solubility. Observed deviations above 100 MPa reflect an increased importance of the molar volume term with increasing pressure, which reduce the rate of increase in solubility with pressure [Blank and Brooker 1994] (Figure 28). The effect of temperature on solubility is relatively modest with an inverse relation between temperature and solubility (Figure 29).

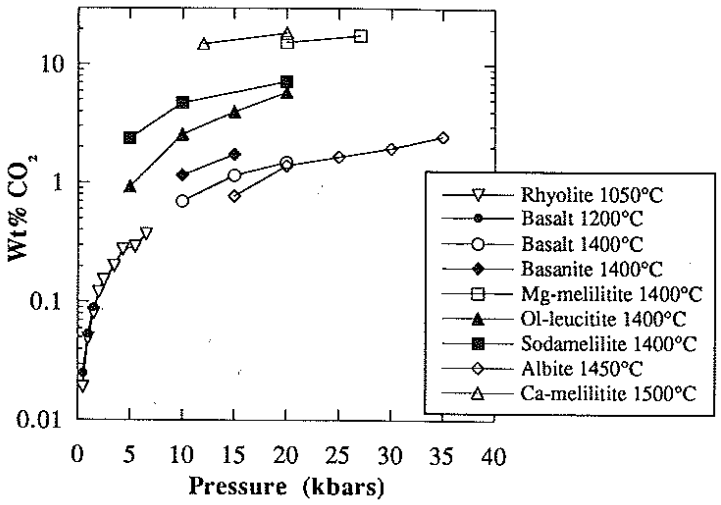

Figure 28

Figure 1 of Blank and Brooker [1994].

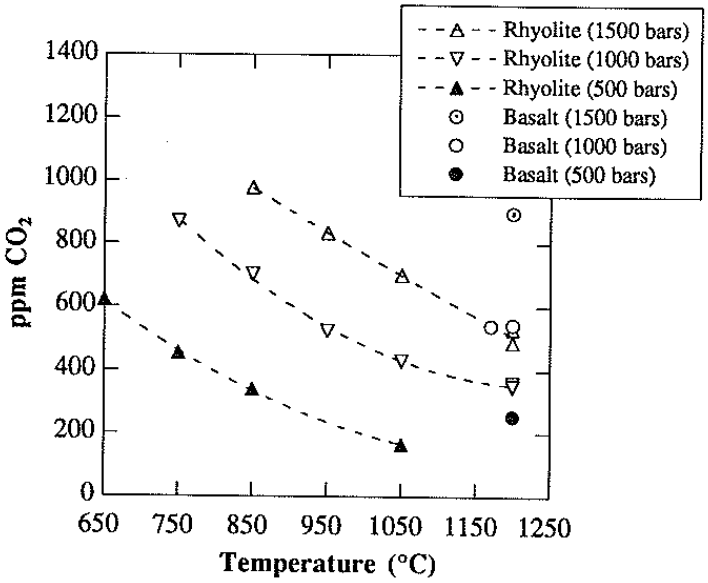

Figure 29

Figure 2 of Blank and Brooker [1994].

Based on vibrational spectra produced by the absorption of certain frequencies of electromagnetic radiation (e.g., infrared) due to molecular vibrational translations, it has been found that CO_2 dissolves as molecules of CO_2 and as carbonate groups (CO_3^{2-}), with a strong dependence of this speciation on melt structure and available cations such as Na^+, Ca^{2+}, and Mg^{2+} [Blank and Brooker 1994]. The dissolution of molecular CO_2 is thought to be via nonreactive occupation of structural "holes" in the silicate melt (ionic porosity model). The dissolution of carbonate is thought to involve the formation of a Ca- or Na-carbonate

complex, with the expulsion of a non-charge-balanced Al from the silicate structural framework, resulting in depolymerization. Unfortunately there are insufficient experiments on the effect of CO_2 on melt viscosity to develop a model for the effect of CO_2 on melt viscosity. A model for CO_2 solubility is provided by [Holloway and Blank 1994, and references therein].

The effect of increasing P_{CO_2} is to increase the amount of CO_2 dissolved in the melt, following a linear relation over pressures of 50 to 500 MPa over a range of natural melt compositions.

5.2.3. Combined H_2O and CO_2 solubility. The behavior of C-O-H volatiles in magmatic systems depends strongly on the relative stabilities of the different molecular species present (e.g., CO, CO_2, H_2O, H_2, CH_4), all a function of oxygen fugacity, pressure, temperature and melt composition. "Geologically important fluid compositions lie in the region bounded by the graphite saturation curve and the CO_2-H_2O join in the C-O-H ternary. Fluid compositions lying below the CO_2-H_2O join contain free oxygen (as molecular O_2) and hence have oxygen fugacities much greater than those commonly found in natural magmatic systems; therefore, magmatic fluids have compositions lying only above the CO_2-H_2O join. Likewise, fluids rich in methane and hydrogen occur only for at oxygen fugacities lower than those commonly found in magmaic systems [Holloway and Blank 1994]."

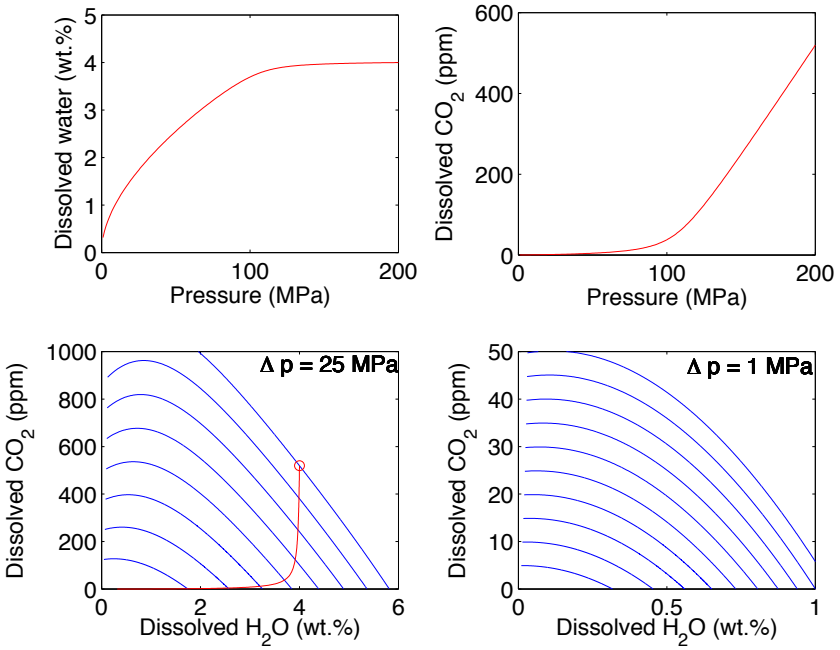

Figure 30

Equilibrium solubility model of Liu et al. [2005].

H_2O-CO_2 SOLUBILITY

An empirical model for joined solubility of H_2O and CO_2 in rhyolitic melts at volcanologically relevant conditions is given by Liu et al. [2005]

$$C_w = 0.0012439\ p_w^{3/2} + \frac{354.94\sqrt{p_w} + 9.623\ p_w - 1.5223\ p_w^{3/2}}{T} + p_c\left(-1.084\times10^{-4}\sqrt{p_w} - 1.362\times10^{-5}\ p_w\right) \quad (73)$$

and

$$C_c = p_c\left[\frac{5668 - 55.99\ p_w}{T} + \left(0.4133\sqrt{p_w} + 0.002041\ p_w^{3/2}\right)\right]. \quad (74)$$

Here C_w is total dissolved H_2O in wt.% and C_c is dissolved CO_2 in ppm. p_w and p_c are the partial pressures in MPa of H_2O and CO_2 respectively. This formulation is also approximately applicable to other melt compositions [Zhang et al. 2007], but more accurate models are available [Newman and Lowenstern 2002, Papale et al. 2006]. Equilibrium dissolved CO_2 and H_2O concentrations based on the formulation of Liu and coworkers are shown in Figure 30 for a temperature of 850 °C. Note that almost all CO_2 exsolves at depth (> 100 MPa) and most H_2O dissolves at relatively shallow depths (< 100 MPa).

5.3. The effect of H_2O and CO_2 on density of silicate melts

Lange and Carmichael (1987) found that the measured volumes of 36 metaluminous Na_2-K_2O-CaO-MgO-Al_2O_3-SiO_2 liquids at a pressure of 1 bar can be modeled with a relative standard error of 0.25% using the following equation (when liquids containing FeO or Fe_2O_3 are added to the data base, the errors on the volume equation increase to 0.4 %)

$$V_m(T) = \sum X_i \left[\bar{V}_{i,T_{ref}} + \frac{d\bar{V}_i}{dT} (T - T_{ref}) \right]. \tag{75}$$

Here $V_m(T)$ is the molar volume of the melt at temperature, T, X_i is the mole fraction of each oxide component, $\bar{V}_i$ is the partial molar volume of each oxide component, and T_{ref} is a reference temperature (representing the midpoint in the experimental temperature range). Conversion from molar volume to the density of silicate melt is achieved using

$$\rho_m = \frac{\sum X_i (MW)_i}{V_m(T)}, \tag{76}$$

where $(MW)_i$ is the molecular weight of oxide component i. **?** recommend values for $\bar{V}_i$ and $d\bar{V}_i/dT$ as summarized in Table 31.

Table 1. Partial molar volumes, thermal expansions and compressibilities of oxide components.

$$V_{liq}(T,P,X_i) = \Sigma X_i [V_{i,1673K} + dV_i/dT\ (T\text{-}1673\ K) + dVi/dP\ (P - 1bar)]$$

	$V_{i,1673K}$ (cc/mole)	$(dV_i/dT)_{1bar}$ (10^{-3} cc/mole-K)	$(dV_i/dP)_{1673K}$ (10^{-4} cc/mole-bar)	$[(dV_i/dP)]/dT$ (10^{-7} cc/mole-bar-K)
SiO_2	26.90 ± .06	0.00 ± 0.50	-1.89 ± .02	1.3 ± 0.1
TiO_2	23.16 ± .26	7.24 ± 0.46	-2.31 ± .06	-----
Al_2O_3	37.11 ± .18	2.62 ± 0.17	-2.26 ± .09	2.7 ± 0.5
Fe_2O_3	42.13 ± .28	9.09 ± 3.49	-2.53 ± .09	3.1 ± 0.5
FeO	13.65 ± .15	2.92 ± 1.62	-0.45 ± .03	-1.8 ± 0.3
MgO	11.45 ± .13	2.62 ± 0.61	0.27 ± .07*	-1.3 ± 0.4
CaO	16.57 ± .09	2.92 ± 0.58	0.34 ± .05*	-2.9 ± 0.3
Na_2O	28.78 ± .10	7.41 ± 0.58	-2.40 ± .05	-6.6 ± 0.4
K_2O	45.84 ± .17	11.91 ± 0.89	-6.75 ± .14	-14.5 ± 1.5
Li_2O	16.85 ± .15	5.25 ± 0.81	-1.02 ± .06	-4.6 ± 0.4
Na_2O-Al_2O_3	-----	-----	10.18 ± .50	----

Volume and thermal expansion data from Lange and Carmichael (1987).
Compressibility data from Kress and Carmichael (1991).
**Fitted parameters should not be applied to pure MgO and CaO liquids.*

Figure 31

Table 1 of Lange [1994].

The **?** model was extended to higher pressures by **?** with an equation that is valid from 0 to 2 GPa [**?**]

$$V_m(X_i, T, P) = \sum X_i \left[\bar{V}_i(T_{ref}, 1\text{ bar}) + \frac{d\bar{V}_i}{dT}(T - T_{ref}) + \frac{d\bar{V}_i}{dP}(p - 1\text{ bar}) \right]. \tag{77}$$

To date the value for the partial molar volume of total dissolved water in siliate melts, $\bar{V}^m_{H_2O,total}$, remains somewhat uncertain, but a best estimate that can be broadly applied to a wide range of melt compositions at variable temperature and pressure is approximately 17 ± 5 cc/mole [Lange 1994] (Table 32). Unfortunately, this uncertainty in $\bar{V}^m_{H_2O,total}$ translates into substantial uncertainties in the densities of natural melts containing significant amounts of water (Figure 34).

Table 2. Current estimates of the partial molar volume of H_2O in silicate liquids

Composition	$\bar{V}^m_{H_2O,total}$ (cc/mole)	P range (kbar)	T range (°C)	Reference
$NaAlSi_3O_8$	14-20	3.5-8.5	750-950	Burnham &Davis (1971)
$NaAlSi_3O_8$	~14	2.0-4.5	1400	Paillat et al. (1992)
$CaMgSi_2O_6$	~17	20	1240	Hodges (1974)
Composition	$\bar{V}^m_{H_2O,molecular}$ (cc/mole)	P range (kbar)	T range (°C)	Reference
$NaAlSi_3O_8$	~22	1-8	1000	Silver et al. (1990)
$KAlSi_3O_8$	~25	1-7	900-1340	Silver et al. (1990)
Ca-Al-silicate	~16	1-5	1180	Silver et al. (1990)
Basalt	~12	1-20	1200	Dixon et al. (1994)
Rhyolite	~0	≤ 1.5	850	Silver et al. (1990)
Rhyolite	~0	≤ 1.5	850	Ihinger (1991)

Figure 32

Table 2 of Lange [1994].

Similarly, the partial molar volume of total dissolved CO_2 remains uncertain, with best estimates for $\bar{V}^m_{CO_2,total}$ falling between 21 and 28 cc/mole [Lange 1994] (Table 33).

Table 3. Best estimates of the partial molar volume of CO_2 in silicate liquids.

Composition	$\bar{V}^m_{CO_2,molecular}$ (cc/mole)	Reference
$NaAlSi_3O_8$	28.6	Stolper et al. (1987)
Rhyolite	28.3	Blank et al. (1993)
Composition	† $\bar{V}^m_{carbonate}$ (cc/mole)	Reference
Tholeiite	27.7	Stolper and Holloway (1988)
Tholeiite	23.1	Pan et al. (1991)
Leucitite	21.5	Thibault and Holloway (1994)
$NaAlSi_3O_8$	24.7	Stolper et al. (1987)

† $\bar{V}^m_{CO_3^{2-}} - \bar{V}^m_{O^{2-}}$

Figure 33

Table 3 of Lange [1994].

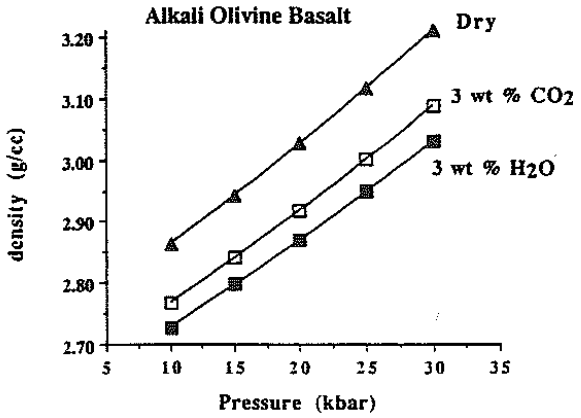

Figure 34

Figure 3 of Lange [1994] depicting the density of an alkali olivine basalt liquid at 1400 °Cas a function of pressure under dry, CO_2 = 3 wt.%, and H_2O = 3 wt.% conditions.

5.4. Diffusivity

5.4.1. H_2O. Volatile diffusivities in silicate melts are best characterized for H_2O and to a lesser extent for CO_2 and S.

H_2O DIFFUSIVITY

A somewhat recent formulation for H_2O diffusivity, D_w ($m^2\ s^{-1}$), in rhyolite is [Zhang and Behrens 2000]

$$\ln \frac{D_w}{C_w} = -17.14 - \frac{10661}{T} - 1.772\frac{p_m}{T} \tag{78}$$

for H_2O contents ≤ 2 wt % and

$$\begin{aligned} D_w &= \alpha \\ &+ \alpha \exp\left[56 + m + X\left(-34.1 + \frac{44620}{T} + \frac{57.3\ p_m}{T}\right)\right. \\ &- \left.\left(0.091 + \frac{4.77 \times 10^6}{T^2}\right)\right] \end{aligned} \tag{79}$$

for higher H_2O [Zhang and Behrens 2000, Zhang et al. 2007].

Here

$$X = \frac{c_w/0.1805}{c_w/0.18015 + (1 - c_w)/0.3249} \tag{80}$$

is the mole fraction of total H_2O dissolved in the melt on a single oxygen basis, $\alpha = 10^{-12} \exp(-20.79 - 5030/T - 1.4\ p_g/T)$, and T is in Kelvin.

H_2O DIFFUSIVITY IN BASALT

From Zhang et al. [2007]

$$\ln \frac{D_w}{C_w} = -8.56 - \frac{19110}{T}. \tag{81}$$

5.4.2. CO_2. CO_2 diffusivity, D_c ($m^2\ s^{-1}$), is smaller than D_w over a range of conditions [Watson 1991, Blank et al. 1991, Blank 1993, Watson 1994]. It has been shown that D_c in silicate melts at volcanologically relevant conditions is essentially identical to the diffusivity of Argon [Behrens and Zhang 2001, Nowak et al. 2004, Zhang et al. 2007]

CO_2 DIFFUSIVITY

$$D_c = D_{\mathrm{Ar}} = -18.239 - \frac{17367 = 1.0964\ p_m}{T} + \frac{(855.2 + 0.2712\ p_m)\, c_w}{T}. \tag{82}$$

5.4.3. S. Zhang et al. [2007] propose the following equation for sulfur diffusivity in basalt at 1498-1723 K and 0.5-1 GPa in the range of 0-4 wt% H_2O

$$D_S = 2.72 \times 10^{-4} \exp\left(-\frac{27692 - 651.6 \times C_W}{T}\right), \tag{83}$$

where C_W is the H_2O content in weight percent.

5.4.4. Gas density. For most volcanological applications a reasonable approximation for gas density is the *Ideal Gas Law*

$$p_g = \frac{\rho_g G T}{M_g}, \tag{84}$$

where $G = 8314.4$ J / (kg mol K) is the universal gas constant, T is temperature, and M_g is the molar mass of the gas. p_g is the gas pressure, which often is assumed equal to the melt pressure, $p_g = p_m = p$. Beyond the ideal gas law there are more accurate *Equations of State (EOS)* available, which can be implemented directly in numerical models or through interpolation functions.

5.4.5. Gas volume fraction. Assuming that ϕ_x+), if the initial concentration of volatile species i, denoted as $C_{i,0}$, is known and its solubility, that is the equilibrium concentration at pressure p_g, denoted as C_i, the volume of exsolved volatiles per unit volume of melt can be calculated as

$$V_g = \frac{\rho_m}{\rho_g}\left(C_{i,0} - C_i\right). \tag{85}$$

The vale of ϕ_g is, in turn, calculated as

$$\phi_g = \frac{V_g}{1 + V_g}. \tag{86}$$

In the presence of crystals a similar, albeit slightly more complicated, expression can be derived. It should be noted that it can be easier, especially when accounting for changes in melt density, to work in terms of moles of oxides and volatiles rather than concentrations. Lastly, it should be noted that it is possible to use the MELTS program to calculate solubilities and densities.

6. Bubbles

KEY CONCEPTS

- Surface tension
- Laplace pressure
- Gibbs free energy for critical bubble nucleus
- Classical nucleation theory
- Rayleigh-Plesset equation for bubble growth
- Viscous and diffusive limits to bubble growth
- Overpressure in bubbles

6.1. Non-equilibrium degassing and overpressure

Thus far we have implicitly assumed that bubbles move with the magma (i.e., *homogeneous bubbly flow*) and that the mass of volatiles dissolved in the melt is exactly equal to the equilibrium solubility value at given pressure and temperature. Here this assumption will be relaxed. Recall that volatile solubility encompasses two processes: *bubble nucleation* and *diffusion into existing bubbles*. Thus, there are several reasons why dissolved volatile concentrations may be higher than the equilibrium solubility value:

REASONS FOR NON-EQUILIBRIUM

- There are no bubbles for volatiles to diffuse into.
- Magma pressure decreases at a higher rate than the rate at which volatiles are able to diffuse into bubbles.
- Significant overpressure of the fluid (gas) phase, that is $\Delta p \equiv p_g \gg p_m$ because of viscosity-limited bubble growth.

6.2. Bubble nucleation

6.2.1. Surface tension.

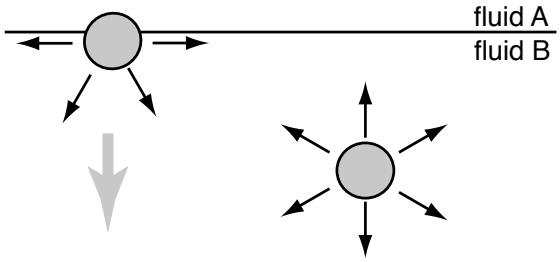

Figure 35

A molecule at the interface between two fluids is missing half its attractive intermolecular interactions and the fluid adjusts its shape in order to expose the smallest possible surface area. (Modified from de Gennes et al., 2004).

From thermodynamic relations it is possible to derive the *surface tension*, σ, as the change in surface excess free energy produced by a unit increase in interface area at constant temperature, T, and constant number of moles, N,

$$\sigma = \left(\frac{\partial F}{\partial A}\right)_{N,T}. \tag{87}$$

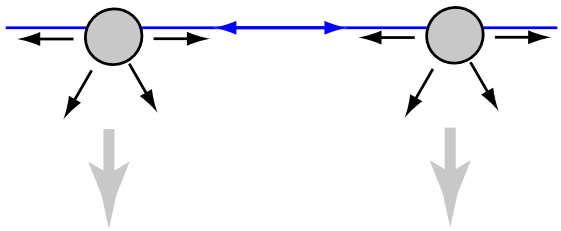

Figure 36

Molecules at the interface between two fluids are pulled into the fluid and also pull against each other due to molecular attractive interactions, thereby creating surface tension.

YOUNG-LAPLACE EQUATION

The difference in fluid pressure on either side of an interface is given by the product of σ and the radius of curvature of the interface, C, at the given point

$$dP = \sigma C, \tag{88}$$

where

$$C = \frac{1}{R_1} + \frac{1}{R_2}. \tag{89}$$

For a sphere $R_1 = R_2 = R_s$ and

$$dP = \frac{2\sigma}{R_s}, \tag{90}$$

the *Young-Laplace equation*.

6.2.2. Thermodynamics of homogeneous nucleation in superheated liquid. At equilibrium, assuming constant and uniform temperature, the chemical potential of liquid, μ_l, and vapor, μ_v, must be equal

$$\mu_l = \mu_v. \tag{91}$$

At equilibrium the pressure of the vapor phase (may also be referred to as the fluid phase) is related to the liquid phase via the Young-Laplace equation

$$P_v = P_l + \frac{2\sigma}{R}. \tag{92}$$

Classical thermodynamics gives the *Gibbs-Duhem equation*

$$d\mu = -s\ dT + v\ dP, \tag{93}$$

where s is the specific entropy ("specific" meaning on a per unit mass basis), T is temperature, v is specific volume, and P is pressure. Assuming a constant temperature and integrating the Gibbs-Duhem equation from the saturation pressure, P_{sat} to an arbitrary pressure, P, gives

$$\mu - \mu_{sat} = \int_{P_{sat}}^{P} v\ dP. \tag{94}$$

For the vapor phase, using the ideal gas law, $v = GT/P$, gives

$$\mu_v = \mu_{sat,v} + \bar{G}T \ln\left(\frac{P_v}{P_{sat}}\right), \tag{95}$$

where $\bar{G}$ is the universal gas constant, $G = 8314.4$ J / (kg mol K), divided by the molar mass of the liquid (in the case of water ≈ 18 kg/mol). Assuming that the liquid is relatively incompressible, that is v is constant, gives

$$\mu_l = \mu_{sat,l} + v_l\left(P_l - P_{sat}\right), \tag{96}$$

where $\Delta P_s = (P_l - P_{sat})$. Substituting for μ_v and μ_l in Equation (91) and using the fact that $\mu_{sat,v} = \mu_{sat,l}$ gives

$$P_v = P_{sat} \exp\left[\frac{v_l \Delta P_s}{\bar{G}T}\right]. \tag{97}$$

Substituting the Young-Laplace equation for P_v gives an equation for the equilibrium radius of a bubble at the time of nucleation

$$R_n = \frac{2\sigma}{P_{sat} \exp\left[v_l \Delta P_s / \bar{G}T\right] - P_l}, \tag{98}$$

which under most conditions applicable to hydrothermal systems can be approximated as

$$R_n \approx \frac{2\sigma}{\Delta P_s}, \tag{99}$$

that is the Young-Laplace equation, with $R_n \sim 10^{-8}$ m for homogeneous nucleation in silicate melts. Substituting the Young-Laplace equation for P_l gives an equation for P_v of a bubble at the time of nucleation

$$P_v = P_{sat} \exp\left[\frac{v_l \left(P_v - P_{sat}\right) - 2\sigma / r_n}{\bar{G}T}\right]. \tag{100}$$

Typically, $(P_v - P_{sat}) \ll 2\sigma / R_n$ and

$$P_v \approx P_{sat} \exp\left[\frac{-2 v_l \sigma}{r_n \bar{G}T}\right]. \tag{101}$$

6.2.3. Bubble nucleation in a melt phase (Gibbs free energy).

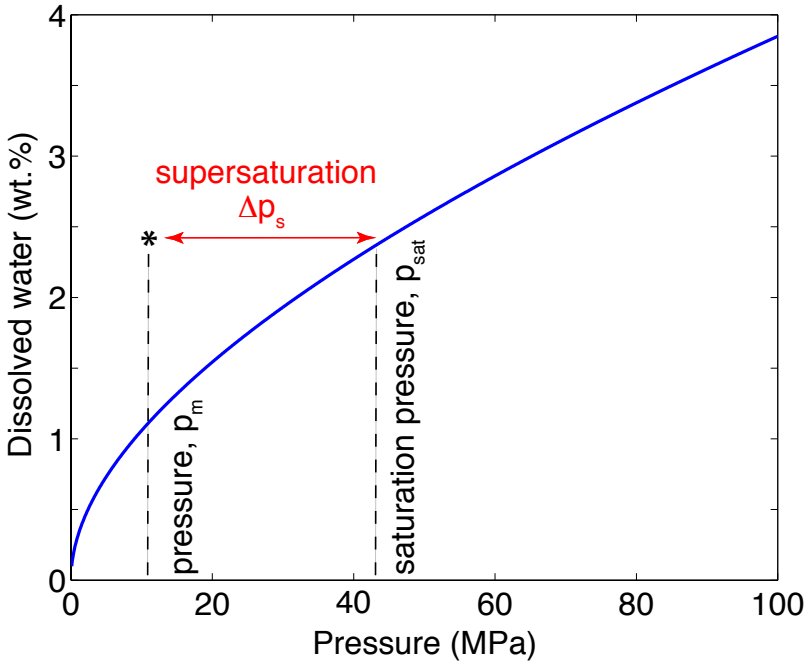

Figure 37

Supersaturation of water dissolved in silicate melt. This curve was calculated using the solubility model of Liu et al. [2005] and for illustrative purposes may be considered roughly applicable to rhyolites and dacites at temperatures of about 900-1000°C.

The Gibbs free energy, ΔG_f, is a measure of the available non-PV work in a system (e.g., chemical). The formation of 2 mol of a substance from the elements in their standard states yields the standard Gibbs free energy of formation

$$\Delta G_f^o = \Delta H_f^o - T \Delta S_f^o, \tag{102}$$

where H is enthalpy, T is temperature, and S is entropy. For a irreversible chemical reaction at constant volume we can measure the heat of reaction, Q_{irrev}, and obtain the change in enthalpy from

$$\Delta H_r = \Delta U_r - P\Delta V, \tag{103}$$

where $\Delta U_r = Q_{\text{irrev}}$ is the change in internal energy. Using an experiment to measure the heat of a reversible reaction, $Q_{\text{reversible}}$, allows us to determine the change in enthalpy from its definition

$$\Delta S = \frac{Q_{\text{reversible}}}{T} \tag{104}$$

and hence, the change in Gibbs free energy of formation. The kinetics of phase changes are such as to minimize the Gibbs energy of the system. The molar Gibbs free energy difference between vapor and melt is

$$\Delta G_{gm} = \int (V_g - V_m)\, dP = RT \ln\left(\frac{P_g}{P_{sat}}\right) - V_m\left(P_m - P_{sat}\right), \tag{105}$$

where $V_g = RT/P_g$ is the molar volume of the vapor phase, V_m is the partial molar volume of the volatile dissolved in the melt, P_g is the pressure of the exsolved vapor (gas) phase in the bubble, P_{sat} is the saturation (equilibrium) pressure for the amount of volatile dissolved in the melt phase, P_m is the ambient melt pressure, T is temperature, and R is the gas constant. Because typically $V_m \ll V_g$

$$\Delta G_{gm} \approx \int V_g dP = RT \ln\left(\frac{P_g}{P_{sat}}\right). \tag{106}$$

If the difference in molar volume of the vapor phase is small, that is

$$V_g(P_m)/V_g(P_{sat}) \sim 1, \tag{107}$$

then we can assume that V_g is approximately constant and

$$\Delta G_{gm} \approx \int V_g dP \approx V_g\left(P_m - P_{sat}\right). \tag{108}$$

The total energy to produce a cluster of gas molecules of radius R_n is

$$\Delta G_f = \frac{4}{3}\pi R_n^3 \Delta G_{gm}/V_g + 4\pi R_n^2 \sigma. \tag{109}$$

or

$$\Delta G_f \approx -\frac{4}{3}\pi R_n^3\left(P_m - P_{sat}\right) + 4\pi R_n^2 \sigma. \tag{110}$$

GIBBS FREE ENERGY FOR A BUBBLE NUCLEUS

In other words, the change in Gibbs energy associated with the formation of a bubble nucleus consists of the Gibbs free energy change associated with the formation of a unit volume of the bubble nucleus and change in energy associated with overcoming the surface tension between the vapor phase and the melt. The volume term is negative, otherwise the phase transformation from liquid to vapor would be prohibitive. However, the surface tension term is positive and acts against the formation of a nucleus. The critical nucleus size is where

$$\frac{\partial \Delta G_f}{\partial R_n} = 0, \tag{111}$$

and therefore,

$$R_c \approx \frac{2\sigma}{P_{sat} - P_m} = \frac{2\sigma}{\Delta P_s}. \tag{112}$$

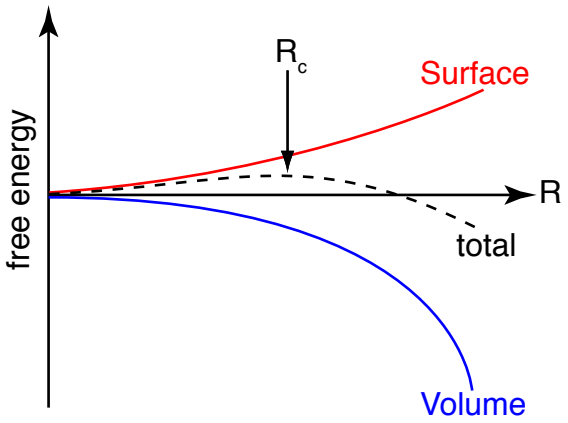

Figure 38

Change in net free energy (ΔG_f) of bubble nucleus as a function of radius, R. At any time random local fluctuations in the concentration of water molecules that are dissolved within the silicate melt lead to the formation of small *clusters* of water molecules (typically of the order of 100-1000 molecules), called *embryos*. If the size of such an embryo exceeds the critical radius, R_c, then the addition of water molecules is energetically favorable, that is the embryo will grow, that is a bubble is nucleated.

6.2.4. Classical nucleation theory (CNT). If the concentration of dissolved volatiles exceeds equilibrium during magma decompression new bubbles may nucleate. The difference between measured pressure and the pressure at which the concentration dissolved volatiles are expected to be in equilibrium with the melt is the *supersaturation pressure, Δp_s*. Supersaturation is required to overcome the energy barrier for bubble nucleation provided by surface tension. Supersaturation can be attained if the rate at which decompression lowers the actual pressure exceeds the rate at which diffusion of volatiles from the melt decreases the saturation pressure.

Figure 39

Figure 4 of Gonnermann and Gardner [2007]. (a) Schematic representation of the modeled melt volume. (1) represents the bubble; (2) the diffusion envelope that is the part of the melt where volatile concentrations and correspondingly nucleation rates are low; and (3) is the nucleation region. During most of the modeling, the volume fraction of melt comprised by region (3) is close to a value of 1. (b) Schematic graph of volatile concentration in the melt as a function of radial distance, r, where R is the bubble radius and S is the radius of the surrounding melt shell. The difference between the saturation pressure at the actual volatile concentration (solid red curve) and the equilibrium concentration at the pressure inside a bubble nucleus is the supersaturation pressure.

SATURATION AND SUPERSATURATION

Within the context of silicate melts and volatiles the following terminology is used.

- Equilibrium solubility: The concentration of volatiles that would dissolve from a coexisting fluid phase into the melt at a given pressure and temperature, if given enough time for the volatiles to diffuse into and throughout the melt.
- Saturation pressure: The pressure at which the actual concentration of dissolved volatiles would be in equilibrium.

- Undersaturation: If the actual concentration of dissolve volatiles is greater than the equilibrium concentration at the same pressure and temperature.
- Supersaturation: If the actual concentration of dissolve volatiles is greater than the equilibrium concentration at the same pressure and temperature.
- Supersaturation pressure: The difference between actual pressure and saturation pressure.

During bubble nucleation, the characteristic time for volatile diffusion depends primarily on the bubble number density, N_m. For an idealized uniform *packing geometry* of bubbles it can be approximated as

$$N_m \approx \frac{3}{4\pi(S^3 - R^3)}, \tag{113}$$

where R is bubble radius and S is the radial distance from bubble center to the midpoint between adjacent bubbles. For a volatile diffusivity, D, the characteristic diffusion time is

$$\tau_D \sim \frac{(S-R)^2}{D}. \tag{114}$$

Using the relation

$$\phi_g = R^3/S^3, \tag{115}$$

gives

$$R = S\phi_g^{1/3} \tag{116}$$

and

$$S \approx \left(\frac{3}{4\pi N_m(1-\phi_g)}\right)^{1/3}, \tag{117}$$

so that

$$R \approx \left(\frac{3\phi_g}{4\pi N_m(1-\phi_g)}\right)^{1/3} \tag{118}$$

and

$$\tau_D \sim N_m^{-2/3}. \tag{119}$$

Nucleation will take place on timescales that are less than about τ_D.

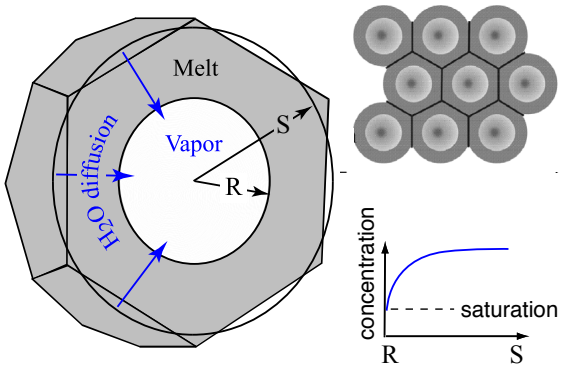

Figure 40

Conceptual drawing of volatile concentration in melt surrounding a bubble existing within an idealized uniform packing geometry.

HOMOGENEOUS AND HETEROGENEOUS NUCLEATION

Bubble nucleation can be homogeneous or heterogeneous.

- Homogeneous bubble nucleation: Bubble nuclei comprised of volatile molecules form and grow spontaneously within the silicate melt.
- Heterogeneous bubble nucleation: Bubble nuclei comprised of volatile molecules form and grow spontaneously on the surface of "impurities" within the silicate melt. For example, crystals (e.g., Fe-Ti oxides) can provide such nucleation substrates.
- At the same Δp_s the nucleation rate for heterogeneous nucleation is higher than for homogenous nucleation, because the nucleation substrates lower the energy barrier for nucleation due to a lower surface tension between bubble nucleus and nucleation substrate.
- Nucleation rate depends on the *effective surface tension* between the fluid phase inside bubble nuclei and the homogeneous silicate melt and/or heterogeneous nucleation substrate.
- The effective surface tension for bubble nuclei is different than the macroscopically measurable surface tension between the different phases, that is fluid-melt or fluid-crystal.

Random local fluctuations in the concentration of dissolved water molecules leads to the formation of small clusters of water molecules (*embryos*). Those that are of critical radius or greater will grow into bubbles and are called bubble *nuclei*. Based on *Classical Nucleation Theory* (CNT) the number of embryos of size larger than the critical size, R_c, formed per unit time and unit liquid volume increases with increasing supersaturation, ΔP_s, according to [e.g., Mangan and Sisson 2005, Cluzel et al. 2008, and references therein]

$$J = J_0 \exp\left[-\frac{16\pi\sigma^3}{3k_B T \Delta P_s^2}\right], \tag{120}$$

where J is the bubble nucleation rate in number of bubbles per unit volume of liquid per unit time,

$$J_0 = \frac{2n_0^2 V_m D}{a_0}\sqrt{\frac{\sigma}{k_B T}}, \tag{121}$$

σ is the effective surface tension between liquid (melt) and bubble nucei (fluid), $k_B = 1.3805 \times 10^{-23}$ J/K is the Boltzmann constant, n_0 is the number density of dissolved volatile molecules, $V_m = 2 \times 10^{-29}$ m^3 is the volume of a volatile molecule, D is the diffusivity of the volatile species in silicic melt, T is the absolute temperature, $a_0 \approx n_0^{-1/3}$ is the mean distance between dissolved volatile molecules, $n_o = (N_A X_M \rho_L / m)$ is the number of water molecules, $N_A = 6.02 \times 10^{23}$ is the Avogadro number, ρ_L is the liquid (melt) density, m is the molar mass of the volatile species (0.018 kg/mol in the case of water), X_M is the mass fraction of dissolved molecular water (X is the total mass fraction of dissolved water and is equal to the solubility value at P_{sat}). Values of σ are approximately 0.05 N/m, with a dependence on both temperature and composition of the melt.

As shown Figure 41, bubble number densities (BNDs) in silicic explosive eruptions often fall in the range of 10^{14} to 10^{16} per m^{-3} of melt (glass). To achieve such high BNDs requires high nucleation rates and, in turn, high supersaturation pressures and/or low surface tension (Figure 42). Regardless of surface tension, the necessary supersaturation has to be achieved during magma decompression within a time of the order of τ_D. In the case of homogeneous nucleation, the required decompression rates may be as high as about ~100 MPa s^{-1}. Such high decompression rates are not easy to reconcile with magma ascent in volcanic conduits and are likely only achieved in the region where the magma fragments.

6.2.5. Heterogeneous nucleation. The presence of impurities, such as crystals - if they have lower interfacial energy between fluid phase and crystal phase than the interfacial energy between fluid phase and melt phase - reduces ΔG_f. Consequently, higher nucleation rates may be achieved at more modest super saturations. In other words, $\Delta P_{s,\text{heterogeneous}} \ll \Delta P_{s,\text{homogeneous}}$, all else being equal. Within the context of classical nucleation theory, the exponential term in Equation (120) can be scaled by a factor $0 \leq \psi \leq 1$, which is a geometrical factor that depends on the wetting relationships between bubble and crystal. This

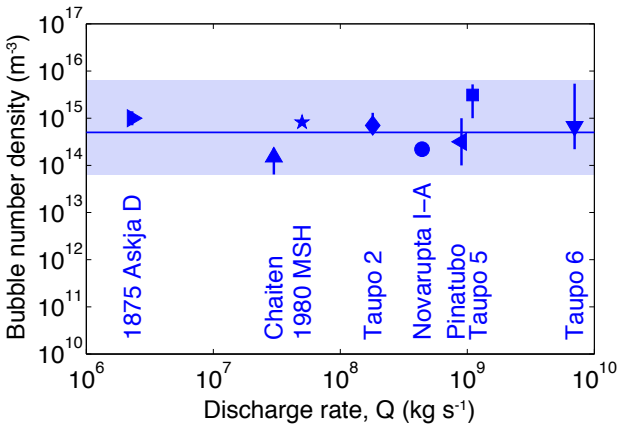

Figure 41

Incomplete compilation of bubble number densities in pyroclasts from explosive eruptions of rhyolitic melts.

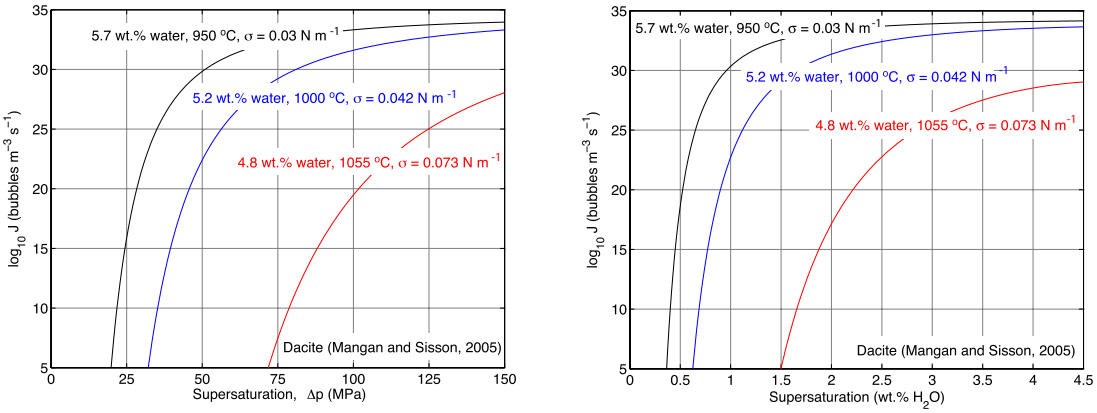

Figure 42

Bubble nucleation rate in dacitic melt as a function of supersaturation pressure (left) and H_2O supersaturation (right).

relationship is determined by the *contact angle* θ (Figure 43)

$$\psi = \frac{(2-\cos\theta)\,(1+\cos\theta)^2}{4}, \tag{122}$$

which controlled by the relative values of the interfacial (surface) tensions: vapor-liquid (σ_{LB}), vapo-crystal (σ_{SB}), and crystal-liquid (σ_{SL}). It is defined as

$$\cos\theta = \frac{\sigma_{SB}-\sigma_{SL}}{\sigma_{LB}}.. \tag{123}$$

For $\theta > 90°$the vapor bubble is poorly wetting and for $\theta < 90°$the vapor bubble is wetting the crystal. For a perfectly wetting liquid $\theta = 0°$and bubbles will not preferably nucleate on the crystal, therefore, $\psi = 1$ and the presence of crystals has no effect on nucleation. For $\theta = 90°$the activation energy for nucleation is divided by two, that is $\psi = 0.5$. For a perfectly non-wetting liquid $\theta = 180°$and $\psi = 0$, implying that the nucleation rate is independent of the presence of crystals. The geometrical ψ depends on the shape of the nucleation substrate, with Equation ((122)) corresponding to the case of a planar substrate. Relative to a planar surface, the nucleation efficiency will be enhanced on a concave substrate, but reduced on a convex substrate [Cluzel et al. 2008, and references therein].

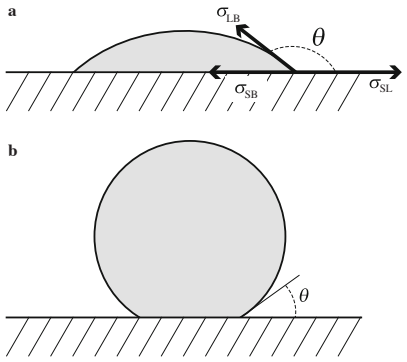

Figure 43

Figure 7 of Cluzel et al. [2008] showing the wetting relationship of a bubble (in grey) with a crystal in a liquid. The contact angle h is controlled by the relative values of the bubbleliquid, bubblecrystal, and liquidcrystal surface tensions, σ_{LB}, σ_{SB}, and σ_{SL}, respectively. The case of a non-wetting liquid ($\theta > 90°$) is illustrated in **a**, the case of a wetting liquid ($\theta < 90°$) in **b**

BUBBLE NUCLEATION IN CONDUIT MODELS

To date few conduit models have incorporated bubble nucleation explicitly. An example of a model with nucleation based on CNT is Massol and Koyaguchi [2005].

6.3. Bubble growth

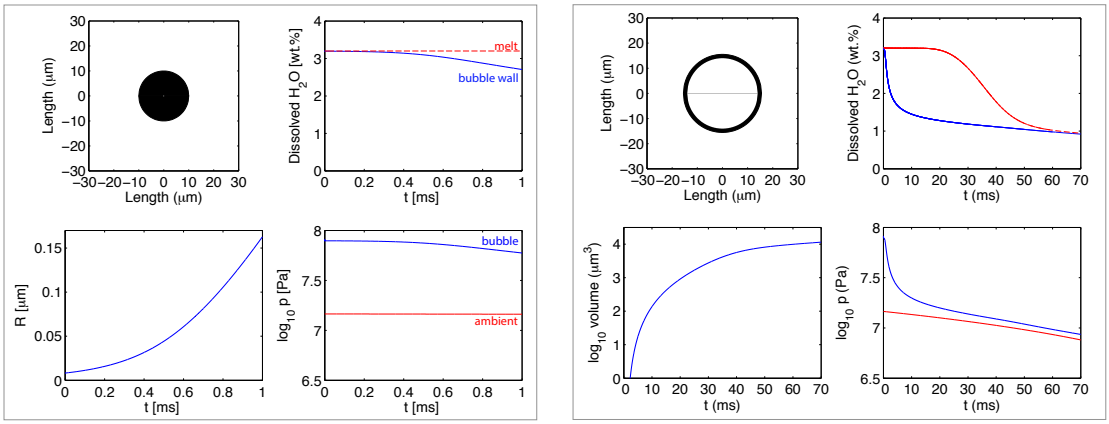

Figure 44

Illustrative example of a bubble growth simulation. Bubble on the left is 1 ms after nucleation, whereas on the right is 70 ms after nucleation, both for $N_m \sim 10^{16}$ m^{-3}. Note that the melt stays supersaturated for several 10s of ms. Also note that the geometry of the simulated bubble eventually becomes inconsistent with the assumed packing geometry. In other words, at $N_m \sim 10^16$ m^{-3} bubbles could not remain spherical for long as they grow.

Magma pressure, p_m, decreases during magma ascent. The pressure of the fluid inside bubble nuclei is $\sim 10^7$ MPa larger than p_m. In other words, $p_g - p_m \sim \Delta p_s \sigma / R_n \sim 10^7$ MPa. Only bubble nuclei with $p_g - p_m > 2\sigma/R$ (the Laplace pressure) will grow. The excess pressure above the Laplace pressure is an outward force on the melt that surrounds the bubble that causes the melt to deform and the bubble to grow. As a consequence the fluid inside the bubble expands in volume and its pressure, p_g, decreases. This, in turn, decreases the volatile solubility at the fluid-melt interface, causing volatiles to transfer from the melt into the bubble. This is *exsolution*. As a consequence the concentration of dissolved volatiles at the fluid-melt interface decrease, relative to the melt at larger distances from the bubble, which results in a concentration gradient and volatile diffusion toward bubbles. Thus more volatiles are transferred by diffusion and exsolution into bubbles, thereby affecting the rate and amount of bubble growth.

The bubble-growth process can be described by a momentum balance for melt that surrounds the growing bubble, together with a diffusion equation for volatiles within the melt, mass balance for the bubble itself, as well as a solubility law for the volatiles and an equation of state. The momentum balance for bubbles in silicate melts are based on the *Rayleigh-Plesset equation* Scriven [1959], albeit with neglecting inertial terms. The latter is justified because large melt viscosities and short length scales result in Reynolds numbers for the bubble's momentum balance that are $\ll 1$. The resultant governing equation for a bubble surrounded by melt of constant viscosity is

$$p_g - p_m = \frac{2\gamma}{R} + 4\eta \left(\frac{1}{R} - \frac{R^2}{S^3} \right) \frac{dR}{dt}. \tag{124}$$

Here dR/dt is the radial velocity of the melt-vapor interface and an idealized uniform packing geometry is assumed so that each bubble can be represented as a gaseous sphere of radius R surrounded by a melt shell of thickness $S - R$. The time-dependent boundary condition for this equation is p_m, so that bubble growth and magma ascent are directly coupled via p_m. This equation is integrated to give $R(t)$.

Mass conservation of volatiles requires that

$$\frac{d}{dt} \left(\tfrac{4}{3}\pi \rho_g R^3 \right) = 4\pi R^2 \rho_m \sum_i D_i \left(\frac{\partial c_i}{\partial r} \right)_{r=R}, \tag{125}$$

where ρ_g is non-constant volatile density, ρ_m is melt density, D_i is (concentration dependent) diffusivity of volatile species i in the melt, and c_i is the mass fraction of the dissolved volatile of species i. Using an equation of state, mass balance can be integrated for $p_g(t)$.

Volatile diffusion is governed by

$$\frac{\partial c_i}{\partial t} + v_r \frac{\partial c_i}{\partial r} = \frac{1}{r^2} \frac{\partial c_i}{\partial r} \left(D_i \, r^2 \frac{\partial c_i}{\partial r} \right), \tag{126}$$

where v_r is the radial velocity of melt at radial position r, which can be obtained from dR/dt. Boundary conditions for the diffusion problem are determined from a suitable solubility model, for which it is assumed that $c_i(t, r = R)$ is the equilibrium solubility value of species, i, at and $p_g(t)$ and given composition of the fluid phase inside the bubble at time t. The coupled problem requires care when integrating, because the flux of volatiles at $r = R$ is very sensitive to the value of $c_i(t, r = R)$, which depends on p_g, which itself depends on the flux of volatiles at $r = R$.

RATE-LIMITED BUBBLE GROWTH

Exsolution and expansion are impeded by surface tension and viscous stresses in the melt. Because surface tension forces are comparatively small Sparks [1978], there are two principle rate-limiting processes during bubble growth, for which it may be feasible to simplify the solution of the governing equations or to use analytical growth laws.

- Diffusive limit: In this limit the rate of diffusion of volatiles to the melt-vapor interface, where they can exsolve, is slower than the magma decompression rate.
- Viscous limit: In this limit the rate of viscous flow of the melt is too slow to allow the fluid inside the bubble to expand. As a consequence, $p_g \gg p_m + 2\sigma/R$. The viscous limit is most significant at melt viscosities in excess of 10^9 Pa s Sparks et al. [1994], Toramaru [1995]. In the absence of significant amounts of crystals, such high viscosities are limited to silicic melts at relatively low pressures, where the dissolved water content is relatively low, which requires that sufficient bubbles have nucleated so that bubble growth is not in the diffusive limit . In the viscous limit p_g decreases at a much slower rate than p_m, resulting in the buildup of overpressure, defined as $\Delta p = p_g - p_m$. This has been referred to as *viscosity quench* Thomas et al. [1994] and is thought to lead to magma fragmentation. Because solubility depends on pressure, overpressure during viscosity-limited bubble growth can lead to volatile supersaturation.

6.3.1. Bubble growth in conduit models. Few conduit models have incorporated diffusive bubble growth, an example of doing so is Proussevitch and Sahagian [2005]. In such models bubble growth is treated

at the sub-grid scale, where $p_m(z)$ is calculated from conduit flow calculations for which it is assumed that the magma is a homogeneous mixture with average properties. Given $p_m(z)$ values of $R(z)$, $p_g()$ and $c_i(z,r)$ are calculated using the transformation

$$\frac{d}{dz} = \frac{1}{u_z}\frac{d}{dt}. \tag{127}$$

Incorporating bubble growth in this manner yields a model that allows the calculation of fluid (gas) overpressure $\Delta p = p_g - p_m - 2\sigma/R$, which is useful for assessing conditions for magma fragmentation and the degree to which volatile concentrations are not at equilibrium. In particular for H_2O will have implications for magma viscosity and, hence, a number of factors affecting the eruption, for example decompression rate and magma fragmentation.

As will be seen in the next section, separated two-phase flow models include a Δp term that can be calculated different ways, one of them is from the momentum balance for bubble growth (see *Lecture Notes Appendix: Bubble Growth*), which gives the result

$$\Delta P \equiv P_g - P_m = -\frac{4}{3}\frac{\mu_m}{\phi}\frac{du_z}{dz}, \tag{128}$$

where surface tension has been neglected.

7. Separated gas flow, open-system degassing

KEY CONCEPTS

- Open vs. closed system degassing
- Buoyant bubble rise
- Bubble coalescence
- Darcy's law
- Permeable outgassing

Thus far we have implicitly assumed that bubbles move with the magma (i.e., *homogeneous bubbly flow*). Often this may not be the case. For example, in basaltic magmas the melt viscosity is low enough to where bubbles can coalesce efficiently to form large bubbles that, due to their lower density (buoyancy), rise to the surface at a faster velocity that the melt phase. In this case our *system*, defined as a parcel of magma, no longer is a *closed system* but rather an *open system*, because the volatile fluid phase may enter and exit the system.

High viscosity magmas, however, may also be subjected to *open system degassing*. In high viscosity magmas bubbles will also coalesce, but because of the high melt viscosity, the time for bubbles to fully coalesce can be long, relative to the magma ascent time. As a consequence, many bubbles within the magma will become interconnected through small holes that form within the melt film that separates adjacent bubbles. The magma thus becomes a *permeable medium* through which the volatile fluid can flow independently of the melt phase. This is referred to as *permeable gas flow*. If through this process there is a net gas loss from a parcel of magma it is referred to as *permeable outgassing*, which is thought to lead to dense magmas, such as *obsidian*, during effusive silicic eruptions.

If we define individual parcels of ascending magma as a system, then outgassing is the end result of open-system degassing processes. During open-system degassing (1) volatile bubbles may be lost or gained by a given magma parcel through buoyant bubble rise; (2) exsolved volatiles may flow along pressure gradients within the volcanic conduit through a permeable network of bubbles that are connected through small apertures produced by bubble coalescence; and (3) bubble walls may be ruptured during magma fragmentation allowing volatiles to escape from the magma.

7.1. Buoyant rise of a spherical bubble

Buoyancy, B, of sphere of lower density material than the fluid in which it is suspended is the total force due to gravity, g, on the density difference, $\Delta\rho$ between he sphere and its surroundings

$$F_B = -\frac{4\pi}{3}R^3 g\Delta\rho. \tag{129}$$

Buoyancy is balanced by viscous resistance, which is proportional to strain rate, which is proportional to the velocity gradient in the vicinity of the sphere. Assume that the velocity of the sphere is u_s and that the fluid next to the sphere is being dragged along at that velocity, but that the velocity of the fluid decreases to a fraction of u at a distance R from the sphere. Therefore the velocity gradient is given by u/R. Viscous stress is viscosity times strain rate, or in this case

$$\tau = c\eta\frac{u}{R}, \tag{130}$$

where c is a constant whose value will be of order 1. The total viscous resisting force acting on the sphere will be the viscous stress multiplied by the surface area of the sphere

$$F_\eta = -4\pi cR\eta u. \tag{131}$$

Because these forces have to balance, $F_B + F_\eta = 0$, which can be solved for the buoyant rise velocity of the sphere

$$u_s = -\frac{g\Delta\rho R^2}{3c\eta}. \tag{132}$$

TERMINAL VELOCITY OF A BUOYANT SPHERE

This terminal rise velocity of a sphere at low Reynolds numbers is also called the *Stokes velocity*. If the viscosity of the sphere, η_s, is different from the viscosity of the surrounding fluid, η, then

$$c = \frac{\eta + 1.5\eta_s}{\eta + \eta_s}. \tag{133}$$

Thus

$$u_s = -\frac{g\Delta\rho R^2}{3\eta}\left(\frac{\eta + \eta_s}{\eta + 1.5\eta_s}\right). \tag{134}$$

If $\eta_s \ll \eta$, typically the case for volatile bubbles in magmas, then $c \approx 1$ and

$$u_s \approx -\frac{g\Delta\rho R^2}{3\eta}. \tag{135}$$

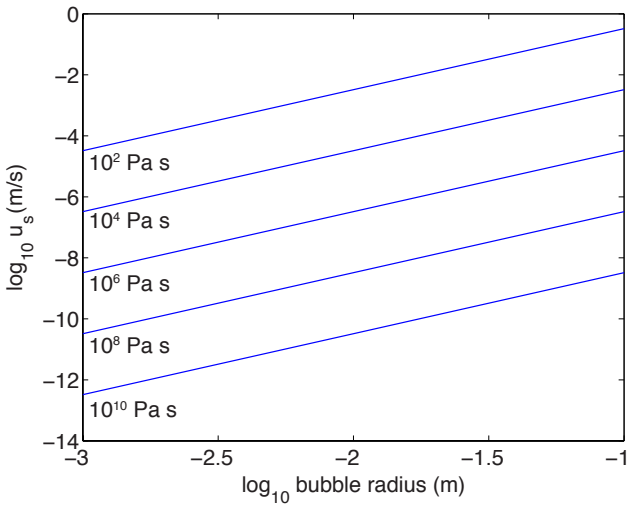

Figure 45

Terminal rise velocity of a single bubble.

7.2. Slow buoyant rise of many spherical bubbles

If we are dealing with a suspension of many spherical bubbles rising due to buoyancy in a volume of liquid, the hydrodynamic interactions between individual bubbles affects the average rise speed (sedimentation velocity) of the bubbles. This was investigated by Richardson and Zaki [1954], who found the following relation

$$u_{\rm sus} = u_{\rm s}\varepsilon^n. \tag{136}$$

Here $u_{\rm s}$ is the terminal velocity of an isolated particle as calculated in Section 7.1. Furthermore, $\varepsilon = 1-\phi_g$ is the voidage of bubbles, ϕ_g is the volume fraction of bubbles and the empirical exponent n is found to be

$$n = \begin{cases} 4.65 & \text{for } Re_t < 0.2 \\ 4.35Re_t^{-0.03} & \text{for } 0.2 < Re_t < 1 \\ 4.45Re_t^{-0.1} & \text{for } 1 < Re_t < 500 \\ 2.239 & \text{for } 500 < Re_t \end{cases} \tag{137}$$

where $Re_t = 2R\rho_{liq}u_{\rm s}/\eta$ is the Reynolds number for an isolated particle.

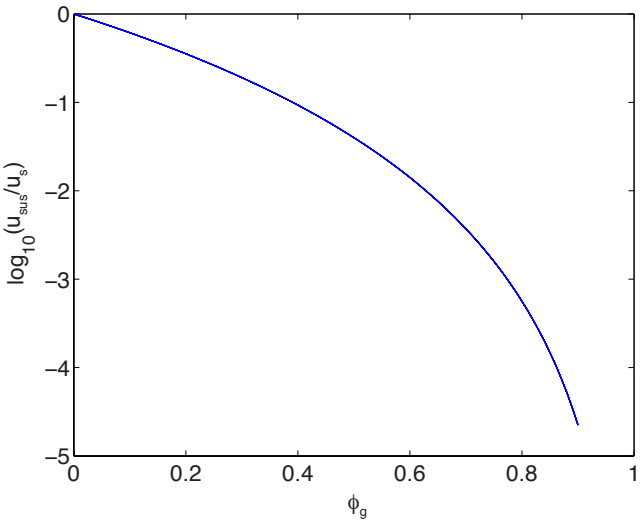

Figure 46

Rise velocity of a suspension of uniform spherical bubbles according to the Richardson-Zaki formula [Richardson and Zaki 1954].

7.3. Bubble coalescence

If two bubbles come into contact they may coalesce. Coalescence promotes the buoyant separation of the fluid phase (gas), because the rise speed of bubbles is proportional to R^2. Moreover, coalescence will also create connective pathways between bubbles through which fluid can flow. Coalescence occurs when the melt that separates the two bubbles thins to a critical thickness and can be the consequence of three different physical processes: (1) gravitational drainage of interstitial liquid, or equivalently buoyant bubble ascent, both within a relatively stagnant bulk liquid column; (2) coalescence induced coalescence, whereby shape relaxation of coalesced bubbles induces a flow field that brings nearby bubbles into sufficient proximity for coalescence, also a process that can occur in an otherwise stationary bulk fluid ; and (3) decompressive bubble growth leading to thinning of the liquid film that separates individual bubbles.

Coalescence requires the drainage of the melt film between two bubbles. This melt film will be thinnest where the two bubbles are closest in contact and will thicken in all directions from this point. In a one-dimensional film of non-uniform thickness ϵ, the local change in pressure in the melt film is given by

$$\gamma\frac{d^2\epsilon}{dR^2}, \tag{138}$$

that is, capillary pressure scales with γ/R. The hydrostatic pressure associated with the film scales as

$$\rho g \epsilon. \tag{139}$$

Equating capillary and hydrostatic pressures gives

$$\frac{\partial^2 \epsilon}{\partial R^2} = \kappa^2 \epsilon, \tag{140}$$

where $\kappa^{-1} = \rho g/\gamma$ is the capillary length scale. For length scales $R < \kappa^{-1}$ gravity is negligible and capillary effects dominate. This is generally the case for magmas, because there buoyancy forces only dominate for radii greater than a few cm.

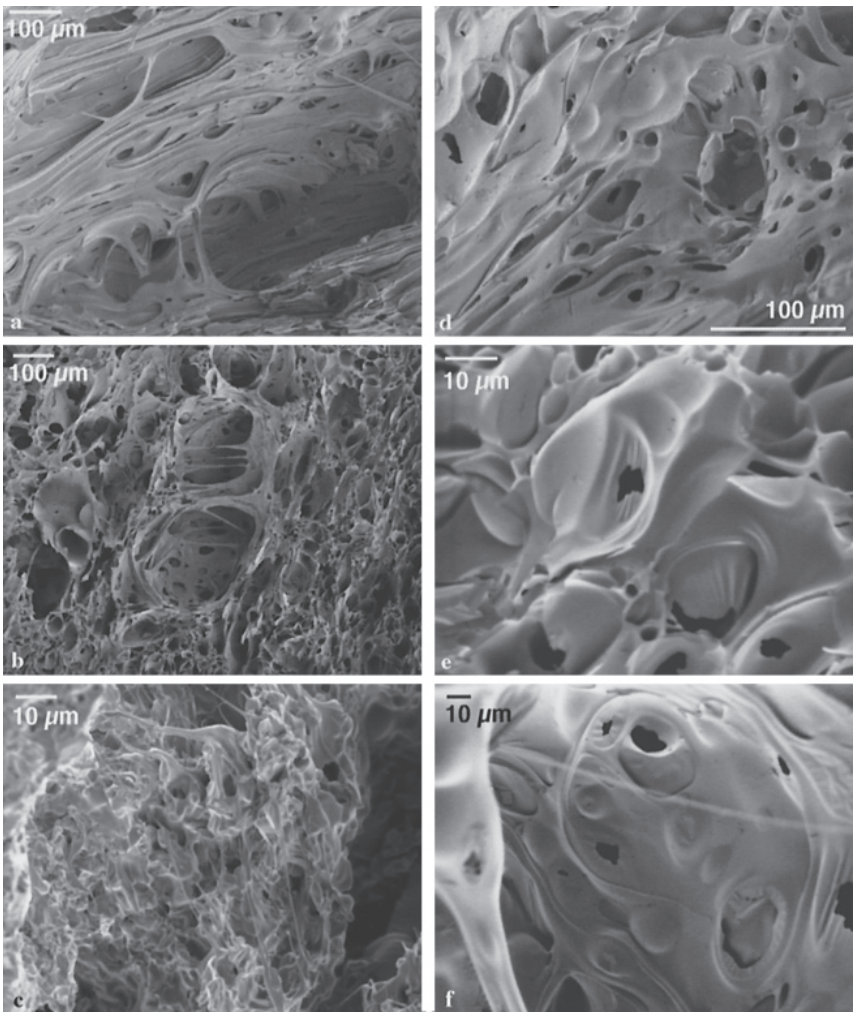

Figure 47

Figure 3 of Klug and Cashman [1996].

A film drainage velocity can be estimated by balancing the pressure gradient γ/R^2 by viscous resistance within the film $\eta v/R^2$. Here v the velocity in the film and the length scale in the viscous stress term is the radius R rather than film thickness, because the bubble-melt surface is assumed to be a free-slip surface. We thus obbtain $v \sim \gamma/\eta$, which highlights the importance of melt viscosity. However, film drainage can be enhanced by flow induced shear or by expansion of bubbles during decompression Larsen et al. [2004]. Similar to film drainage, the time scale for the coalesced composite bubble to return to a spherical shape, given by $\eta R/\gamma$, also dependents on viscosity. For example, in a basalt with $\eta \sim 10^2$ Pa s and $\gamma \sim 0.1$ N

m^{-1}, this time is $O(1)$ s for milimeter-size bubbles. Thus coalescence is expected to be most important in low viscosity magmas or more viscous magmas that are stored in the subsurface for long periods of time.

The effect of crystals on coalescence is not well characterized. Silicate crystals have a positive adhesion in silicate melts Murase and McBirney [1973]. Bubble coalescence in the presence of crystals is expected to occur by thinning of the melt film to the thickness of individual crystals, followed by rupture of the melt film adjacent to individual crystals Proussevitch et al. [1993], but is also dependent on the aspect ratio of the crystals. Moreover, crystals, especially if they are much smaller than the average bubble size, increase the viscosity of the surrounding melt-crystal mixture and, therefore, should decrease the coalescence rate Klug and Cashman [1994].

7.4. Permeable outgassing

Gas flow measurements at active silicic volcanoes indicate considerable vertical gas flow through the ascending magma Edmonds et al. [2003], Wallace et al. [2003]. In contrast to mafic magmas silicic magmas may outgas due to gas flowing through the porous and permeable magma without the requirement of differential movement of bubbles and melt Eichelberger et al. [1986], Yoshida and Koyaguchi [1999], Edmonds et al. [2003], Mueller et al. [2005]. Outgassing may also be aided by brittle magma deformation resulting in cracks and fractures amenable to enhanced gas flow Gonnermann and Manga [2003], Tuffen et al. [2003], Rust et al. [2004]. If conduit walls are permeable, which is controversial Boudon et al. [1998], and if pressure gradients are favorable, then volatiles may also flow from the ascending magma laterally into the wall rock Jaupart and Allegre [1991], Woods and Koyaguchi [1994], Jaupart [1998], Ida [2007].

7.4.1. Fluid flow through porous media. *Darcy's law* is an empirical relationship for fluid flow through a porous material. It is credited to Henry Darcy for experiments in 1856 on the flow of water through vertical columns of sand (Figure 48). Darcy's law can be expressed as

$$Q = -KA\frac{h_2 - h_1}{L}. \tag{141}$$

where Q is the volumetric flow rate, A the cross-sectional area of the porous column, L the length of the column, K a coefficient of proportionality called *hydraulic conductivity* with units of length over time. h_1 is the *piezometric head* at the inlet and h_2 the head at the outlet. Alternatively Darcy's law can be expressed in terms of the *specific discharge* or *Darcy velocity*, $q = Q/A$, defined as the discharge or volumetric flow rate per unit cross-sectional area normal to the direction of flow

$$q = -K\frac{h_2 - h_1}{L}, \tag{142}$$

The equation for pressure within a static column of fluid is given by

$$\int dp = \rho g \int dz, \tag{143}$$

which upon integration gives

$$p = \rho g z + C. \tag{144}$$

This is the *hydrostatic equation*. **Caution**, here we will use the convention that z, the vertical coordinate increases in value with depth and that $z = 0$ is at the top of whatever *system* we are considering. For example, if we are considering a fluid column of depth h and with atmospheric pressure p_0 at $z = 0$, then

$$C = p_0. \tag{145}$$

With this in mind (and assuming a fluid of constant density), we can write Equation (142) as

$$q = -\frac{K}{\rho g}\frac{p_2 - p_1}{L}, \tag{146}$$

or in general form

$$\mathbf{q} = -\frac{1}{\rho g}\mathbf{K}\,\nabla p. \tag{147}$$

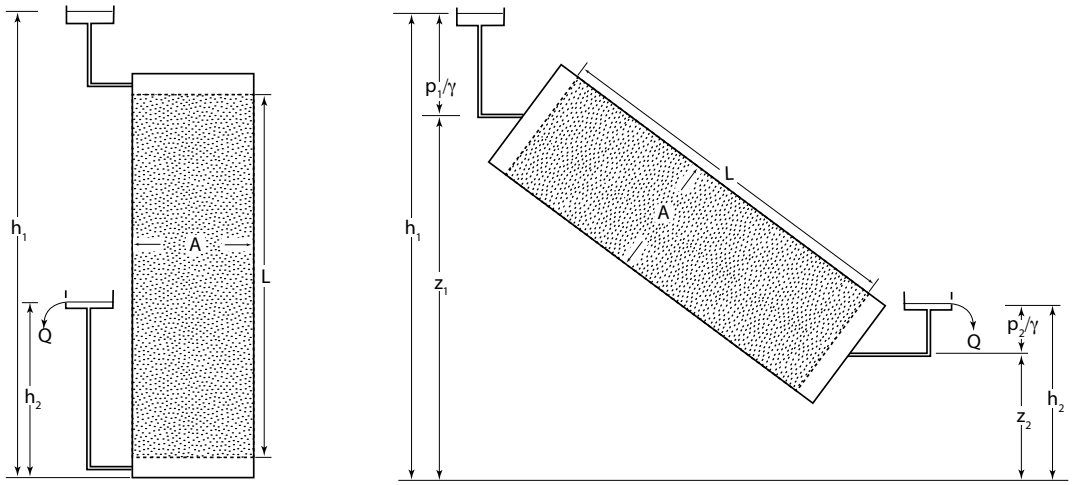

Figure 48

Darcy's experiment (left) and inclined equivalent (right).

Recall that K is an empirical constant that depends on the properties of the porous material and of the fluid. It is defined as

$$\frac{k}{\eta} = \frac{K}{\rho g}, \tag{148}$$

where k is the permeability (m^2) and η the dynamic viscosity (Pa s) of the fluid.

A fundamental requirement for the applicability of Darcy's law is that the flow in the individual pores is laminar, as opposed to turbulent. This can be quantified in terms of a *Reynolds number based on average grain diameter, δ*, $\mathrm{Re} = q\delta\rho/\eta$, and requires that $\mathrm{Re} < 1 - 10$ (Figure 49). Just like the Reynolds

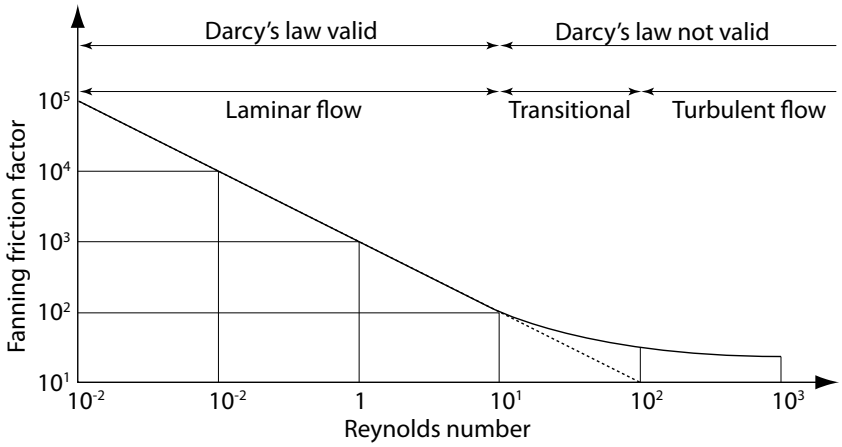

Figure 49

Relationship between Fanning's friction factor and Reynolds number for flow through porous media. The line represents the approximate fit to compiled experimental data and for laminar flow $f \approx 1000/\mathrm{Re}$.

number for other types of flows, this Reynolds number is a dimensionless number expressing the ratio of inertial to viscous forces and is used as a criterion to distinguish between laminar flow at low velocities from turbulent flow at higher velocities. The transition from laminar to turbulent flow can be seen when experimental data are plotted in terms of a friction factor. Friction factors are empirical functions of the Reynolds number and are used in fluid mechanics to relate the pressure gradient that drives a flow, typically through a pipe or duct of some given geometry, to the resulting flow rate (velocity). If the flow is laminar friction pressure (energy) loss is solely due to fluid viscosity. If the flow is turbulent, then there

is additional pressure (energy) loss associated with *turbulent eddies* (i.e., the flow is more complex and all the eddies and currents due to turbulence add to the overall viscous loss of energy). Consequently, graphs of friction factor vs. Reynolds number will show a change in slope or curvature at the transition between laminar (low Re) and turbulent (high Re) flow. This is shown for flow through a porous medium in Figure 49 for the *Fanning friction factor*, f_F, defined as

$$\frac{dp}{dz} = f_F \frac{2}{\delta} \rho \bar{u}^2, \tag{149}$$

where $\delta/4$ is the *hydraulic radius* of the capillary and $\bar{u} = q/\phi$. To account for intertial dissipation effects during porous flow, Austrian scientist Phillip Forchheimer (1901) investigated fluid flow through porous media in the high velocity regime. During this study, he observed that as the flow velocity increases, the inertial effects start dominating the flow. In order to account for these high velocity inertial effects, he suggested the inclusion of an inertial term representing the kinetic energy of the fluid to the Darcy equation. *Forchheimer's equation* adds a term that depends on velocity square, relative to Darcy's equation

$$\frac{\Delta P}{L} = \frac{\mu}{k_1} q + \frac{\rho}{k_2} q^2, \tag{150}$$

where k_1 *is the Darcian permeability* or equivalently *intrinsic permeability*, ρ is the fluid density and k_2 is called the *Forchheimer coefficient* or also referred to as the *inertial permeability*.

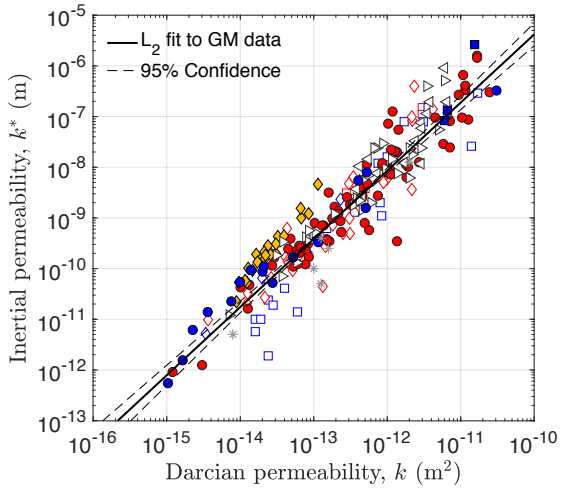

Figure 50

The relationship between Darcian and inertial permeability in rhyolitic samples.

7.4.2. Permeability. Permeability depends on the geometry, tortuosity and abundance of "channels" or "flow pathways" through the porous material. Permeability estimates are often empirically based, with k a function of grain or pore size and material porosity. There are many theoretical models for permeability in a porous material and a good discussion is provided by Bear - *Dynamics of Fluids in Porous Materials* (1988). The simplest model assumes that the porous medium is made up of a capillary tubes. The basic model assumes that the capillaries are circular in cross section, straight, aligned in the direction of flow, with flow through the capillaries being laminar and governed by the Hagen-Poiseuille equation. To make such a model more realistic is to assume that the diameter of the capillary tubes is not uniform. Further variants assume that the diameter of individual capillaries varies along the flow direction and that the capillary tubes are no longer straight, but tortuous. Alternatively, the porous material can be represented as narrow capillary fissures or slits, perhaps most applicable to fractured rock.

One idealized *capillary tube model* is based on a cubical matrix of circular tubes of diameter δ with a distance of b between tube centers (Figure 51). In this model each cubical element contains 1/4 of a tube with volume $\pi b(\delta/2)^2$ on each of its 12 edges. Thus the total volume of "pore space" comprised by these

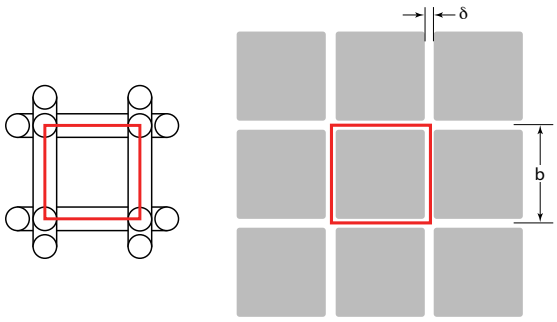

Figure 51

An idealized model of a porous medium.

tubes for one cubical element of volume b^3 is $3\pi\delta^2 b/4$. Therefore the porosity is given by

$$\phi = \frac{3\pi\delta^2}{4b^2}. \tag{151}$$

To obtain the Darcy velocity through this porous medium we assume a one-dimensional flow in the x-direction. If the flow through the tube is laminar, the mean velocity is given by

$$\bar{u} = -\frac{\delta^2}{32\mu}\frac{dp}{dx}. \tag{152}$$

Consequently the mean velocity per unit area perpendicular to the flow direction is

$$q = \frac{\pi\delta^2}{4b^2}\bar{u} = \frac{\phi}{3}\bar{u} = -\frac{\phi}{96}\frac{\delta^2}{\mu}\frac{dp}{dx}. \tag{153}$$

Therefore, for this highly idealized porous material

$$k = \frac{\phi\delta^2}{96} = \frac{\phi^2 b^2}{72\pi} = \frac{\pi}{128}\frac{\delta^4}{b^2}. \tag{154}$$

Let's return to a simplified version of the capillary tube model, and consider a cylindrical inclined tube passing through a solid block (Figure 52).

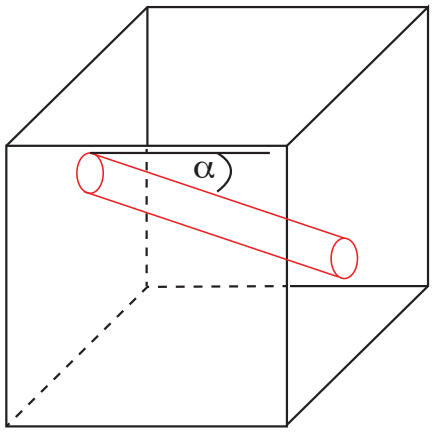

Figure 52

Capillary tube of radius, $\delta/2$, and inclined at angle α passing through a cube of side length L

$$\bar{u} = -\frac{\delta^2}{32\mu}\frac{\Delta p}{L\tau} = -\frac{\delta^2}{32\mu\tau}\frac{dp}{dx}, \tag{155}$$

where we shall call $\tau = 1/\sin(\alpha)$ the *tortuosity*. The porosity of this block is given by

$$\phi = \frac{V_{\rm tube}}{V_{\rm cube}} = \frac{\pi\delta^2 L\tau}{4}/L^3 = \frac{\pi\delta^2\tau}{4L^2} \tag{156}$$

and

$$q = \bar{u}\frac{\pi\delta^2}{4L^2} = -\frac{\pi\delta^2}{4L^2}\frac{\delta^2}{32\mu\tau}\frac{dp}{dx} = -\phi\frac{\delta^2}{32\mu\tau^2}\frac{dp}{dx}. \tag{157}$$

Consequently,

$$k = \frac{\phi\delta^2}{32\tau^2}. \tag{158}$$

Lets define the *specific surface*, M, defined as the total interstitial surface area of the pores per volume of solid. For the included capillary tube model

$$M = \frac{\pi\delta L\tau}{L^3} = \frac{4\phi}{\delta} \tag{159}$$

Lets expresses the permeability in terms of porosity, ϕ, specific surface area, M, and tortuosity, τ, to obtain

$$k = \frac{\phi^3}{2M^2\tau^2} \tag{160}$$

and redefine the specific surface as the total interstitial surface area of the pores per volume of solid, $M_s = M/(1-\phi)$ and rewrite the equation for k in terms of M_s

$$k = \frac{\phi^3}{2M_s^2(1-\phi)^2\tau^2}. \tag{161}$$

Equation (161) is known as the *Kozeny-Carman equation* with a value $\tau^2 = 5$ found by Carman [1937]. It is also possible to define some mean particle size by $d_m = 6/M_s$ to express the Kozeny-Carman equation as

$$k = \frac{d_m^2}{c}\frac{\phi^3}{(1-\phi)^2}, \tag{162}$$

where $c = 180$ [Carman 1937, Bear 1988]. Modifications of this equation to account for different *turtuosities* of the fluid pathway may allow for different values of c.

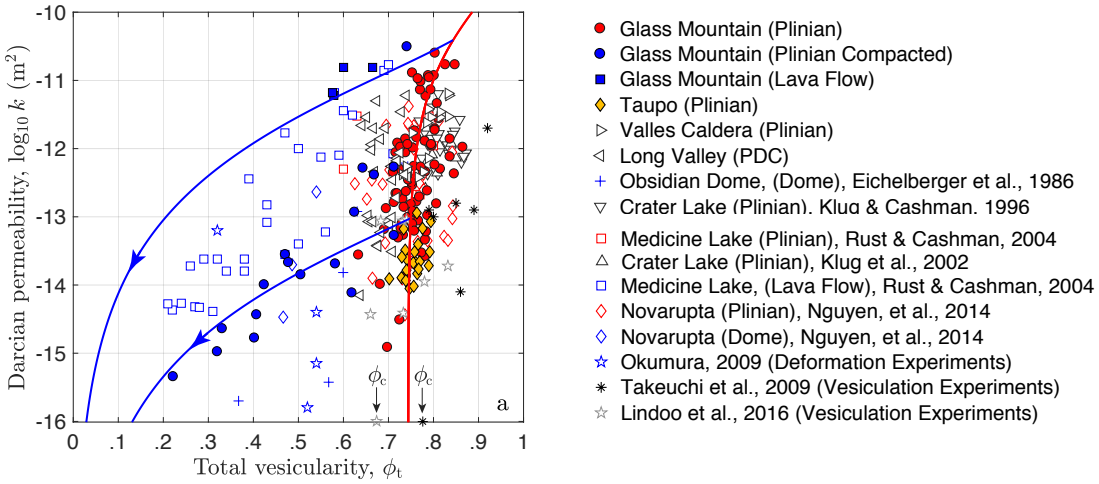

Figure 53

Data from rhyolitic explosive and effusive eruptions, and experiments. Log of Darcian permeability, k, as a function of total vesicularity, $\phi_{\rm t}$. The blue and red curves are empirical fits to the data. The arrows labeled $\phi_{\rm cr}$ indicate the maximum value of $\phi_{\rm t}$ for which permeabilities were below the detection limit. The range in permeabilities corresponds to that of sandstones and sands.

KOZENY-CARMAN EQUATION

There are various adaptations of the Kozeny-Carman equation in the literature and it is common to see porosity permeability relations of the form

$$k = c\ \phi^n, \tag{163}$$

or

$$k = c\,(\phi - \phi_{\rm cr})^n\,, \tag{164}$$

or

$$k = c\ d^2\phi^n. \tag{165}$$

All of the above are often referred to as Kozeny-Carman equations, where typically $2 \leq n \leq 3$, as well as c are used as fitting parameters. Similarly, $\phi_{\rm cr} \approx 0.3$ is thought to represent the *percolation threshold* below which the material is impermeable. Often it is simply used as fitting parameter.

8. Separated two-phase (gas-liquid) flow

I will focus on gas-melt flow below fragmentation. Similar equations govern the flow above fragmentation. For simplicity, crystals are not treated as a separate phase, although their presence can often be accounted for if the liquid phase is assumed to be a homogeneous mixture of melt plus crystals.

8.1. Approximating volatile diffusion

It is assumed that the flux of volatile species i, where for example $i = CO_2$ and/or $i = H_2O$, is given by

$$\Gamma_i \equiv 4\pi R^2 N D_i \rho_m (1-\phi)\frac{C_{s,i} - C_i}{R} \quad \Rightarrow \quad \left[\frac{\rm M_{volatile}}{\rm M_{melt} \times Time}\right]. \tag{166}$$

Here, D_i is diffusivity, N is bubble number density, $C_{s,i}$ is the solubility at pressure, P_g, and C_i is the average concentration of volatile i dissolved in the melt at depth, z. The rate of change in concentration is given by

$$\frac{\partial C_i}{\partial t} + u_m \frac{\partial C_i}{\partial z} = \frac{\Gamma_i}{\rho_m(1-\phi)} = -4\pi R^2 N D_i \frac{C_i - S_i}{R} \quad \Rightarrow \quad \left[\frac{\rm M_{volatile}}{\rm M_{melt} \times Time}\right] \tag{167}$$

8.2. Conservation of mass of melt

$$\frac{D}{Dt}\Big\{(1-\phi)\rho_m(1-C)A\Big\} + (1-\phi)\rho_m(1-C)A\frac{\partial u_m}{\partial z} = 0 \tag{168}$$

or equivalently

$$\frac{\partial}{\partial t}\Big\{(1-\phi)\rho_m A\Big\} + u_m \frac{\partial}{\partial z}\Big\{(1-\phi)\rho_m A\Big\} + (1-\phi)\rho_m A\frac{\partial u_m}{\partial z} = \frac{(1-\phi)\rho_m A}{1-C}\frac{\partial C}{\partial t} + \frac{u_m(1-\phi)\rho_m A}{1-C}\frac{\partial C}{\partial z} \tag{169}$$

8.3. Conservation of mass of gas

$$\frac{D}{Dt}\Big\{\phi\rho_g A\Big\} + \phi\rho_g A\frac{\partial u_g}{\partial z} = -\frac{(1-\phi)\rho_m A}{1-C}\,\frac{DC}{Dt} \tag{170}$$

8.4. Momentum balance melt

According to Ishii & Hibiki's (*Thermo-Fluid Dynamics of Two-Phase Flow*, 2011) Eq. 9-11, with interfacial momentum flux defined by Eq. 9-100, and neglecting lift and virtual mass forces the continuous phase momentum equation is given by

$$\begin{aligned}\frac{D}{Dt}\Big\{\rho_m(1-\phi)u_m\Big\} + u_m\rho_m(1-\phi)\frac{\partial u_m}{\partial z} = &-\frac{\partial}{\partial z}\Big\{(1-\phi)P_m\Big\} + P_i\frac{\partial(1-\phi)}{\partial z} \\ &+ u_m\Gamma - \rho_m(1-\phi)g + F_{mg} - F_{mw}\end{aligned} \tag{171}$$

or equivalently

$$\frac{\partial}{\partial t}\Big\{\rho_m(1-\phi)u_m\Big\}+\frac{\partial}{\partial z}\Big\{\rho_m(1-\phi)u_m^2\Big\}=-\frac{\partial}{\partial z}\Big\{(1-\phi)P_m\Big\}+P_i\frac{\partial(1-\phi)}{\partial z} \\ +u_m\Gamma-\rho_m(1-\phi)g+F_{mg}-F_{mw}. \tag{172}$$

8.5. Momentum balance gas

Similarly, Ishii & Hibiki's (*Thermo-Fluid Dynamics of Two-Phase Flow*, 2011) equation of motion for the dispersed gas phase is given by

$$\frac{\partial}{\partial t}\Big\{\rho_g\phi u_g\Big\}+u_g\frac{\partial}{\partial z}\Big\{\rho_g\phi u_g\Big\}=-\frac{\partial}{\partial z}\Big\{\phi P_g\Big\}-\rho_g\phi g-u_g\Gamma+P_i\frac{\partial\phi}{\partial z}-F_{gm}-F_{gw}. \tag{173}$$

8.6. Friction factors

Below fragmentation the melt-wall friction is given by

$$F_{mw}=\rho u_m^2\frac{f_D}{4a_c}, \tag{174}$$

where a_c is the conduit radius and f_D is the Darcy-Weissbach friction factor. Note that the factor of $1/4$ associated with f_D arises because the Darcy-Weissbach friction factor equals $1/4$ the Fanning friction factor. Above fragmentation one can approximate $F_{mw}\approx 0$. Below fragmentation the gas-melt friction in the case of permeable flow is given by

$$F_{gm}=\phi\left(\frac{\mu_g}{k}+\frac{\rho_g}{k_2}\left|u_g-u_m\right|\right)\Big(u_g-u_m\Big). \tag{175}$$

Similarly, a friction factor approximation can be used in the case of buoyant bubble rise (recall, for example, Richardson-Zaki). Lastly, it is usually assumed that

$$F_{gw}=0. \tag{176}$$

8.7. Pressures

The interface pressure, P_i is often assumed equal to P_g or P_m. As a consequence a ΔP term arises in one of the momentum equations. As I have shown in the previous discussion for bubble growth, ΔP can be expressed in terms of $\partial u_z/\partial z$, for example. This is essentially the approach taken by, for example, Michaut et al., *Nature Geoscience*, 2013.

8.8. Ill posedness

The two-phase flow equations in the form presented above are *ill posed*, something long recognized in the engineering community. To overcome this problem and obtain a system of solvable equations, frequently additional terms are added, for example a *virtual mass* term. Not surprisingly, it quickly becomes bewildering trying to figure out what equations one should use or how to calculate terms like *virtual mass*. Moreover, most of the time it is assumed that $P_g=P_m=P$. Recently a new set of equations has been proposed by Romenski et al. [2007] and applied to volcanic eruptions, for example, by La Spina et al. [2017], which is in my personal opinion the current state of the art in conduit modeling.

The equations can, however, be solved without too much hassle, if one assumes steady state and $P_g=P_m=P$. This was done by Degruyter et al. [2012], who explored permeable outgassing and its effect on the transition between effusive and explosive eruptions.

9. Rheology

9.1. Introduction to nonNewtonian rheology

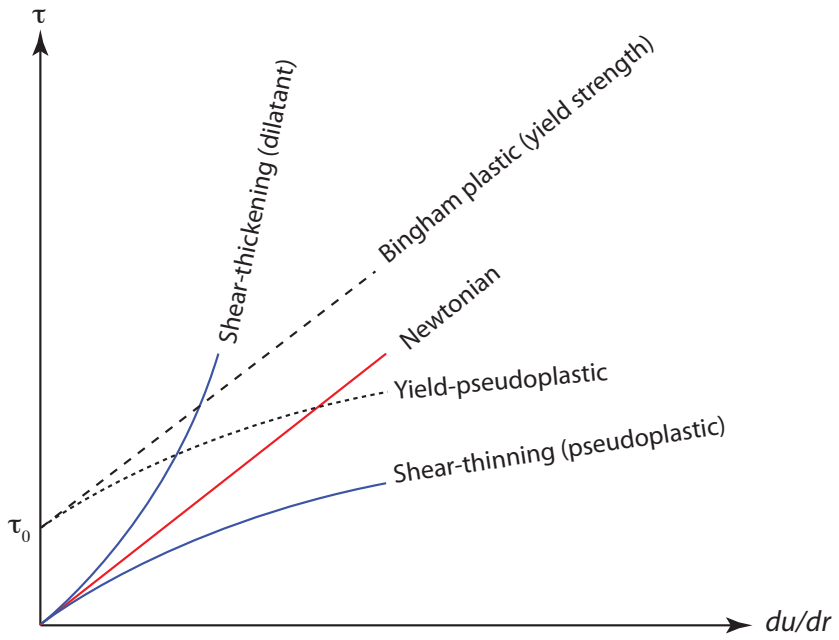

Figure 54

Types of time-independent flow behavior.

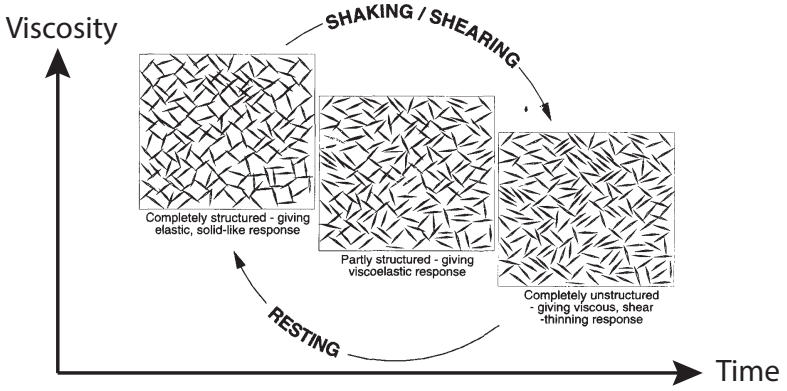

Figure 55

Modified from Figure 1 of Barnes [1997]. Structure of time-dependent shear thinning material (thixotropic). The longer the material is stressed (deformed) the lower its viscosity gets.

9.1.1. Some mathematical models for nonNewtonian fluid behavior. There are a large number of mathematical models that describe different types of nonNewtonian fluid behavior. Some of the main ones are listed below.

Power-law or Ostwald de Waele model (shear thinning)

$$\tau = m\left(\frac{du}{dr}\right)^n, \tag{177}$$

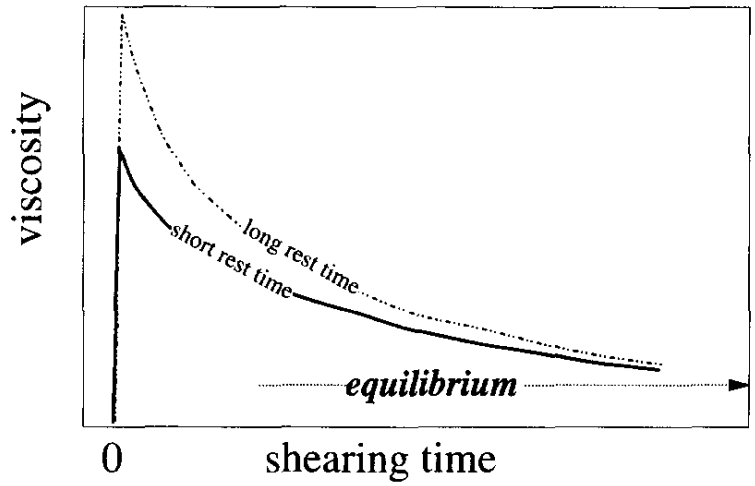

Figure 56

Figure 2 of Barnes [1997]. Thixotropic (time-dependent shear thinning) flow behavior.

where m and n are empirical fitting parameters, known as the *fluid consistency coefficient* and the *flow behavior index* respectively. For shear thinning, $0 < n < 1$. For peanut butter $n = 0.07$ and $m = 500$ Pa s^n and for toothpaste $n = 0.28$ and $m = 120$ Pa s^n.

Carreau viscosity equation (shear thinning)

$$\frac{\mu - \mu_\infty}{\mu_0 - \mu_\infty} = \left[1 + \left(\lambda \frac{du}{dr}\right)^2\right]^{(n-1)/2}, \tag{178}$$

where μ_0 is the *apparent viscosity* at low shear rates and μ_∞ is the apparent viscosity at high shear rates. Apparent means the viscosity that is measured under given conditions. $n < 1$ and λ are fitting parameters.

Cross viscosity equation (shear thinning)

$$\frac{\mu - \mu_\infty}{\mu_0 - \mu_\infty} = \frac{1}{1 + k\left(\frac{du}{dr}\right)^n}, \tag{179}$$

where $n < 1$ and k are fitting parameters.

Bingham plastic model (yield strength)

$$\begin{aligned} \tau &= \tau_0 + \mu_B \frac{du}{dr} \text{ for } |\tau| > |\tau_0| \\ \tau &= 0 \text{ for } |\tau| < |\tau_0|, \end{aligned} \tag{180}$$

where τ_0 the yield strength and μ_B are fitting parameters.

9.2. Silicate melt structure and viscosity

KEY CONCEPTS

- Bridging oxygens
- Non-bridging oxygens (NBO)
- Configurational entropy
- Structural relaxation
- Vogel-Fulcher-Tammann (VFT) equation
- H_2O depolymerizes silicate melt

- Viscoelasticity
- Maxwell model
- Glass transition (relaxed and unrelaxed response)
- Relaxation timescale

Part of the following text is borrowed from Gonnermann and Manga [2007]. Silicate melts form a disordered network of interconnected SiO_4 tetrahedra. Structural relaxation, the self-diffusive motion of atoms results in a continuous, unstructured rearrangement of the average molecular structure. This, in part, allows for viscous deformation of silicate melts [Moynihan 1995]. The intrinsic viscosity of silicate melts varies over orders of magnitude, and is related to the degree of polymerization, which depends on chemical composition and volatile content [e.g. Zhang et al. 2007], so that melt viscosities may vary over many orders of magnitude, even for magma within a single volcanic eruption.

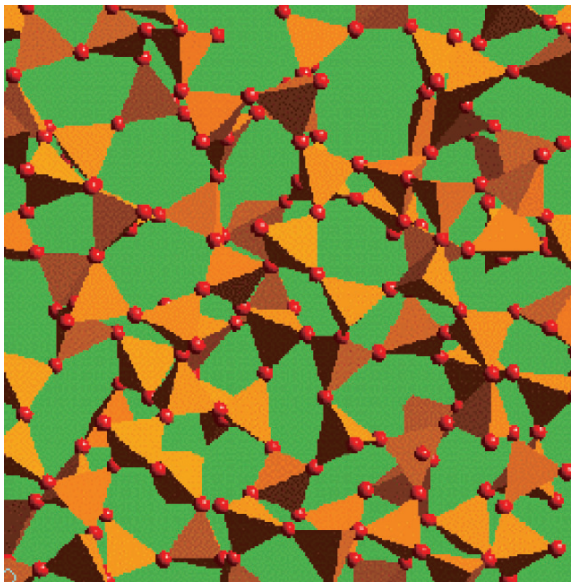

Figure 57

Amorphous assemblage of SiO_4 tetrahedra characteristic of *glass*.

SiO_4 tetrahedra may be linked, or *configured*, into polymeric structural units via *bridging oxygens*. However, not all SiO_4 tetrahedra are linked by Si-O bonds and oxygen that do not link adjacent tetrahedra are called *non-bridging oxygen* (NBO). The bridging oxygen bonds (Si-O bonds) randomly break and and reform, resulting in a continuous structural reorganization. If the SiO_4 structure of a subliquidus melt becomes strained by deformation, the random breaking and reforming of Si-O bonds results in a *structural relaxation*, that is viscous flow. Based on nuclear magnetic resonance (NMR) spectroscopic studies it has been found that the exchange of oxygens between bridging and non-bridging oxygens occurs at the microsecond to nanosecond time scale at liquidus temperatures [Lange 1994]. In part, based on these observations the viscosity of structurally (compositionally) "simple" melts can be described by an *Eyring model* of viscosity

$$\eta = \frac{k_B T \tau_0}{d^3}, \tag{181}$$

where $1/\tau_0 = \Omega_0$ represents the exchange (jump) frequencies of the Si-O bonds, T is temperature, k_B is Boltzmann's constant, and d is the jump distances taken as the Si-Si distance of 0.3 nm [Lange 1994]. The characteristic jump time, τ_0, is inversely proportional to what is known as the *configurational entropy*, $S^{conf}(T)$, which is based on the Adam and Gibbs [1965] *configurational entropy theory of relaxation*. In this theory it is assumed that viscous flow occurs through the cooperative rearrangement of configurational states in the liquid. The configurational state represents how and/or with how many O_2^- the Si_4^+ cation

coordinates. If it coordinates with four O_2^- a silica tetrahedron is formed. However, Si_4^+ may enter into other coordinations, such as three-fold, four-fold, six-fold and eight-fold coordination.

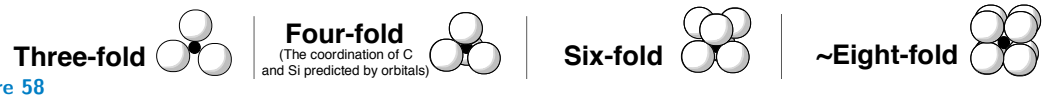

Figure 58

Examples of Si_4^- coordination.

The more configurational states are available to the liquid, the more readily viscous flow occurs. Richet [1984] and Richet et al. [1986] showed that this theory of relaxation can be applied to changes in viscosity with temperature for many silicate and aluminosilicate liquids using the relation

$$\ln \eta = A_e + \frac{B_e}{T\ S^{\text{conf}}(T)}, \tag{182}$$

where A_e is a pre-exponential term and B_e is a potential energy barrier hindering the structural rearrangement of the liquid [Lange 1994]. The rate of structural rearrangement in the absence of an imposed stress is

$$\Omega_0 = \frac{1}{\tau_0} \exp\left(-\frac{\Delta H}{k_B T}\right), \tag{183}$$

where ΔH is the *activation enthalpy barrier* that must be overcome for structural rearrangement to occur at a given Si (under constant pressure conditions the change in the internal energy of the system, plus the work that the system has done on its surroundings is defined as the change in enthalpy, in other words, the heat absorbed by a chemical reaction). Under an applied shear stress, σ, the activation barrier is lowered to $\Delta H - V_A \sigma$, where V_a is the *activation volume* (the difference between the partial molar volumes of the transition state for a reaction and the sums of the partial volumes of the reactants at the same temperature and pressure). Within this framework, the structural relaxation time is defined as

$$\tau = \tau_0 \exp\left(\frac{\Delta H}{k_B T}\right), \tag{184}$$

where the exponential dependence of τ on inverse temperature is called an *Arrhenius* form. Consequently, a frequently used expression for the temperature dependence of silicate melt viscosity on temperature is expressed in a so-called Arrhenian model

$$\eta = \eta_0 \exp\left(\frac{E_a + pV_a}{RT}\right), \tag{185}$$

where n_0 is the asymptotic viscosity at infinite temperature, E_a is the activation energy for viscous flow (constant for an Arrhenian fluid) and R is the universal gas constant. Increasing the concentration of non-framework components, such as alkalis, alkaline earths and H_2O, results in the creatin of oxygens bridged to only a single Si or Al, as well as nonbridging oxygen (NBO). This destroys the network structure of the melt created by the formation of tetrahedral rings and serves to lower both η_0 and E_a [Lange 1994]. Figure 9.2 shows an example of the Arrhenian temperature dependence of dacite melts at different dissolved water contents.

Not all silicate melts follow the Arrhenian temperature-viscosity relationship and an empirical relation for predicting the temperature dependence of viscosity for non-Arrhenian melts is the *Vogel-Fulcher-Tamman* (VFT) equation, which can be expressed as

$$\log_{10} \eta = A + \frac{B}{T - C}, \tag{186}$$

where A, B and C are fitting parameters [e.g., Whittingon et al. 2009].

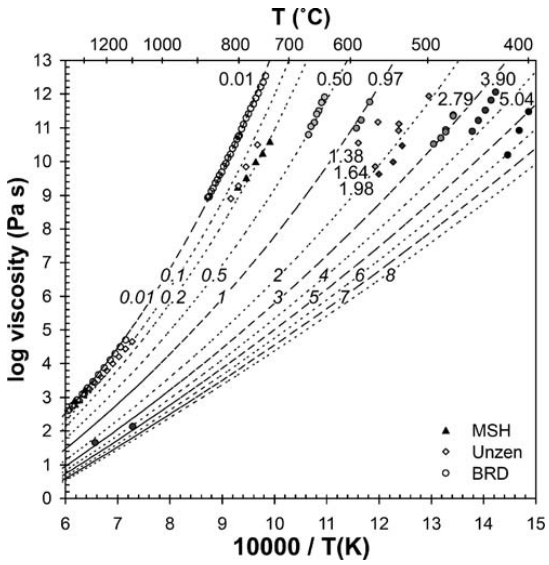

Figure 59

Figure 4 of Whittington et al. [2009]. Viscosity data for hydrous dacites. Circles are synthetic dacite; diamonds are Unzen dacite; triangles are Mount St. Helens dacite. Hydrous samples are labeled with water content in weight percent. Lines are viscosity of synthetic dacite for indicated water contents using a *Vogel-Fulcher-Tammann (VFT) equation*.

As already mentioned, the presence of H_2O *depolymerizes* the melt structure, thereby lowering the viscosity. H_2O dissolves in silicate melts and glasses as a combination of molecular water, $H_2O_{molecular}$ and hydroxyl groups, OH^- with the following equilibrium

$$H_2O_{molecular}(melt) + O^{2-}(melt) = 2OH^-(melt). \tag{187}$$

The required "consumption" of O^{2-} by this reaction results in the depolymerization, that is breakage of Si-O bonds, of the melt structure, thereby increasing the number of available configurational states.

Overall, the dependence of melt viscosity on water content and temperature is less pronounced for mafic magmas [e.g., Giordano et al. 2006, Hui and Zhang 2007]. While CO_2 also affects viscosity [Bourgue and Richet 2001], it is not nearly as abundant as H_2O in silicic magmas, whereas in mafic magmas, where CO_2 and H_2O can be equally abundant, viscosity variations with volatile content are less pronounced. Because there have been very few studies on the effect of CO_2 or halogens on melt viscosity, this remains a very active area of research. Although several thermodynamically based formulations for melt viscosity as a function of composition, water content and temperature exist, a general and universally applicable formulation does not yet exist (see review by Zhang et al. [2007]). A alternate approach is to find a purely empirical fit to a broad range of viscosity data for natural melts. This is the approach taken by Hui and Zhang [2007], which has resulted in a relatively accessible and "simple" equation applicable to natural silicate melts with viscosities $< 10^{15}$ Pa s, temperatures > 573 K, and water contents ≤ 5 wt.% for melts other than rhyolite (up to 12.3 wt. % for rhyolite). Figure 9.2, based on the formulation of Hui and Zhang [2007], shows that within realistic ranges of compositional variability, eruptive temperatures and volatile content, viscosity of crystal-and-vesicle free basalt liquids may vary by up to 2 order of magnitude [e.g., Giordano and Dingwell 2003, Hui and Zhang 2007]. This variability is much larger for silicic melts [e.g., Geschwind and Rutherford 1995, Barclay et al. 1998]. Beyond the dynamical aspects of bubbly flows, the viscosity of bubbly magma may vary significantly as the volume fraction of bubbles increases [e.g., Lejeune et al. 1999, Manga and Loewenberg 2001, Llewellin et al. 2002, Pal 2003, 2004, Llewellin and Manga 2005]. Moreover, the presence of crystals or microlites, which may reach up to 90% in some magmas, will significantly increase magma viscosity [Lejeune and Richet 1995, Stevenson et al. 1996, Saar et al. 2001, Pal 2002, Deubener 2003, Costa 2005, Arbaret et al. 2007, Caricchi et al. 2007, Lavallee et al. 2007]. It can therefore be concluded that the rheological effects of bubbles and crystallinity are important potential factors modulating eruption dynamics.

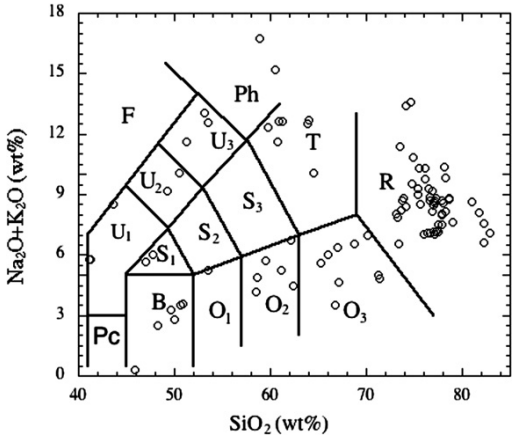

Figure 60

Figure 5 of Hui and Zhang [2007] showing the compositions of samples used to calibrate their empirical viscosity formulation.

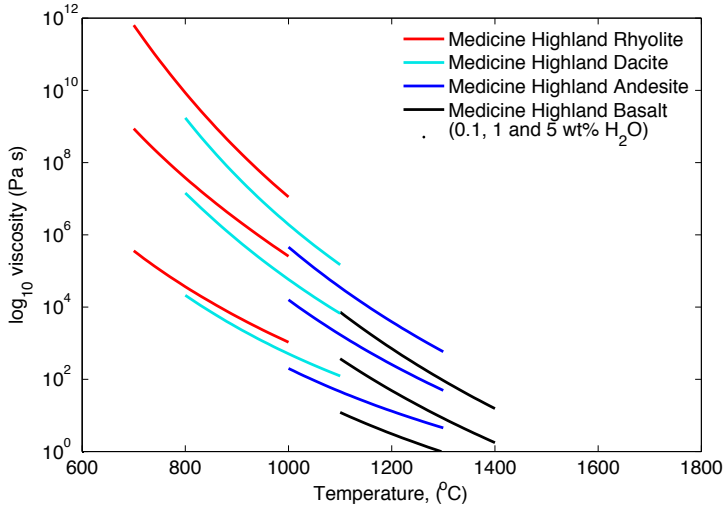

Figure 61

Viscosity as a function of temperature for natural melts using the viscosity formulation of Hui and Zhang [2007].

$$
\begin{aligned}
\log \eta = \big[& -6.83 X_{\mathrm{SiO_2}} - 170.79 X_{\mathrm{TiO_2}} - 14.71 X_{\mathrm{Al2O3,ex}} \\
& - 18.01 X_{\mathrm{MgO}} - 19.76 X_{\mathrm{CaO}} + 34.31 X_{\mathrm{(Na,K)2Oex}} \\
& - 140.38 Z + 159.26 X_{\mathrm{H_2O}} - 8.43 X_{\mathrm{(Na,K)_{AlO_2}}} \big] \\
& + 1000 [18.14 X_{\mathrm{SiO_2}} + 248.93 X_{\mathrm{TiO_2}} \\
& + 32.61 X_{\mathrm{Al2O3,ex}} + 25.96 X_{\mathrm{MgO}} + 22.64 X_{\mathrm{CaO}} \\
& - 68.29 X_{\mathrm{(Na,K)2Oex}} + 38.84 Z - 48.55 X_{\mathrm{H_2O}} \\
& + 16.12 X_{\mathrm{(Na,K)_{AlO_2}}}] / T + \exp\{ [21.73 X_{\mathrm{Al2O3,ex}} \\
& - 61.98 X_{\mathrm{(Fe,Mn)O}} - 105.53 X_{\mathrm{MgO}} \\
& - 69.92 X_{\mathrm{CaO}} - 85.67 X_{\mathrm{(Na,K)2Oex}} + 332.01 Z \\
& - 432.22 X_{\mathrm{H_2O}} - 3.16 X_{\mathrm{(Na,K)_{AlO_2}}}] \\
& + 1000 [2.16 X_{\mathrm{SiO_2}} - 143.05 X_{\mathrm{TiO_2}} - 22.1 X_{\mathrm{Al2O3,ex}} \\
& + 38.56 X_{\mathrm{(Fe,Mn)O}} + 110.83 X_{\mathrm{MgO}} \\
& + 67.12 X_{\mathrm{CaO}} + 58.01 X_{\mathrm{(Na,K)2Oex}} + 384.77 X_{\mathrm{P_2O_5}} \\
& - 404.97 Z + 513.75 X_{\mathrm{H_2O}}] / T \},
\end{aligned}
$$

Figure 62

Empirical viscosity model of Hui and Zhang [2007].

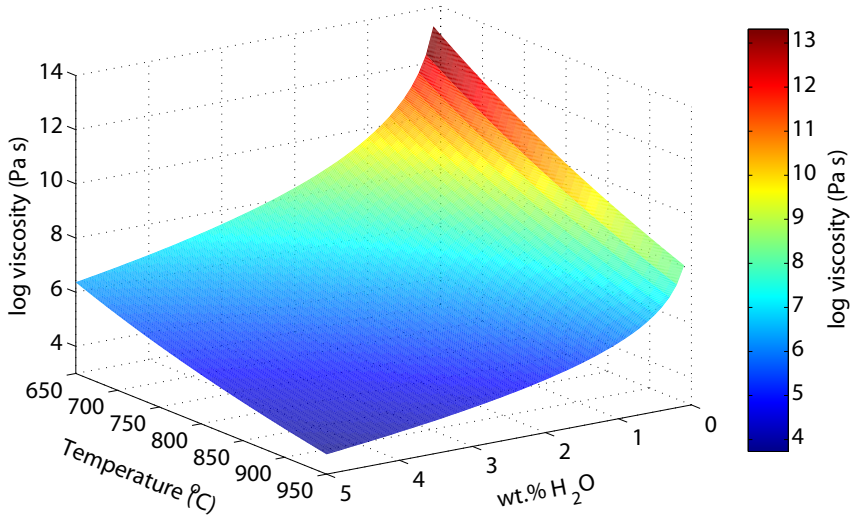

Figure 63

Viscosity for granitic melt based on work by Hess and Dingwell [1996].

9.3. Strain-Rate dependence of silicate melt

Silicate melts flow, that is they deform viscously, because of molecular motions that result in a random reordering of the melt structure called structural relaxation. If the imposed rate of flow deformation exceeds the flow relaxation rate, a measure of the structural relaxation [Moynihan 1995], the melt structure becomes disrupted. This is manifested in a decrease in viscosity from its "relaxed", or Newtonian, value and has been observed experimentally [Webb and Dingwell 1990a,b, Deubener and Brückner 1997, Thies 2002]. The critical strain rate at which the onset of shear-thinning behavior is observed is inversely proportional to the Newtonian viscosity and can be defined in terms of the viscous relaxation time as $\tau_r = \eta_{melt}/G_\infty$ as [Yue and Brückner 1994, Simmons 1998]

$$\dot{\varepsilon}_{st} \sim \frac{10^{-4}}{\tau_r}, \tag{188}$$

where $G_\infty \sim 10^{10}$ is the shear modulus and η_{melt} is the Newtonian melt viscosity. At shear strain rates considerably higher than the onset of nonNewtonian behavior, the induced molecular motions are no longer compensated by random reordering of the melt structure, resulting brittle failure of the melt Webb and Dingwell [1990a,b], Yue and Brückner [1994] This transition from viscous flow to structural failure is called the glass transition. For a wide range of melt compositions and temperatures, structural failure occurs at the critical strain rate [Webb and Dingwell 1990b]

$$\dot{\varepsilon}_f \sim \frac{10^{-2}}{\tau_r}, \tag{189}$$

which has important consequences for magma fragmentation [Dingwell 1996].

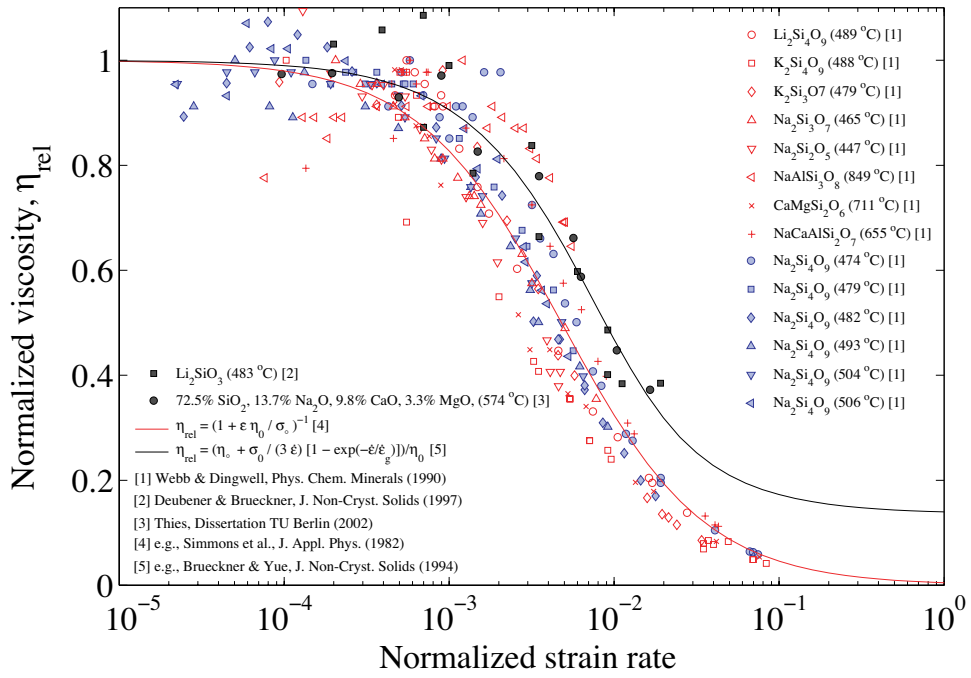

Figure 64

Strain-rate-dependent viscosity of silicate melts. Measurements are published in Brückner & Yue (1994), Deubener&Brückner (1997), Simmons et al. (1982), Thies (2002),and Webb & Dingwell (1990).

9.4. Viscoelasticity and glass transition

9.4.1. Maxwell model. The simplest mechanical model of a linear viscoelastic material is attributed to Maxwell (1867) is a series combination of a viscous dashpot with Newtonian viscosity, η, and a Hookean spring with elastic modulus, G, (or its inverse, compliance).

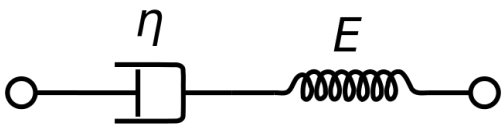

Figure 65

The dashpot-spring model of a viscoelastic material.

The constitutive equation for the spring is

$$\varepsilon_1 = \frac{1}{E}\sigma, \tag{190}$$

where ε is strain, E is the stiffness of the spring and proportional to the elastic modulus, and σ is the applied stress. Differentiation gives

$$\dot{\varepsilon_1} = \frac{1}{E}\dot{\sigma}, \tag{191}$$

The constitutive equation for the dashpot is

$$\dot{\varepsilon_2} = \frac{1}{\eta}\sigma. \tag{192}$$

Integration gives

$$\varepsilon_2 = \frac{\sigma_0}{\eta}t \tag{193}$$

Given that the Maxwell model has dashpot and spring *in series*,

$$\varepsilon = \varepsilon_1 + \varepsilon_2. \tag{194}$$

Equivalently,

$$\dot{\varepsilon} = \dot{\varepsilon_1} + \dot{\varepsilon_2} \tag{195}$$

and upon substitution on obtains the Maxwell relation between stress and strain rate (Equation (196)).

MAXWELL MODEL OF VISCOELASTICITY

$$\sigma + \frac{\eta}{E}\dot{\sigma} = \eta\dot{\varepsilon}. \tag{196}$$

Figure 66 shows the response to an increase in stress that is held for some time before being reduced back to zero for a dashpot and for a spring individually. Figure 67 shows the corresponding response of a Maxwell viscoelastic material. These are called creep-recovery responses.

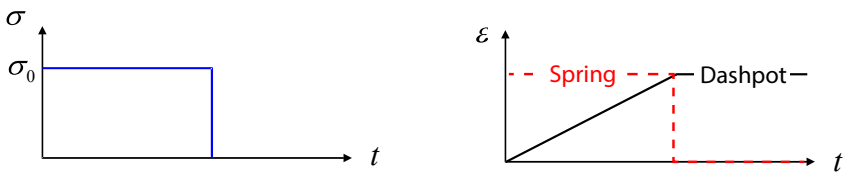

Figure 66

Response of a dashpot (black) and spring (red) to an applied stress.

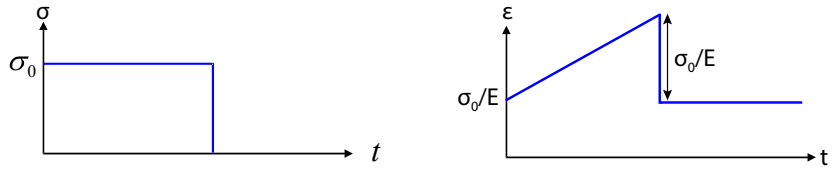

Figure 67

Response of a Maxwell material.

9.4.2. Glass Transition.

CHANGE IN THERMODYNAMIC PROPERTIES AT GLASS TRANSITION

At the glass transition an *amorphous material*, that is a glass, exhibits a more or less sudden change in thermodynamic properties from liquid-like to crystal-like, such as heat capacity (Figure 68) and thermal expansivity, over a relatively small change in temperature [Wong and Angell 1976].

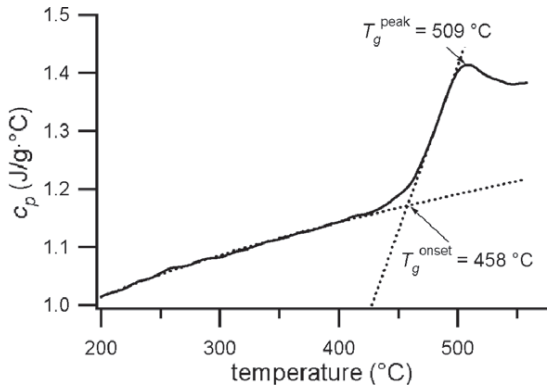

Figure 68

Figure 1 of Giordano et al. [2005]. Variation of specific heat capacity (c_p) with temperature across the glass transition for a phonolite from Teide volcano, Tenerife.

The viscous (liquid) response of silicate melts is termed *relaxed*, that is it behaves as a liquid, because the relaxation time of the melt structure to the equilibrium configurational state occurs at a shorter time than the imposed frequency or rate of deformation. However, behavior that characterizes the glass transition may also be observed at constant temperature if the imposed frequency (rate) of deformation exceeds the relaxation rate of the melt structure (Figure 69). Beyond the glass transition the response of the melt is termed *unrelaxed*, that is it behaves elastically like a glass.

"The crossing of the glass transition with cooling results from the exponential decrease with temperature of the self-diffusivity of Si and other components in the liquid [Dingwell and Webb 1989]. The effective freezing out of the self-diffusion in this manner affects the kinetics of a host of processes (e.g., viscous flow, growth and nucleation of crystals and bubbles). Although crystallization has been avoided, the liquid is effectively *frozen* to a glass [Giordano et al. 2005]." Using *differential scanning calorimetry* on various natural silicate melts (trachyte, phonolite, basalt) with variable dissolved water content, Giordano et al. [2005] found that the glass transition temperature, T_g, depends on composition and is strongly reduced by increasing water content, particularly for the first 1 wt.% of water added. However, the onset of the glass transition interval was found to correspond for all samples, regardless of water content, to a viscosity of about 10^{12} Pa s, with the calirometric peak at about 10^{11} Pa s. Although the glass transition "temperature" is not a constant, practical considerations in glass making have led to the frequent use of a single glass transition temperature, usually defined as the temperature at which the viscosity is 10^{12} Pa s [Giordano et al. 2005].

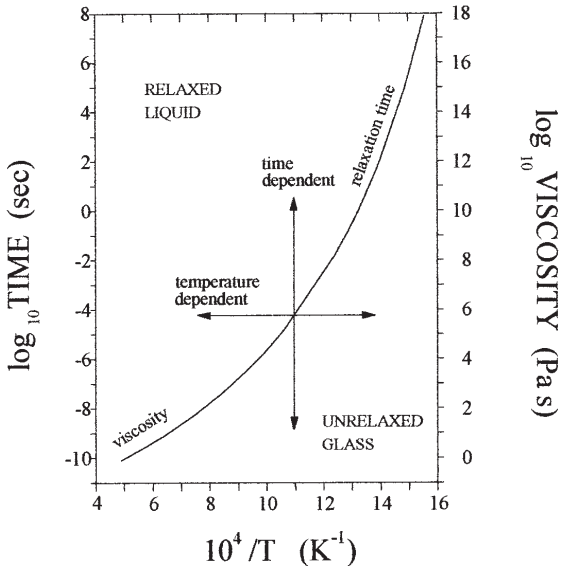

Figure 69

Figure 5 of Webb [1997]. The relaxation time curve and viscosity curve for $Na_2Si_2O_5$ as a function of inverse temperature calculated from the Maxwell relationship. The relaxation time curve can be crossed at a constant temperature by varying the timescale of observation of the melt property. If the timescale of observation is held constant, the relaxation time curve can be crossed by varying the temperature of the melt.

RELAXATION TIMESCALE

The relaxation timescale, τ_r, defines the glass transition curve and can be calculated as the ratio of Newtonian viscosity to infinite frequency elastic modulus, G_∞

$$\tau_r = \frac{\eta}{G_\infty}, \tag{197}$$

where G_∞ is commonly assumed to be $\sim 10^{10}$ Pa.

9.5. The effect of bubbles on rheology

The viscosity of magma containing bubbles also differs from that of the melt phase and depends on whether the bubbles are able to deform, which is governed by the relative importance of viscous stresses that act to deform bubbles relative to capillary stresses that act to keep bubbles spherical. The ratio of these forces is the Capillary number

$$\mathrm{Ca} = \eta_{\mathrm{melt}} \dot{\gamma} R / \sigma_{\mathrm{s}}, \tag{198}$$

where σ_{s} is surface tension. If Ca is small, $< O(1)$, bubbles are spherical and the magma viscosity is greater than that of the melt (e.g., Taylor, 1932). For Ca > 1, bubbles become elongated [Rust et al. 2003] (Figure 71 and the viscosity decreases [e.g., Bagdassarov and Dingwell 1992, Stein and Spera 2002, Rust and Manga 2002, Llewellin and Manga 2005].

A comprehensive formulation that explicitly accounts for the full range of Ca and is an extension of previous models for dilute suspensions is provided by Pal [Pal 2003]

$$\eta_r \left(\frac{1 - 12\eta_r^2 \mathrm{Ca}^2/5}{1 - 12\mathrm{Ca}^2/5} \right)^{-4/5} = \left(1 - \frac{\phi}{\phi^*} \right)^{-\phi^*}, \tag{199}$$

whereas a recent review of the subject is given in Mader et al. [2013].

The effect of bubbles on the flow of magma is illustrated in Figure 73. For a given frictional pressure loss and assuming laminar flow, the presence of bubbles can increase or decrease mass discharge rate by almost one order of magnitude, depending on Ca. The strain-rate dependent rheology of silicate melt with suspended bubbles and crystals derives from a superposition of the individual dependencies [Brückner and Deubener 1997, Thies 2002].

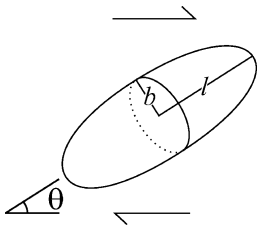

Figure 70

Figure 1 of Rust and Manga [2002] illustrating the shape and orientation of a deformed bubble in a simple shear flow of Ca> 1.

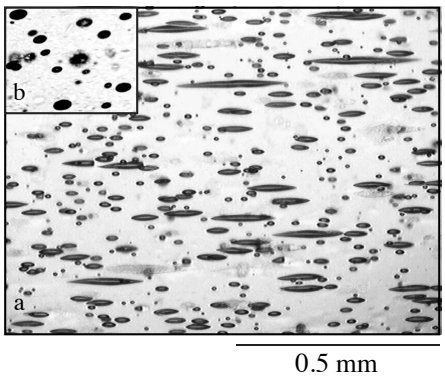

Figure 71

Figure 3 of Rust et al. [2003] illustrating photomicrographs of the Mayor Island sample perpendicular to flow banding, (a) parallel to the bubble elongation lineation, and (b) perpendicular to the bubble lineation.

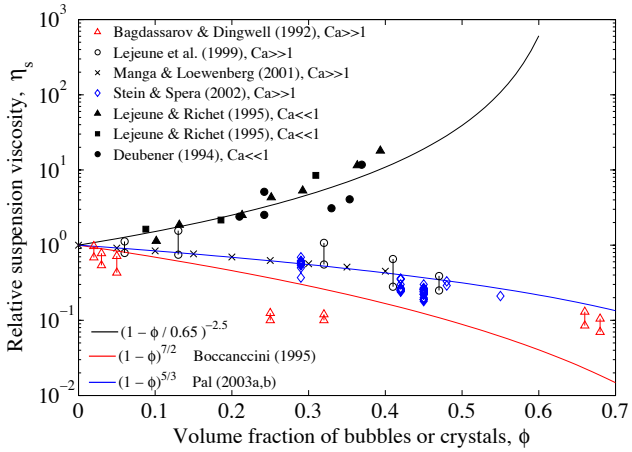

Figure 72

Figure 6 of Gonnermann and Manga, Annu. Rev. Fluid Mech. (2007). Relative viscosity of suspensions of silicate melt + bubbles (open triangles, circles, and diamonds) and silicate melt + crystals (black solid dots, triangles, and squares). Only cases with Ca$\ll$ 1 and Ca$\gg$ 1 are shown. Crosses are numerical calculations for bubbles in liquid (Manga & Loewenberg 2001). Note that at values of above approximately 0.4 the rheological behavior for melt and crystals becomes complex and inhomogeneous, including yield strength and shear localization (see Lejeune & Richet 1995 for a discussion). Measurements are published in Bagdassarov & Dingwell (1992), Deubener (1994), Lejeune et al. (1999), Lejeune & Richet (1995), Manga & Loewenberg (2001), and Stein & Spera (2002).

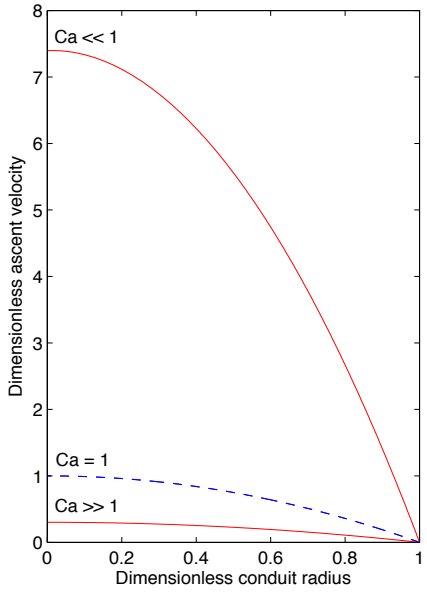

Figure 73

The effect of bubbles on magma viscosity, where $\phi = 0.6$ and $\phi^* = 0.75$. For each velocity profile the pressure gradient and melt viscosity were identical.

9.6. The effect of crystals on rheology

KEY POINTS

- Relative viscosity, η_r, is the measured viscosity of the suspension normalized by the (Newtonian) liquid viscosity.
- The maximum packing fraction of particles, ϕ_m, is the volume fraction of particles required to fill a container.
- Jamming occurs at some value of ϕ, which corresponds to particles forming interconnected networks that effectively 'hinders' the motion of particles past one another.
- Einstein (1906) proposed an equation for η_r as a function of particle volume fraction, ϕ

$$\eta_r = 1 + B\phi, \tag{200}$$

  where B is a constant with a value of 2.5 in the case of spheres.
- For both dilute and concentrated suspensions Krieger (1959) proposed

$$\eta_r = \left(1 - \frac{\phi}{\phi_m}\right)^{-B\phi_m}, \tag{201}$$

  where ϕ_m is the maximum packing fraction of particles.
- Herschel (1926) proposed a model that accounts for both apparent yield stress, τ_y and strain-rate dependence

$$\tau = \tau_y + K\dot{\gamma}^n, \tag{202}$$

  where K is the *consistency* and n is the flow index.

Crystals increase magma viscosity compared with that of the melt [Lejeune and Richet 1995, Brückner and Deubener 1997, Caricchi et al. 2007, Lavallee et al. 2007]. At crystal volume fractions of $> 30\%$, the suspension viscosity will increase by several orders of magnitude over the melt viscosity Lejeune and Richet [1995], Brückner and Deubener [1997], Caricchi et al. [2007], Lavallee et al. [2007]. This, of course, tremendously affects magma ascent, perhaps to the point of inhibiting it, because of the very large frictional pressure loss. Depending on the shape of the crystals, a framework of interconnected and touching crystals provides an apparent yield strength to the magma [e.g., Barnes 1999, Saar et al. 2001]. Shear thinning behavior is caused by the redistribution of melt and crystals to produce smaller flow disturbance relative to the disordered suspension [e.g., Caricchi et al. 2007]. At greater than about 60 vol % of crystals, inter-particle contact requires dilation, as well as brittle deformation of crystals, to allow particles to move relative to one another during flow [e.g., Rutter et al. 2006, Lavallee et al. 2007, Caricchi et al. 2007]. It is likely that the ascent of magmas with significant amounts of crystals will be subjected to shear localization and formation of shear zones [Lejeune and Richet 1995, Lavallee et al. 2007, Caricchi et al. 2007, Arbaret et al. 2007]. The subsequent sections provide an overview of concepts and rheological models related to suspension viscosity. Parts of this discussion are copied verbatim from a paper by (Moitra & Gonnermann, G3, 2015, doi:10.1002/2014GC005554).

9.6.1. Relative viscosity. At any instant, the ratio of shear stress to shear rate defines the shear viscosity of a fluid. The viscosity of a fluid usually increases if particles are added in suspension. This change in viscosity is expressed as the ratio of the viscosity of the suspension (liquid+particle) η_s, to the viscosity of liquid η_l, and is called the relative viscosity η_r. Because of the complicated theory behind multi-body particle-particle-liquid interactions, the notion of suspension viscosity, which is based on a continuum approximation, has been proven useful for a wide range of applications.

The relationship between an applied stress and resultant deformation rate is a manifestation of the aforementioned interactions, and it is the principal macroscopically accessible observation amenable to quantitative measurement. It is therefore of fundamental importance for any field of study involving liquid-particle suspensions. The estimation of suspension viscosity is based on well-established methodologies that yield reproducible direct measurements of shear stress and shear rate using sophisticated rheometers [e.g., **?**]. Measuring the viscosity of suspensions is also complicated because the relationship between shear

stress and shear rate may depend on the shear rate, $\dot{\gamma}$, and also on strain, γ. Therefore, the measured viscosity at any given shear rate and strain is called the apparent viscosity.

A number of models have been proposed to estimate the rheological properties of unimodal particule suspensions (Table **??**). In the pioneering work by Einstein (1906), η_r has been expressed as a function of particle volume fraction, ϕ, given by

$$\eta_r = 1 + B\phi, \tag{203}$$

where B is a constant with a value of 2.5 in the case of spheres. The Einstein model is limited to suspensions with $\phi \leq 0.10$. A widely used semi-empirical model for both dilute and concentrated suspensions was proposed by Krieger (1959) and is given by

$$\eta_r = \left(1 - \frac{\phi}{\phi_m}\right)^{-B\phi_m}, \tag{204}$$

where ϕ_m is the maximum packing fraction of particles.

Among the models for bimodal to polymodal suspensions, the model by **?** is based on effective medium theory, where the coarser particles are considered to be suspended in a material with properties equivalent to a mixture of finer particles and suspending liquid.

9.6.2. Herschel-Bulkley model. The aforementioned models predict suspension viscosity as a function of particle volume fraction, ϕ, but neglect shear-rate dependence or yield stress. Although, the existence and meaning of yield stress have been an issue of debate, measurements of shear stress, τ, as a function of $\dot{\gamma}$, indicate that suspensions above some critical volume fraction of particles and at low values of $\dot{\gamma}$ undergo a rheological transition that has been attributed to a change from liquid- to solid-like behavior. This transition can be characterized within rheological models as an apparent yield stress parameter, τ_y. A model that accounts for both apparent yield stress and strain-rate dependence is by Herschel (1926)

$$\tau = \tau_y + K\dot{\gamma}^n. \tag{205}$$

Here the relationship between τ and $\dot{\gamma}$ depends on three parameters: (1) the yield stress parameter, τ_y; (2) the consistency, K; and (3) the flow index, n. For a Newtonian liquid $\tau_y = 0$ and $n = 1$, in which case K is equal to the suspension viscosity η_s. In theory, once $\tau > \tau_y$ the suspension starts to deform. In experiments the measurement of yield stress is often confounded by limitations of accurately measuring sufficiently small values of $\dot{\gamma}$.

The flow index n defines the extent of shear-rate dependence, where the slope $d\tau/d\dot{\gamma}$ becomes less steep as n decreases. In other words, smaller values of n indicate a greater dependence of apparent viscosity on shear rate. To achieve a wide range of applicability for Equation (205) we seek for each of these three parameters functional dependences on particle shape, particle size, total volume fraction of particles and relative proportions of particles with different shape and/or size.

9.6.3. Maximum packing fraction. It has been found that the maximum packing fraction of the particle mixture, ϕ_m, is a key parameter in controlling the rheological response of suspensions [e.g., Mader et al. 2013]. At volume fractions below ϕ_m the deformation of the suspension involves the flow of liquid in-between particles, which themselves tend to be non-stationary. With increasing volume fraction, ϕ, the average inter-particle distance decreases, resulting in larger gradients in interstitial liquid velocity and higher viscosity of the bulk suspension. ϕ_m depends on the distribution of particle sizes and shapes (Figures 74 and 75), as well as the packing geometry. For example, for spheres in cubic or in random close packing $\phi_m \approx 0.52$ or 0.74, respectively; and for random close packing of ellipsoids $\phi_m \approx 0.74$ for aspect ratio ≈ 1.3.

MAXIMUM PACKING FRACTION

The maximum packing fraction, ϕ_m, is the volume fraction of particles required to fill a container. It can be viewed as the critical concentration of particles at which the suspension becomes *jammed* [e.g., **??**]. The latter refers to a physical state where an interconnected network of particles renders the suspension non-deformable so that viscosity tends to infinity.

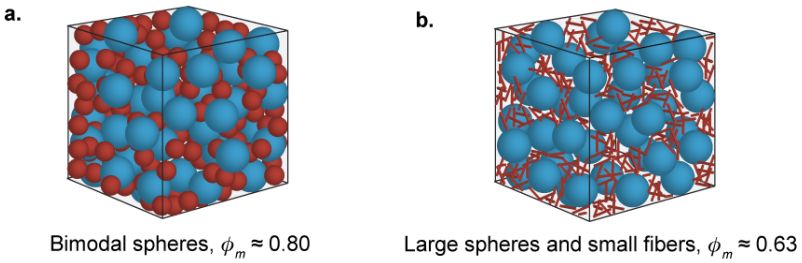

Figure 74

Diagrams illustrating the effect of particle aspect ratio, a_r and size ratio, λ on maximum dry packing fraction, ϕ_m. In comparison to the bimodal spherical particles **(a)**, high aspect ratio particles, due to entanglement and local caging **(b)**, create more excluded volume (open void space in between adjacent particles). From Moitra & Gonnermann (2015).

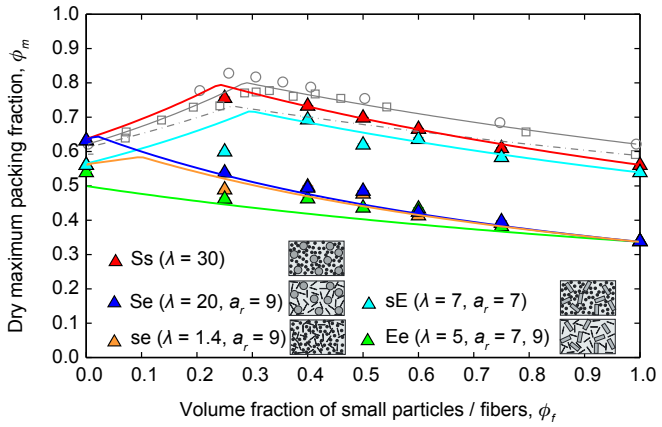

Figure 75

Dry maximum packing fraction of the different particle mixtures. The lines are based on the model of **?**, assuming an equivalent spherical diameter for fibers. λ is the ratio of particle diameters, approximated by the equivalent spherical diameter for fibers, whereas a_r is the aspect ratio of elongated particles. Open symbols are the data by **?** for bimodal spheres and by **?** for mixture of spheres and fibers. A value of $\phi_f = 0$ corresponds to a unimodal mixture of large or spherical particles ('S' or 's' or 'E'), whereas $\phi_f = 1$ represents a unimodal mixture of small or fibrous particles ('s' or 'e' or 'E'). Error bars are smaller than the symbol size. From Moitra & Gonnermann (2015).

9.7. Consistency, K

Consistency, K, is equal to η_s at $n = 1$, whereas the normalized consistency K_r is defined as K/η_l. For $\phi_f = 0.25$ we find that K_r always increases with ϕ following a Maron-Pierce type model

$$K_r = \left(1 - \frac{\phi}{\phi_m}\right)^{-\alpha}, \tag{206}$$

where α is a fitting parameter, and Moitra & Gonnermann (2015) find $1.7 < \alpha < 3.2$, with typical values of $\alpha \approx 1.9$. That ϕ_m is the key parameter controlling K_r is apparent when K_r is plotted as a function of ϕ/ϕ_m, with K_r tending to infinity as $\phi \to \phi_m$. At a given ϕ, values of K_r are larger for suspensions with particles of higher aspect ratios and/or for smaller particle size ratios.

9.7.1. Flow index, n. The flow index determines the dependence of viscosity on shear rate. Our results show a decrease in viscosity with increasing shear rate (i.e., $n < 1$) for all suspension types and at any given ϕ. All else being the same, n decreases with increasing ϕ for a given suspension type. Furthermore, across different suspension types, at a given ϕ, the values of n are smaller for suspensions with particles of larger aspect ration and/or with smaller size ratio. Moitra & Gonnermann (2015) find $0.4 \leq n \leq 1$.

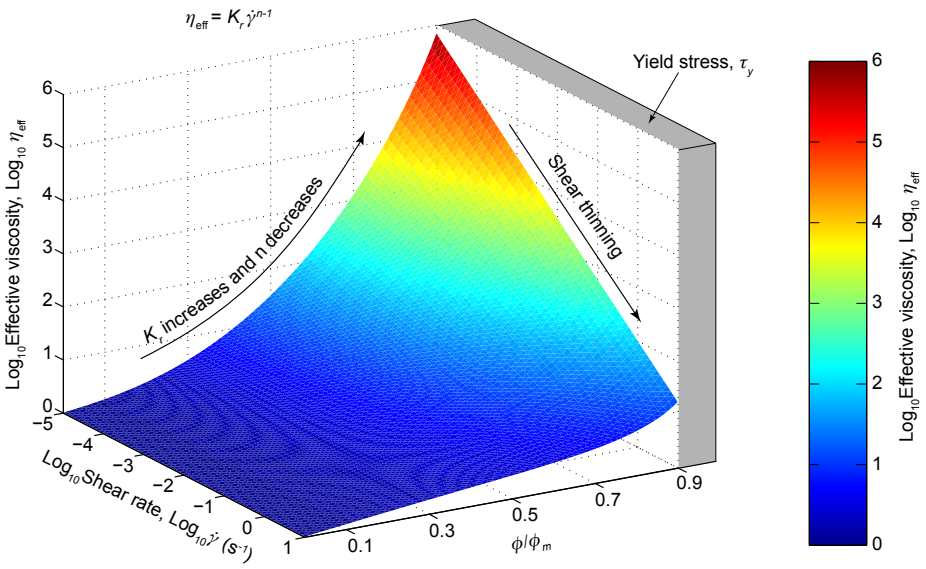

Figure 76

Effective viscosity, η_{eff}, as a function of shear rate, $\dot{\gamma}$, and normalized particle volume fraction, ϕ/ϕ_m, with K_r and n dependent on ϕ/ϕ_{m}. For $\phi \to \phi_m$ yield stress, τ_y, is significant and η_{eff} is not valid. From Moitra & Gonnermann (2015).

9.8. Yield stress and effective viscosity

The dependence of η_r on $\dot{\gamma}$ is significant for $\phi/\phi_m > 0.5$, leading to as much as a $10 - 100$ fold decrease in η_r across $2 - 3$ orders of magnitude change in $\dot{\gamma}$. The physical origin of such shear thinning behavior remains controversial. An important aspect of Equation (206) is the prediction of an infinite viscosity as $\phi \to \phi_m$, consistent with the view that at some value of ϕ, particles form interconnected networks that effectively 'hinder' the motion of particles past one another, in a process referred to as *jamming*. Because yield stress becomes only significant as $\phi \to \phi_m$, an effective relative viscosity, η_{eff}, can be defined from the Herschel-Bulkley model with applicability over a wide range of conditions

$$\frac{\eta_s}{\eta_l} \approx \eta_{\text{eff}} = K_r \dot{\gamma}^{n-1}, \tag{207}$$

where K_r and n depend on ϕ/ϕ_m. Figure 76 shows the variation in η_{eff} as a function of $\dot{\gamma}$ and ϕ/ϕ_m. $\eta_{\text{eff}} \to 1$ as $\phi \to 0$, however, because of the approximation $\tau_y = 0$, Equation (207) is not applicable as $\phi \to \phi_m$, where τ_y becomes significant.

9.9. Viscous dissipation (shear heating)

For a control volume the first law of thermodynamics requires that:

the rate of energy accumulation =
the net transfer of energy by fluid flow
+ the net heat transfer by condutcion
+ the rate of internal heat generation
- the net work transfer from the control volume to its environment

We will jump directly to the "temperature" formulation of the First Law of Thermodynamics (but see the notes on *Conservation Equations* for more details)

$$\rho c_p \frac{DT}{Dt} = \nabla \cdot (k \nabla T) + q_{\text{internal}} + \beta T \frac{DP}{Dt} + \mu \Phi, \tag{208}$$

where β is the coefficient of thermal expansion and Φ is the viscous dissipaton function (i.e., frictional heating), which in the case of incompressible and two-dimensional flow reduces to

$$\Phi = 2\left[\left(\frac{\partial u}{\partial x}\right)^2 + \left(\frac{\partial v}{\partial y}\right)^2\right] + \left(\frac{\partial u}{\partial y} + \frac{\partial v}{\partial x}\right)^2. \tag{209}$$

The implications are as follows. Recall that near the conduit walls shear rates are highest. This is therefore where there will be the highest amount of heat generation due to viscous dissipation. Because shear heating will lower viscosity, this can result in localization of shear deformation or, in other words, a positive feedback between shear heating and shear localization near the conduit walls.

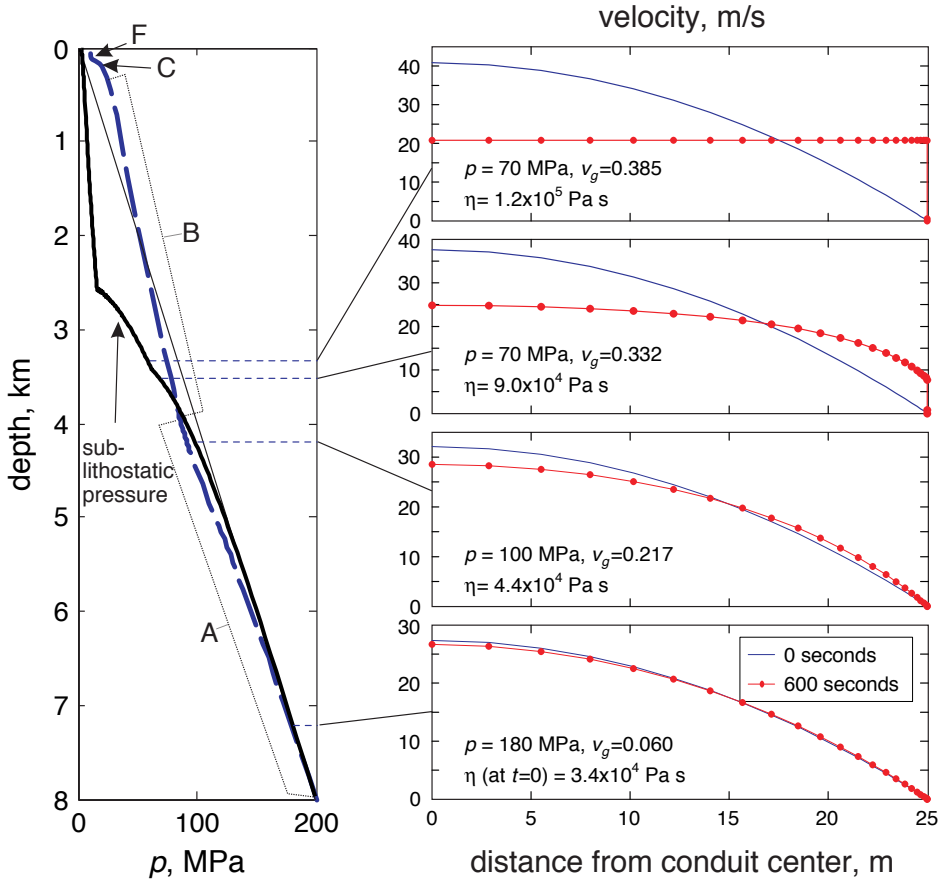

Figure 77

Figure 4 or Mastin [2005]. **Left:** Pressure profile (heavy solid line) compared with a run (dashed line) for which the conduit friction factor was adjusted for shear heating. The light solid line represents the lithostat for a rock density of 2500 kg m^{-3}. **Right:** Velocity profiles under isothermal initial conditions (solid lines) and after 10 min of viscous heating (red with dots). Arrows indicate the depth at which these pressures would occur in the conduit under isothermal flow. Variable v_g denotes the gas volume fraction. Note the extreme departure from a parabolic velocity profile after a short time. For this calculation the radial temperature profile was calculated at each depth from the transient energy equation. In contrast, for the conduit flow a steady-state velocity profile with radially varying viscosity is assumed.

10. Magma fragmentation

SOME DEFINITIONS

- Brittle: Material response above a critical stress by fracture and loss of continuity (cohesion).
- Ductile: Response of a solid material to tensile stress by flowing mesoscopically like a viscous fluid with strain distributed throughout.
- Elasticity: The ability of a body to return to its initial shape and size after a deforming stress is removed.
- Maxwell time: The time after which a stressed viscoelastic material transitions from elastic to viscous deformation.
- Plasticity: The capacity of a material to undergo non-reversible deformation above a sufficient applied stress, called yield.
- Viscoelasticity: Capacity of materials to undergo recoverable elastic deformation at short times and viscously at long times.
- Viscous: Non-reversible deformation of a fluid to an applied stress. Newtonian if stress and strain rate are linearly related.

Magma fragmentation may occur at some depth beneath the surface, usually within the volcanic conduit and/or above the surface. As the pyroclasts are transported to, at, or above the surface, collisions between clasts result in additional fragmentation, termed *secondary fragmentation*. Upon deposition pyroclastic material may form unconsolidated tephra deposits or become welded to form pyroclastic rock. In some cases welded pyroclastic deposits may be able to flow for some distance in a process termed rheomorphic flow. In eruptions of low-viscosity basaltic magmas, fragmentation will produce pyroclastic material that remains fluid and can, upon deposition, form lava flows and lava lakes.

Brittle magma fragmentation requires that the melt, a viscoelastic material, responds to an applied stress in a predominantly elastic manner. This is the case for highly polymerized melts, if they are subjected to a sufficiently large stress. The glass transition defines the conditions of temperature and deformation rate under which the deformation of silicate melt changes from viscous to elastic, with recoverable elastic deformation at small strains and brittle failure at large strains.

If silicate melts are subjected to sufficiently large stress over a short duration, deformation may be mostly accommodated by reversible changes in molecular bond lengths and angles. In other words, by elastic deformation at small strain. In fact, over some range of stress the melt behaves approximately as a linear viscoelastic material. At sufficiently high stress and large strain deformation causes bonds within the silicate network to break, resulting in a decrease in apparent viscosity. This non-Newtonian behavior is known as shear thinning. Upon sufficiently long application of such high stress the melt structure will be disrupted, due to its inability to relax on the time-scale of the deformation, resulting in brittle failure.

The relaxation time-scale can be estimated from the Maxwell relation $\tau_r = \eta_r/G$, where η_r is the melt viscosity at low strain rates and $G \sim 10^{10}$ Pa is the shear modulus [Dingwell and Webb 1989, **?**, Dingwell 1997]. It is found that shear-thinning behavior occurs at about 3 ± 0.5 orders of magnitude lower strain rates than the relaxation rate τ_r^{-1}, whereas the transition to viscoelastic behavior occurs at strain rates of approximately 2 orders of magnitude below τ_r^{-1}. This transition between viscous or ductile and elastic or brittle behavior is the glass transition [Figure 78; Dingwell 1996]. Once the magma intersects the glass transition, fragmentation can be treated within the conceptual framework of fracture mechanics. In other words, at or beyond the glass transition high strain and strain rates prevent structural relaxation and the molecular structure of the magma is disrupted, resulting at the macroscopic scale in brittle fracturing. Numerical modeling suggests that magma expansion during eruption, due to volatile exsolution and decompression, can result in sufficiently large extensional strain rates to intersect the glass transition [Papale 1999].

10.1. Fragmentation and the ascent of magma with high viscosity

The pressure of ascending magma must decrease, mostly because of the static pressure of the overlying magma and the pressure loss required to balance viscous stresses, referred to as wall friction [Wilson 1999]. In the simplest sense, for magma to erupt at steady conditions, the pressure within the chamber has to

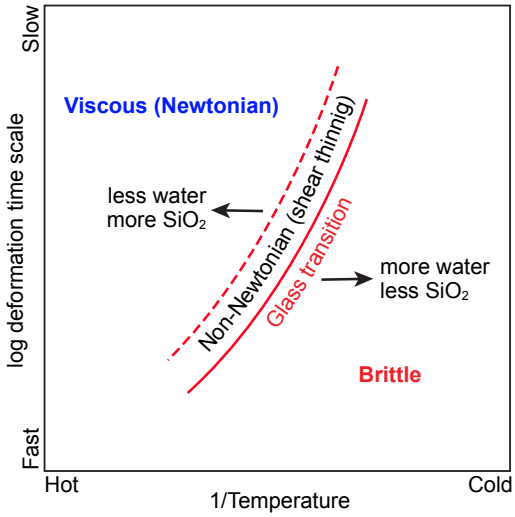

Figure 78

Schematic diagram of the glass transition in time vs. reciprocal temperature space [Dingwell 1996]. Melt composition, temperature and dissolved water content determine viscosity and, hence, the structural relaxation time. The melt deforms as a Newtonian viscous liquid if deformation rates are slower than $\sim 10^{-3.5} G/\eta_r$. At deformation rates $\gtrsim 10^{-2} G/\eta_r$ the flow becomes nonNewtonian and the response will be elastic at small strain and brittle failure at high strain.

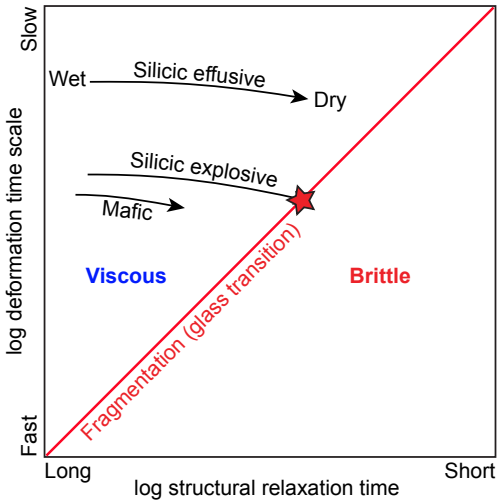

Figure 79

Schematic diagram illustrating idealized hypothetical ascent paths for silicic and mafic magmas. During ascent magma degasses, which increases viscosity and decreases the structural relaxation time. Although deformation rates may not change by much, the magma approaches the glass transition and brittle fragmentation, as it loses water. If the magma ascends slowly, it may never intersect the glass transition, because deformation rates are too slow. In contrast, even rapidly ascending mafic magma will not intersect the glass transition, because its structural relaxation time remains too large.

balance or exceed the integrated pressure loss within the conduit [e.g., Wilson et al. 1980, Mastin 2002]

$$p_c - p_v = \int_c^v \left[\rho u \frac{g}{u} + \rho u \, f \frac{u}{a} - \rho u \frac{u}{a^2} \frac{da^2}{dz} + \rho u \frac{1}{\rho} \frac{d\rho}{dz} \right] dz. \tag{210}$$

Here subscripts c and v denote chamber and vent, respectively. Furthermore, the conduit radius, a, the ascent velocity, u, and the magma density, ρ, are all functions of the vertical coordinate z. The first term on the right hand side of Equation ((210)) is the hydrostatic or rather, magma-static pressure loss, whereas

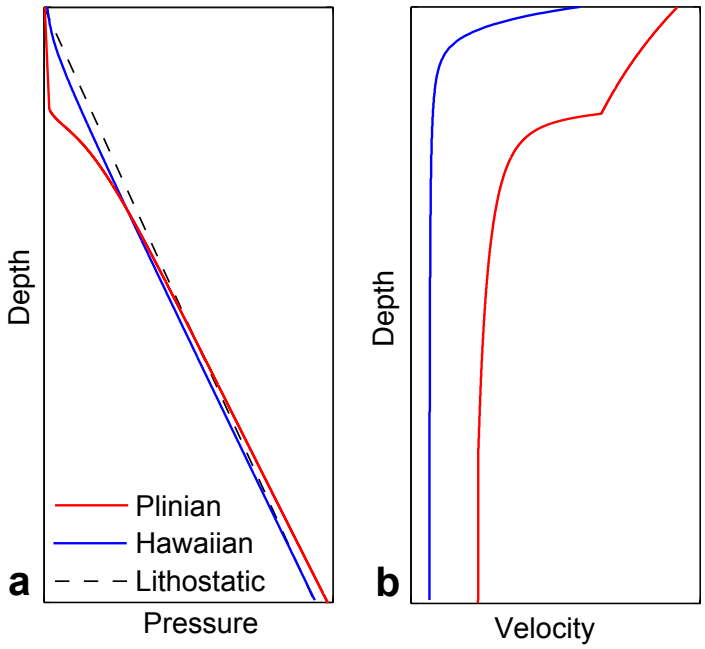

Figure 80

Illustrative examples of (a) magma pressure, (b) magma velocity, both as a function of depth for the Hawaiian style eruption of basaltic magma (blue) and for the Plinian eruption of rhyolitic magma (red). For the basaltic magma pressure is close to lithostatic, because frictional pressure loss is much smaller than the magma-static pressure gradient. For the rhyolitic magma frictional pressure loss becomes much larger than magma-static, once appreciable amounts of water exsolve. Without fragmentation and resultant low-viscosity gas-pyroclast mixture, the eruption of highly viscous magma at high velocities would not be possible.

the second term is the frictional pressure loss, with $f \approx f_0 + 8\eta/\rho u a$ and $f_0 \sim 0.001 - 0.01$. It should be noted that near the conduit walls, heating by viscous dissipation [e.g., Mastin 2005], shear thinning due to the presence of bubbles or crystals [**?**], as well as shear fragmentation [Goto 1999, Gonnermann and Manga 2003], each have the potential to affect f. The third and fourth terms are due to magma acceleration, which in the case of a constant discharge rate may arise from changes in conduit radius, as well as volatile exsolution and expansion, which decrease magma density.

Assuming the conduit radius does not change drastically with depth, the pressure loss due to friction and acceleration is small, relative to magma-static pressure, especially if u is small. Moreover, magma-static pressure tends to be smaller than lithostatic pressure, because magma density decreases as a consequence of volatile exsolution. Therefore, values of p_c, which may exceed lithostatic pressure by up to approximately 10 MPa, can result in the slow eruption of high-viscosity magma. As u increases, the frictional pressure loss, especially as the magma becomes more viscous due to water exsolution, can become so large that reasonable values of p_c are insufficient to drive the magma to the surface, unless the magma fragments at some depth z_f. In this case the gases are released from confining bubbles and expand. The resultant decrease in the gas-pyroclast mixture not only reduces the magma-static pressure, but the low viscosity of the mixture also drastically reduces the frictional pressure loss above z_f [Figure 80; Dobran 1992, Mader 1998, Papale 2001, Dufek and Bergantz 2005, Koyaguchi 2005]. Fragmentation of high viscosity magma may thus not only require rapid magma ascent rates, but it may also be a necessary condition for high viscosity magma to erupt at high discharge rates.

10.2. Fragmentation by Bubble Overpressure

Brittle fragmentation in bubbly viscoelastic fluids that are undergoing abrupt decompression has been observed experimentally [Ichihara et al. 2002, Namiki and Manga 2005]. Brittle fragmentation of vesicular magma has been reproduced experimentally by confining and heating porous volcanic rock samples within a pressurized *shock tube* and then decompressing them near-instantaneously by rupturing a diaphragm at one end of the shock tube [Alidibirov and Dingwell 1996, Spieler et al. 2004]. A decompression wave

propagates into the sample and it fragments, if the change in pressure exceeds a threshold of approximately σ_t/ϕ, where $\sigma_t \approx 10^6$ Pa is the tensile strength of the melt and ϕ is the volume fraction of vesicles (Figure 81).

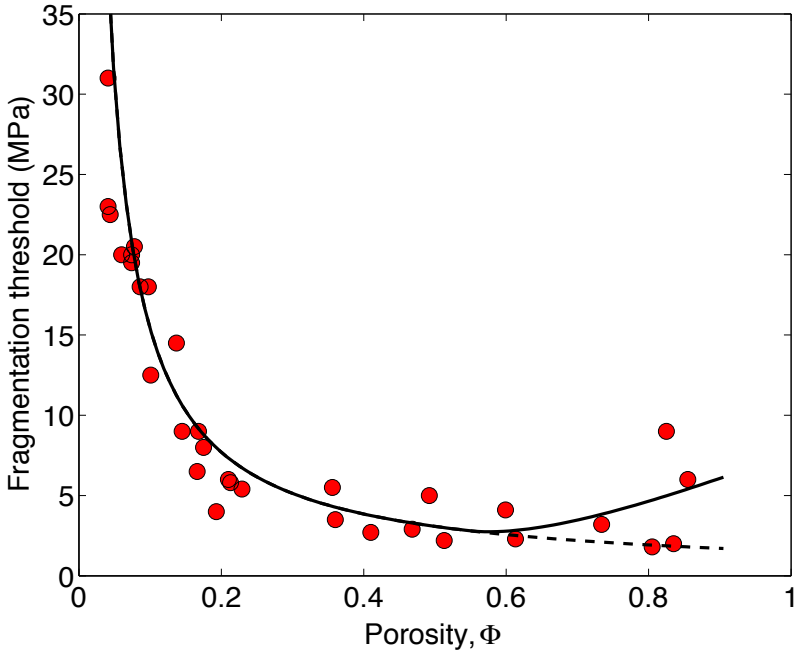

Figure 81

Pressure drop as a function of sample porosity, ϕ, at which porous volcanic rocks samples of various compositions and a temperature of 850°C fragmented upon abrupt decompression [Spieler et al. 2004]. Also show is the empirical threshold of σ_t/ϕ (dashed curve), where $\sigma_t = 1.54 \times 10^6$ Pa, as well as the empirical threshold that accounts for pressure dissipation by permeable gas flow (solid curve) given by $(8.21 \times 10^{11}\,\mathrm{Pa\,m^{-1}}\sqrt{k} + \sigma_t)/\phi$ [Mueller et al. 2008], where permeability is based on measured values in silicic Plinian pyroclasts and is given by $k = 9 \times 10^{-10}$ m^2 $(\phi - \phi_c)^n$, with a percolation threshold of $\phi_c = 0.55$ and $n = 3.5$ [**?**].

This dependence of the fragmentation threshold on ϕ derives from the geometrical relationships of stress distribution within the melt surrounding bubbles [e.g., Zhang 1999, Koyaguchi and Mitani 2005]. The value of σ_t has also been estimated from fiber elongation studies, and values of $\sim 10^8$ Pa are considerably higher than those obtained from shock tube experiments. A possible explanation for this discrepancy is the presence of micro-cracks within bubble walls. As water diffuses from the melt into bubbles, the resultant concentration gradients result in viscosity gradients and volume stresses, due to the dependence of molar melt volume on dissolved water content. Because samples used in shock tube experiments were cooled and solidified prior to reheating and decompression, they presumably contained such micro-cracks. In contrast, the formation of micro-cracks in erupting magmas is contingent on the development of volume stresses that locally exceed the tensile strength of the melt on time scales that are shorter than the relaxation time. Stress localization at the tips of such micro-cracks, if they indeed exist, should then decrease the effective tensile strength of erupting magmas to $\sigma_t \sim 10^6$ Pa [Alidibirov 1994, Zhang 1999, Spieler et al. 2004].

Fragmentation in shock tube experiments proceeds via the formation of brittle fractures that propagate layer by layer into the sample, producing fragments that range in size from tens of micron to centimeters. It is envisaged that magma fragments in this manner during sustained explosive eruptions, by ascending rapidly into a region of steep pressure gradients, which in turn are a consequence of acceleration due to bubble nucleation and growth, as well as large increases in viscosity. Consequently, frictional pressure losses increase simultaneously as the melt relaxation rate decreases. The magma thus rises monotonically toward conditions that favor brittle fragmentation (Figure 80). In other words, ϕ, η and u all increase, driving the magma toward $\eta\, u/a \gg \sigma_t/\phi$, which is equivalent to a Deborah number criterion, $\tau_r \gg \tau_p$, for brittle fragmentation. In contrast, during unloading events and Vulcanian eruptions the decompression wave propagates downward into a relatively stagnant and degassed magma of high viscosity, but also with $\tau_\eta \gg \tau_p$ and $\tau_r \gg \tau_p$.

10.3. Fluid-dynamic breakup

In volcanic eruptions of low viscosity magmas, such as basalt, fragmentation is not by intersection of the glass transition, but rather by breakup in the liquid state through hydrodynamic stresses and instabilities. This is a common phenomenon of everyday life, such as for example, the breakup of a jet of water or the droplets generated from bursting bubbles. It involves a change in topology from a compact macroscopic volume into sheets and filaments. The latter then break apart into smaller fragments, either because of capillary instability to along-axis variations in thickness, or because of pinch-off when stretched to some critical thickness.

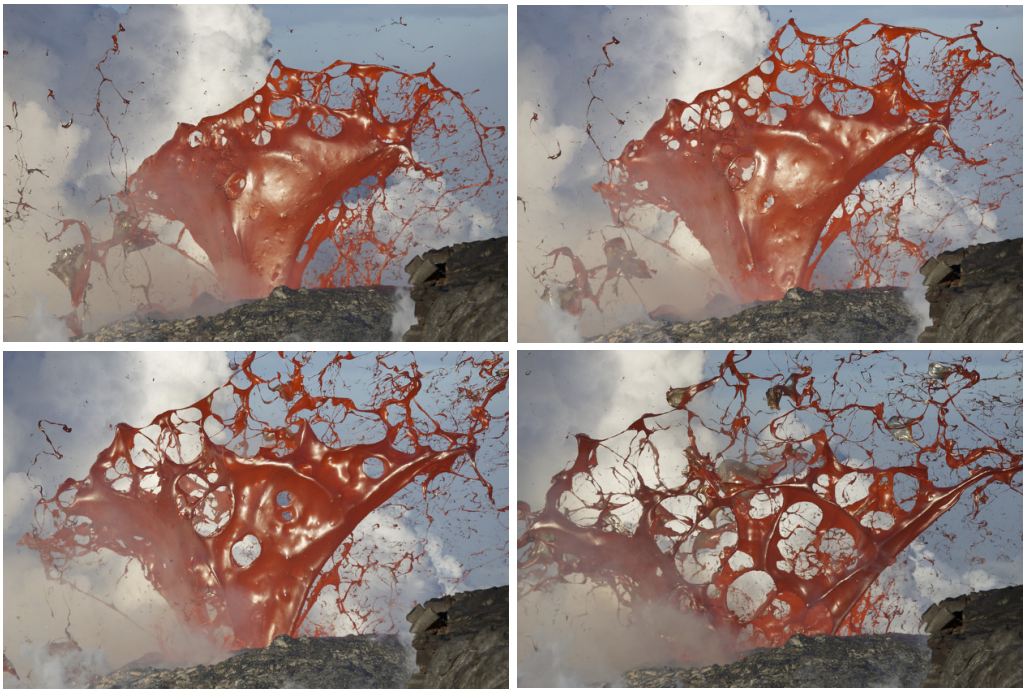

Figure 82

Fluid-dynamic breakup of basaltic magma by an expanding vapor bubble of approximately 30 m in diameter at Kilauea volcano, Hawaii. The time interval between individual frames is approximately 0.2 s. The magma becomes stretched into a sheet that breaks up into filaments, which in turn break up into pyroclasts (Photo: Bruce Omori/Extreme Exposure).

Capillary instabilities arise because the local pressure inside a liquid filament is greater than the pressure of the surrounding gas or air, by an amount that is inversely proportional to the local radius of curvature of the interface. Because the smallest radius of curvature corresponds to the thinnest part of the filament, there will be an axial pressure gradient causing flow from thinner to thicker parts. Once a segment reaches a thickness of the order of 1 μm, it pinches off and retracts to form a more compact volume with lower surface energy. Bubbles or particles can affect the breakup of liquid sheets and filaments significantly.

Filament formation, and ultimately breakup, can be dominated by capillary or viscous forces. The capillary dominated characteristic breakup time is $\tau_{\rm cap} \sim \sqrt{\rho d/\sigma}$, where d is the diameter. If viscous forces dominate, then breakup is slowed and the characteristic timescale is instead $\tau_{\rm vis} \sim \eta d/\sigma$. The ratio of these two timescales is the Ohnesorge number, ${\rm Oh} = \tau_{\rm vis}/\tau_{\rm cap}$. For magmas breakup is dominated by viscous forces, because ${\rm Oh} \gg 1$. If the filament is being stretched in the axial direction at an elongation rate of $\tau_{\rm str}^{-1}$, the instability is suppressed if $\tau_{\rm str} < \max[\tau_{\rm vis}, \tau_{\rm cap}]$, although it will still break up, once a critical thickness is reached.

In many situations, such as for example a liquid drop within a stream of air, the liquid will first deform into a flattened shape with a toroidal rim that contains most of the liquid volume. As the sheet becomes stretched it eventually ruptures and the filament-like rim becomes corrugated and breaks up into drops. These drops may themselves break up into smaller drops, in what can be considered a cascade of breakups. A key parameter associated with the resultant fragment (drop) size is the aerodynamic Weber number,

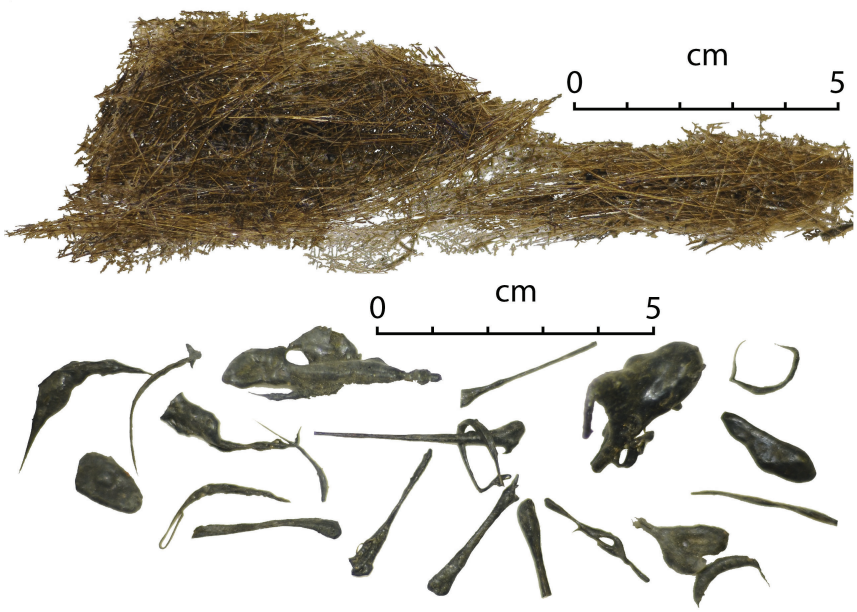

Figure 83

Pele's hair (top) and Pele's tears (bottom) from Kilauea volcano, Hawaii. (Bruce F. Houghton).

$\mathrm{We}_g \sim \rho_g(\Delta u)^2 l/\sigma$, where ρ_g represents the density of the surrounding gas, Δu is the difference in velocity between the surrounding gas and the drop, and l is the drop diameter. The Weber number represents the ratio of the stress due to drag between gas and liquid, that is $\rho_g(\Delta u)^2$, which is essentially a stagnation pressure that will deform the drop, and the capillary pressure, σ/l, which tends to restore the drop to spherical shape.

In turbulent jets, filaments and drops are also formed as a consequence of shear at the interface between the liquid and the surrounding air or gas. The dynamics of jet disintegration depend on a Reynolds number and a Weber number, which are each based on the liquid viscosity and on the relative velocity between liquid and gas. The fragmentation process becomes increasingly effective at disrupting the jet as inertial forces increase, relative to viscous and capillary forces, in other words, as Reynolds and Weber numbers increase. For magma it is reasonable to expect that the topology of the gas-melt mixture, due to the presence of bubbles, plays a significant role during deformation into filaments and subsequent breakup. This is illustrated in Figure 82, where sheet rupture is facilitated by the presence of bubbles.

10.3.1. Magma Jets: Hawaiian. For sustained explosive eruptions of low viscosity magma, such as Hawaiian style eruptions, the flow within the conduit will be turbulent. The magma-gas mixture will exit the vent at speeds of $\sqrt{2gH_f} \sim 10 - 100$ m s^{-1} [Wilson 1999], where H_f is the height to which the magma jets above the surface, and typically hundreds of meters in Hawaiian style eruptions. Rapid decompression of a bubbly Newtonian liquid, analogous to basalt magma, results in inertial stretching and break-up into discrete pieces, if $\mathrm{Re}_e = \rho u_e L/\eta \gtrsim 1$, where Re_e is the expansion Reynolds number, u_e is the expansion velocity, and L is the height of the expanding liquid volume. During Hawaiian style eruptions inertial fragmentation is expected to occur within the upper-most few hundred meters of the conduit and/or in the jet above the surface, where rapid exsolution and expansion of water vapor lead to high magma expansion rates. Numerical modeling predicts a difference in velocity between magma and free gas phase of $\Delta u \sim 100$ m s^{-1} [Wilson 1999], corresponding to $\mathrm{We} = \rho(\Delta u)^2 a/\sigma$ and $\mathrm{Re} = \rho a \Delta u/\eta$, where a is the jet radius. This implies that there should be magma breakup due to interfacial shear between gas and melt, which is corroborated by the abundant presence of Pele's hair during Hawaiian style eruptions.

10.3.2. Bursting Bubbles: Strombolian. Strombolian eruptions are characterized by the bursting of large gas slugs, which may form by coalescence of smaller bubbles during ascent or if the conduit geometry is somehow favorable to the accumulation of buoyantly rising bubbles. When a slug becomes sufficiently large to break free and rise to the surface, it expands in size as pressure decreases. Near the surface the

overlying layer of magma is deformed into a sheet that ruptures, thereby creating a Strombolian explosion through the impulsive releases of gas and resultant short-lived jet that carries with it pyroclastic fragments of the ruptured sheet. Because the magma contains bubbles over a range of sizes, the sheet ruptures into a polyhedral network of holes and filaments that are flung outward at high velocities by the combined upward motion of the slug and the rapid expansion and outflow of gas, with inertial forces stretching the filaments until breakup into pyroclasts.

10.4. Shear fragmentation

I strain rates near the conduit walls become sufficiently high to intersect the glass transition, it is hypothesized that the magma may undergo brittle fragmentation due to shear [Goto 1999, Gonnermann and Manga 2003]. This may produce intermittent permeable pathways to facilitate enhanced outgassing, thereby affecting the explosive potential [Gonnermann and Manga 2003], a hypothesis that is consistent with volatile contents measured in pyroclastic obsidian Rust et al. [2004], as well as observations of magma degassing during effusive eruptions. Brittle shear fragmentation was attained experimentally at stresses of approximately 10-100 MPa, corresponding to strain rates of the order of 10^{-2} to 10^{-4} s^{-1}, and it was furthermore affected by the presence of crystals [e.g., Lavallee et al. 2007].

10.5. Secondary Fragmentation

Pyroclasts formed by magma fragmentation may be reduced to smaller size by *secondary fragmentation*, due high energy collisions within the volcanic conduit. During secondary fragmentation larger clasts are more likely fragmented to smaller size. Because the number of disruptive collisions scales with the fragmentation depth, the presence of abundant large clasts in pyroclastic deposits may therefore reflect shallow fragmentation. In contrast, large fragmentation depths are expected to result in enhanced ash production, changing the grain size distribution of pyroclastic deposits toward larger power law exponents, all else being equal. Secondary fragmentation may also occur above the vent within the volcanic jet and within pyroclastic flows. Because the clasts produced by secondary fragmentation are angular in shape, they may be indistinguishable from those produced by primary fragmentation. In contrast, low energy collisions will result in rounding of clasts, but also produce ash.

SUMMARY POINTS

1. The glass transition is a reversible transition between elastic/brittle and viscous/ductile behavior of amorphous materials. It is related to the relaxation rate of the molecular structure, which is inversely proportional to the Maxwell time, defined as the ratio of viscosity over elastic modulus. If deformation rates are much larger than the reciprocal Maxwell time, the material will respond in a elastic or brittle manner, and viscously otherwise. Brittle failure is a consequence of breaking bridging oxygen bonds within the molecular silica network. Because viscosity is strongly temperature dependent, the glass transition is a function of both temperature and deformation rate.
2. Brittle fragmentation requires magma of high viscosity. High viscosity hinders bubble growth and leads to bubble overpressure. High viscosity also results in steep pressure gradients, due to viscous stresses during magma flow within the conduit. Furthermore, brittle deformation requires that deformation rates exceed the structural relaxation rate, which scales with reciprocal viscosity.
3. Fragmentation of mafic magma is by fluid-dynamic breakup, due to inertial forces generated during the expansion of magmatic gases and turbulence with the gas-magma jet.
4. Brittle fragmentation by shear near the conduit walls is seismically detectable, provides pathways for gas escape, and affects the dynamic conditions for effusive or explosive activity.
5. Pyroclastic fragment sizes depend on the energy balance of converting potential energy of compressed magmatic gases into new surface area and kinetic energy. Collisions between magma fragments result in secondary fragmentation, which shifts fragment size distributions toward smaller fragment size and larger power-law exponents.

LITERATURE CITED

G. Adam and J. H. Gibbs. On the temperature dependence of cooperative relaxation properties in glass-forming liquids. *J. Chem. Phys.*, 43:139–146, 1965.

M. Alidibirov. A model for viscous magma fragmentation during volcanic blasts. *Bull. Volcanol.*, 56:459–465, 1994.

M. Alidibirov and D. B. Dingwell. Magma fragmentation by rapid decompression. *Nature*, 380:146–148, 1996.

P. Allard, M. Burton, and F. Mure. Spectroscopic evidence for a lava fountain driven by previously accumulated magmatic gas. *Nature*, 433:407–410, 2005.

L. Arbaret, M. Bystricky, and R. Champallier. Microstructures and rheology of hydrous synthetic magmatic suspensions deformed in torsion at high pressure. *Journal of Geophysical Research-Solid Earth*, 112, 2007.

N. S. Bagdassarov and D. B. Dingwell. A Rheological Investigation Of Vesicular Rhyolite. *Journal Of Volcanology And Geothermal Research*, 50:307–322, 1992.

J. Barclay, M. J. Rutherford, M. R. Carroll, M. D. Murphy, J. D. Devine, J. Gardner, and R. S. J. Sparks. Experimental phase equilibria constraints on pre-eruptive storage conditions of the Soufriere Hills magma. *Geophys. Res. Lett.*, 25:3437–3440, 1998.

H. A. Barnes. Thixotropy - a review. *Journal of Non-Newtonian Fluid Mechanics*, 70:1–33, 1997.

H. A. Barnes. The yield stress - a review or 'pi alpha nu tau alpha rho epsilon iota' - everything flows? *Journal of Non-Newtonian Fluid Mechanics*, 81:133–178, 1999.

J. Bear. *Dynamics of fluids in porous media*. Dover, Mineola, N. Y., 1988.

H. Behrens and Y. X. Zhang. Ar diffusion in hydrous silicic melts: implications for volatile diffusion mechanisms and fractionation. *Earth. Planet. Sci. Lett.*, 192:363–376, 2001.

R. B. Bird, W. E. Steward, and Lightfoot E. N. *Transport Phenomena*. John Wiley, New York, 1960.

J. G. Blank. *An experimental investigation of the behavior of carbon dioxide in rhyolitic melt*. PhD thesis, California Institute of Technology, 1993.

J. G. Blank and R. A. Brooker. Experimental studies of carbon-dioxide in silicate melts - solubility, speciation, and stable carbon-isotope behavior. In M. R. Carroll and J. R. Holloway, editors, *Volatiles in Magmas*, volume 30 of *Reviews in Mineralogy*, pages 157–186. American Mineralogical Society, 1994.

J. G. Blank, E. M. Stolper, and Y. Zhang. Diffusion of CO_2 in rhyolitic melt. *Trans. Am. Geophys. Union*, 75:353, 1991.

G. Boudon, B. Villemant, J. C. Komorowski, P. Ildefonse, and M. P. Semet. The hydrothermal system at Soufriere Hills volcano, Montserrat (West Indies): Characterization and role in the on-going eruption. *Geophys. Res. Lett.*, 25:3693–3696, 1998.

E. Bourgue and P. Richet. The effects of dissolved CO_2 on the density and viscosity of silicate melts: a preliminary study. *Earth Planet Sci. Lett.*, 193:57–68, 2001.

R. Brückner and J. Deubener. Description and interpretation of the two phase flow behaviour of melts with suspended crystals. *J. Non-Cryst. Solids*, 209:283–291, 1997.

C. W. Burnham. Water and magmas: a mixing model. *Geochim. Cosmomchim. Acta*, 39:1077–1084, 1975.

C. W. Burnham. Development of the Burnham model for prediction of H_2O solubility in magmas. *Rev. Mineral.*, 30:123–129, 1994.

M. R. Burton, H. M. Mader, and M. Polacci. The role of gas percolation in quiescent degassing of persistently active basaltic volcanoes. *Earth. Planet. Sci. Lett.*, 264:46–60, 2007.

L. Caricchi, L. Burlini, P. Ulmer, T. Gerya, M. Vassalli, and P. Papale. Non-Newtonian rheology of crystal-bearing magmas and implications for magma ascent dynamics. *Earth. Planet. Sci. Lett.*, 264:402–419, 2007.

P. C. Carman. Fluid flow through a granular bed. *Trans. Inst. Chem. Eng. London*, 15:150–156, 1937.

M. R. Carroll and J. D. Webster. Solubilities of Sulfur, Noble-Gases, Nitrogen, Chlorine, and Fluorine in Magmas. *Volatiles in Magmas*, 30:231–279, 1994.

T. Churikova, G. Worner, N. Mironov, and A. Kronz. Volatile (S, Cl and F) and fluid mobile trace element compositions in melt inclusions: implications for variable fluid sources across the Kamchatka arc. *Contrib. Mineral. Petrol.*, 154:217–239, 2007.

N. Cluzel, D Laporte, A. Provost, and I. Kannewischer. Kinetics of heterogeneous bubble nucleation in rhyolitic melts: implications for the number density of bubbles in volcanic conduits and for pumice textures. *Contrib. Mineral. Petrol.*, 156:745–763, 2008.

C. F. Colebrook. Turbulent flowin pipes with particular reference to the transition between the smooth and rough pipe laws. *Journal of the Institute of Civil Engineers London*, 11:133–156, 1939.

A. Costa. Viscosity of high crystal content melts: Dependence on solid fraction. *Geophys. Res. Lett.*, 32: doi:10.1029/2005GL024303, 2005.

W. Degruyter, O. Bachmann, A. Burgisser, and M. Manga. The effects of outgassing on the transition between effusive and explosive silicic eruptions. *Earth Planet. Sci. Lett.*, 349-350:161–170, 2012. .

P. Del Carlo and M. Pompilio. The relationship between volatile content and the eruptive style of basaltic magma: the Etna case. *Annals of Geophysics*, 47:1423–1432, 2004.

J. Deubener. Flow of partially crystallised silicate melts. *Glass Sci. Technol.*, 76:20–25, 2003.

J. Deubener and R. Brückner. Influence of nucleation and crystallisation on the rheological properties of lithium disilicate melt. *J. Non-Cryst. Solids*, 209:96–111, 1997.

D. B. Dingwell. Volcanic dilemma: Flow or blow? *Science*, 273:1054–1055, 1996.

D. B. Dingwell. The brittle-ductile transition in high-level granitic magmas: Material constraints. *Journal Of Petrology*, 38:1635–1644, 1997.

D. B. Dingwell and S. L. Webb. Structural relaxation in silicate melts and non-Newtonian melt rheology in geologic processes. *Phys. Chem. Miner.*, 16:508–516, 1989.

F. Dobran. Nonequilibrium-Flow in Volcanic Conduits and Application to the Eruptions of Mt St-Helens on May 18, 1980, and Vesuvius in Ad 79. *Journal of Volcanology and Geothermal Research*, 49:285–311, 1992.

F. Dobran. *Volcanic processes mechanisms in material transport*. Kluwer Academic / Plenum Publishers, New York, N. Y., 2001.

Z. Duan, M. M. Yovanovich, and Y. S. Muzychka. Pressure drop for fully developed turbulent flow in circular and noncircular ducts. *ASME J. Fluids Eng.*, 134:10.1115/1.4006861, 2012.

J. Dufek and G. W. Bergantz. Transient two-dimensional dynamics in the upper conduit of a rhyolitic eruption: A comparison of closure models for the granular stress. *Journal of Volcanology and Geothermal Research*, 143: 113–132, 2005.

M. Edmonds and T. M. Gerlach. Vapor segregation and loss in basaltic melts. *Geology*, 35:751–754, 2007.

M. Edmonds, C. Oppenheimer, D. M. Pyle, R. A. Herd, and G. Thompson. SO_2 emissions from Soufriere Hills Volcano and their relationship to conduit permeability, hydrothermal interaction and degassing regime. *Journal Of Volcanology And Geothermal Research*, 124:23–43, 2003.

J. Eggers and E. Villermaux. Physics of liquid jets. *Rep. Prog. Phys.*, 71, 2008.

J. C. Eichelberger. Origin of andesite and dacite: evidence of mixing at Glass Mountain in California and at other circum-Pacific volcanoes. *Geological Society of America Bulletin*, 86:1381–1391, 1975.

J. C. Eichelberger, C. R. Carrigan, H. R. Westrich, and R. H. Price. Non-explosive silicic volcanism. *Nature*, 323: 598–602, 1986.

C. H. Geschwind and M. J. Rutherford. Crystallization of Microlites During Magma Ascent - the Fluid-Mechanics of 1980-1986 Eruptions at Mount-St-Helens. *Bulletin of Volcanology*, 57:356–370, 1995.

W. F. Giggenbach. Chemical composition of volcanic gases. In R. Scarpa and R. I. Tilling, editors, *Monitoring and mitigation of volcano hazards*, pages 221–256. Springer Verlag, Berlin, 1996.

D. Giordano and D. B. Dingwell. Viscosity of hydrous Etna basalt: implications for Plinian-style basaltic eruptions. *Bulletin of Volcanology*, 65:8–14, 2003.

D. Giordano, A. R. L. Nichols, and D. B. Dingwell. Glass transition temperatures of natural hydrous melts: a relationship with shear viscosity and implications for the welding process. *J. Volcanol. Geotherm. Res.*, 142: 105–118, 2005.

D. Giordano, A. Mangiacapra, M. Potuzak, J. K. Russell, C. Romano, D. B. Dingwell, and A. Di Muro. An expanded non-Arrhenian model for silicate melt viscosity: A treatment for metaluminous, peraluminous and peralkaline liquids. *Chem. Geol.*, 229:42–56, 2006.

H. M. Gonnermann and J. E. Gardner. Homogeneous bubble nucleation in rhyolitic melt: Experiments and non-classical theory. *Geochem. Geophys. Geosys.*, 14, 2007. .

H. M. Gonnermann and M. Manga. Explosive volcanism may not be an inevitable consequence of magma fragmentation. *Nature*, 426:432–435, 2003.

H. M. Gonnermann and M. Manga. The fluid mechanics inside a volcano. *Annual Review of Fluid Mechanics*, 39: 321–356, 2007.

H. M. Gonnermann and M. Manga. Dynamics of magma ascent in the volcanic conduit. In S. A. Fagents, T. K. P. Gregg, and R. M. C. Lopes, editors, *Modeling Volcanic Processes - The Physics and Mathematics of Volcanism*. Cambridge University Press, 2013.

H. M. Gonnermann and S. Mukhopadhyay. Non-equilibrium degassing and a primordial source for helium in ocean-island volcanism. *Nature*, 449:1037–1040, 2007.

A. Goto. A new model for volcanic earthquake at Unzen Volcano: Melt rupture model. *Gephys. Res. Lett.*, 26: 2541–2544, 1999.

K. U. Hess and D. B. Dingwell. Viscosities of hydrous leucogranitic melts: A non-Arrhenian model. *Am. Mineral.*, 81:1297–1300, 1996.

M. M. Hirschmann. Water, melting, and the deep Earth H_2O cycle. *Annu. Rev. Earth Planet. Sci.*, 34:629–653, 2006.

J. R. Holloway and J. G. Blank. Application of experimental results to C-O-H species in natural melts. *Rev. Mineral.*, 30:187–230, 1994.

B. F. Houghton and H. M. Gonnermann. Basaltic explosive volcanism: constraints from deposits and models. *Chemie der Erde*, 68:117–140, 2008.

H. J. Hui and Y. X. Zhang. Toward a general viscosity equation for natural anhydrous and hydrous silicate melts. *Geochim. Cosmochim. Acta*, 71:403–416, 2007.

M. Ichihara, D. Rittel, and B. Sturtevant. Fragmentation of a porous viscoelastic material: implications to magma fragmentation. *J. Geophys. Res.*, 107:doi: 10.1029/2001JB000591, 2002.

Y. Ida. Driving force of lateral permeable gas flow in magma and the criterion of explosive and effusive eruptions. *Journal of Volcanology and Geothermal Research*, 162:172–184, 2007.

C. Jaupart. Gas loss from magmas through conduit walls during eruption. In J. S. Gilbert and R. S. J. Sparks, editors, *The physics of explosive volcanic eruptions*, volume 145, pages 73–90. Geological Society, London, 1998.

C. Jaupart and C. J. Allegre. Gas Content, Eruption Rate and Instabilities of Eruption Regime in Silicic Volcanos. *Earth. Planet. Sci. Lett.*, 102:413–429, 1991.

A. J. R. Kent. Melt inclusions in basaltic and related volcanic rocks. *Rev. Minearl. Geochem.*, 69:273–331, 2008.

H. Keppler. Experimental evidence for the source of excess sulfur in explosive volcanic eruptions. *Science*, 284: 1652–1654, 1999.

C. Klug and K. V. Cashman. Vesiculation Of May 18, 1980, Mount St. Helens Magma. *Geology*, 22:468–472, 1994.

C. Klug and K. V. Cashman. Permeability development in vesiculating magmas: implications for fragmentation. *Bull. Volcanol.*, 58:87–100, 1996.

T. Koyaguchi. An analytical study for 1-dimensional steady flow in volcanic conduits. *Journal Of Volcanology And Geothermal Research*, 143:29–52, 2005.

T. Koyaguchi and N. K. Mitani. A theoretical model for fragmentation of viscous bubbly magmas in shock tubes. *Journal Of Geophysical Research-Solid Earth*, 110, 2005.

G. La Spina, M. de' Michieli Vitturi, and A. B. Clarke. Transient numerical model of magma ascent dynamics: application to the explosive eruptions at the Soufrire Hills Volcano. *J. Volcanol. Geothem. Res.*, 336:118–139, 2017. .

R. A. Lange. The effect of H_2O, CO_2 and F on the density and viscosity of silicate melts. *Rev. Mineral.*, 30:331–369, 1994.

J. F. Larsen, M. H. Denis, and J. E. Gardner. Experimental study of bubble coalescence in rhyolitic and phonolitic melts. *Geochim. Cosmochim. Acta*, 68:333–344, 2004.

Y. Lavallee, K. U. Hess, B. Cordonnier, and D. B. Dingwell. Non-Newtonian rheological law for highly crystalline dome lavas. *Geology*, 35:843–846, 2007.

M. J. Le Bas, R. W. Le Maitre, A. Streckeisen, and B. Zamettin. A chemical classification of volcanic rocks based on the total alkali-silica diagram. *Journal of Petrology*, 27:745–750, 1986.

A. M. Lejeune and P. Richet. Rheology Of Crystal-Bearing Silicate Melts - An Experimental-Study At High Viscosities. *Journal Of Geophysical Research-Solid Earth*, 100:4215–4229, 1995.

A. M. Lejeune, Y. Bottinga, T. W. Trull, and P. Richet. Rheology of bubble-bearing magmas. *Earth. Planet. Sci. Lett.*, 166:71–84, 1999.

N.G. Lensky, V. Lyakhovsky, and O. Navon. Radial variations of melt viscosity around growing bubbles and gas overpressure in vesiculating magmas. *Earth Planet. Sci. Lett.*, 186:1–6, 2001.

Y. Liu, Y. X. Zhang, and H. Behrens. Solubility of H_2O in rhyolitic melts at low pressures and a new empirical model for mixed H_2O-CO_2 solubility in rhyolitic melts. *Journal Of Volcanology And Geothermal Research*, 143: 219–235, 2005.

E. W. Llewellin and A. Manga. Bubble suspension rheology and implications for conduit flow. *Journal Of Volcanology And Geothermal Research*, 143:205–217, 2005.

E. W. Llewellin, H. M. Mader, and S. D. R. Wilson. The rheology of a bubbly liquid. *Proceedings Of The Royal Society Of London Series A-Mathematical Physical And Engineering Sciences*, 458:987–1016, 2002.

A. S. Lloyd, T. Plank, P. Ruprecht, E. H. Hauri, and W. Rose. Volatile loss from melt inclusions in pyroclasts of differing sizes. *Contrib. Mineral. Petrol.*, 165:129–153, 2012. .

H. M. Mader. Conduit flow and fragmentation. In J. S. Gilbert and R. S. J. Sparks, editors, *The physics of explosive volcanic eruptions*, volume 145, pages 51–71. Geological Society, London, 1998.

H. M. Mader, E. W.. Llewellin, and S. P. Mueller. The rheology of two-phase magmas: A review and analysis. *Journal Of Volcanology And Geothermal Research*, 257:135–158, 2013.

M. Manga and M. Loewenberg. Viscosity of magmas containing highly deformable bubbles. *Journal Of Volcanology And Geothermal Research*, 105:19–24, 2001.

M. Mangan and T. Sisson. Evolution of melt-vapor surface tension in silicic volcanic systems: Experiments with hydrous melts. *J. Geophys. Res.*, 110:doi:10.1029/2004JB003215, 2005.

C. Martel, D. B. Dingwell, O. Spieler, M. Pichavant, and M. Wilke. Fragmentation of foamed silicic melts: an experimental study. *Earth. Planet. Sci. Lett.*, 178:47–58, 2000.

C. Martel, D. B. Dingwell, O. Spieler, M. Pichavant, and M. Wilke. Experimental fragmentation of crystal- and vesicle-bearing silicic melts. *Bulletin Of Volcanology*, 63:398–405, 2001.

H. Massol and T. Koyaguchi. The effect of magma flow on nucleation of gas bubbles in a volcanic conduit. *Journal Of Volcanology And Geothermal Research*, 143:69–88, 2005.

L. G. Mastin. Insights into volcanic conduit flow from an open-source numerical model. *Geochemistry Geophysics Geosystems*, 3, 2002.

L. G. Mastin. The controlling effect of viscous dissipation on magma flow in silicic conduits. *Journal Of Volcanology And Geothermal Research*, 143:17–28, 2005.

L. G. Mastin and M. S. Ghiorso. A numerical program for steady-state flow of magma-gas mixtures through vertical eruptive conduits, 2000.

P. F. McMillan. Water solubility and speciation models. In M. R. Carroll and J. R. Holloway, editors, *Volatiles in Magmas*, volume 30 of *Reviews in Mineralogy*, pages 131–156. Mineralogical Society of America, 1994.

N. Metrich and M. J. Rutherford. Low pressure crystallization paths of H2O-saturated basaltic-hawaiitic melts from Mt Etna: Implications for open-system degassing of basaltic volcanoes. *Geochim. Cosmochim. Acta*, 62: 1195–1205, 1998.

N. Metrich, A. Bertagnini, P. Landi, and M. Rosi. Crystallization driven by decompression and water loss at Stromboli volcano (Aeolian Islands, Italy). *Journal of Petrology*, 42:1471–1490, 2001.

N. Metrich, P. Allard, N. Spilliaert, D. Andronico, and M. Burton. 2001 flank eruption of the alkali- and volatile-rich primitive basalt responsible for Mount Etna's evolution in the last three decades. *Earth. Planet. Sci. Lett.*, 228: 1–17, 2004.

C. T. Moynihan. Structural relaxation and the glass transition. *Rev. Mineral. Geochem.*, 32:1–19, 1995.

S. Mueller, O. Melnik, O. Spieler, B. Scheu, and D. B. Dingwell. Permeability and degassing of dome lavas undergoing rapid decompression: An experimental determination. *Bulletin Of Volcanology*, 67:526–538, 2005.

S. Mueller, B. Scheu, O. Spieler, and D. B. Dingwell. Permeability control on magma fragmentation. *Geology*, 36: 399402, 2008.

B. R. Munson, D. F. Young, and T. H.. Okiishi. *Fundamentals of Fluid Mechanics, Third Edition*. John Wiley & Sons, New York, 1998.

T. Murase and A. R. McBirney. Properties of Some Common Igneous Rocks and Their Melts at High-Temperatures. *Geol. Soc. Am. Bull.*, 84:3563–3592, 1973.

Y. S. Muzychka and M. M. Yovanovich. Pressure drop in laminar developing flow in noncircular ducts: a scaling and modeling approach. *ASME J. Fluids Eng.*, 131, 2009. .

A. Namiki and M. Manga. Response of a bubble bearing viscoelastic fluid to rapid decompression: Implications for explosive volcanic eruptions. *Earth. Planet. Sci. Lett.*, 236:269–284, 2005.

S. Newman and J. B. Lowenstern. VOLATILECALC: A siliate melt-H_2O-CO_2 solution model written in Visual Basic for excel. *Comp. Geosci.*, 28:597–604, 2002.

M. Nowak, D. Schreen, and K. Spickenbom. Argon and CO2 on the race track in silicate melts: A tool for the development of a CO, speciation and diffusion model. *Geochim. Cosmochim. Acta*, 68:5127–5138, 2004.

R. Pal. Complex shear modulus of concentrated suspensions of solid spherical particles. *J. Colloid Interface Sci.*, 245:171–177, 2002.

R. Pal. Rheological behavior of bubble-bearing magmas. *Earth. Planet. Sci. Lett.*, 207:165–179, 2003.

R. Pal. Rheological constitutive equation for bubbly suspensions. *Ind. Eng. Chem. Res.*, 43:5372–5379, 2004.

P. Papale. Numerical simulations of magma ascent along volcanic conduits. *Physics And Chemistry Of The Earth Part A-Solid Earth And Geodesy*, 24:957–961, 1999.

P. Papale. Dynamics of magma flow in volcanic conduits with variable fragmentation efficiency and nonequilibrium pumice degassing. *Journal Of Geophysical Research-Solid Earth*, 106:11043–11065, 2001.

P. Papale, R. Moretti, and D. Barbato. The compositional dependence of the saturation surface of H2O+CO2 fluids in silicate melts. *Chem. Geol.*, 229:78–95, 2006.

E. A. Parfitt, L. Wilson, and J. W. Head. Basaltic Magma Reservoirs - Factors Controlling Their Rupture Characteristics and Evolution. *Journal of Volcanology and Geothermal Research*, 55:1–14, 1993.

A. Proussevitch and D. Sahagian. Bubbledrive-1: A numerical model of volcanic eruption mechanisms driven by disequilibrium magma degassing. *J. Volcanol. Geotherm. Res.*, 143:89–111, 2005.

A.A. Proussevitch, D.L. Sahagian, and A.T. Anderson. Dynamics of diffusive bubble growth in magmas: Isothermal case. *J. Geophys. Res.*, 98:22,283–22,307, 1993.

D. M. Pyle and D. L. Pyle. Bubble Migration and the Initiation of Volcanic-Eruptions. *Journal of Volcanology and Geothermal Research*, 67:227–232, 1995.

J. F. Richardson and W. N. Zaki. The Sedimentation of a Suspension of Uniform Spheres under Conditions of Viscous Flow. *Chem. Eng. Sci.*, 3:65–73, 1954.

P. Richet. Viscosity and configurational entropy of silicate melts. *Geochim. Cosmochim. Acta*, 48:471–483, 1984.

P. Richet, R. A. Robie, and B. S. Hemingway. Low-temperature dependence of carbon dioxide solubility in tholeiitic basaltic melts. *Geochim. Cosmochim. Acta*, 50:1521–1533, 1986.

E. Romenski, A. D. Resnyansky, and E. F. Toro. Conservative hyperbolic formulation for compressible two-phase flow with different phase pressures and temperatures. *Quart. Appl. Math.*, 65:259–279, 2007.

A. C. Rust and M. Manga. Bubble shapes and Orientations in low Re simple shear flow. *J. Colloid Interface Sci.*, 249:476–480, 2002.

A. C. Rust, M. Manga, and K. V. Cashman. Determining flow type, shear rate and shear stress in magmas from bubble shapes and orientations. *Journal Of Volcanology And Geothermal Research*, 122:111–132, 2003.

A. C. Rust, K. V. Cashman, and P. J. Wallace. Magma degassing buffered by vapor flow through brecciated conduit margins. *Geology*, 32:349–352, 2004.

E. H. Rutter, K. H. Brodie, and D. H. Irving. Flow of synthetic, wet, partially molten "granite" under undrained conditions: An experimental study. *Journal of Geophysical Research-Solid Earth*, 111, 2006.

M. O. Saar, M. Manga, K. V. Cashman, and S. Fremouw. Numerical models of the onset of yield strength in crystal-melt suspensions. *Earth. Planet. Sci. Lett.*, 187:367–379, 2001.

L. E. Scriven. On The Dynamics Of Phase Growth. *Chem. Eng. Sci.*, 10:1–13, 1959.

A. G. Simakin and T. P. Salova. Plagioclase crystallization from a hawaiitic melt in experiments and in a volcanic conduit. *Petrology*, 12:82–92, 2004.

J. H. Simmons. Morey Award paper - What is so exciting about non-linear viscous flow in glass, molecular dynamics simulations of brittle fracture and semiconductor-glass quantum composites. *J. Non-Cryst. Solids*, 239:1–15, 1998.

R. S. J. Sparks. The dynamics of bubble formation and growth in magmas: A review and analysis. *J. Volc. Geotherm. Res.*, 3:1–37, 1978.

R. S. J. Sparks, J. Barclay, C. Jaupart, H. M. Mader, and J. C. Phillips. Physical aspects of magmatic degassing I. Experimental and theoretical constraints on vesiculation. In *Volatiles In Magmas*, volume 30 of *Reviews In Mineralogy*, pages 413–445. Mineralogical Society of America, Washington D. C., 1994.

O. Spieler, B. Kennedy, U. Kueppers, D. B. Dingwell, B. Scheu, and J. Taddeucci. The fragmentation threshold of pyroclastic rocks. *Earth. Planet. Sci. Lett.*, 226:139–148, 2004.

D. J. Stein and F. J. Spera. Shear viscosity of rhyolite-vapor emulsions at magmatic temperatures by concentric cylinder rheometry. *Journal Of Volcanology And Geothermal Research*, 113:243–258, 2002.

R. J. Stevenson, D. B. Dingwell, S. L. Webb, and T. G. Sharp. Viscosity of microlite-bearing rhyolitic obsidians: An experimental study. *Bulletin Of Volcanology*, 58:298–309, 1996.

S. Tait, C. Jaupart, and S. Vergniolle. Pressure, Gas Content And Eruption Periodicity Of A Shallow, Crystallizing Magma Chamber. *Earth. Planet. Sci. Lett.*, 92:107–123, 1989.

M. Thies. *Herstellung und rheologische Eigenschaften von porösen Kalk-Natron-Silicatschmelzen*. Ph. d., RU, 2002.

N. Thomas, C. Jaupart, and S. Vergniolle. On The Vesicularity Of Pumice. *Journal Of Geophysical Research-Solid Earth*, 99:15633–15644, 1994.

A. Toramaru. Numerical Study Of Nucleation And Growth Of Bubbles In Viscous Magmas. *Journal Of Geophysical Research-Solid Earth*, 100:1913–1931, 1995.

H. Tuffen, D. B. Dingwell, and H. Pinkerton. Repeated fracture and healing of silicic magma generate flow banding and earthquakes? *Geology*, 31:1089–1092, 2003.

F. J. Turner and Verhoogen J. *Igneous and metamorphic petrology*. McGraw-Hill, New York, 1960.

E. Villermaux. Fragmentation. *Annual Review of Fluid Mechanics*, 39:419–446, 2007.

P. J. Wallace. Volatiles in subduction zone magmas: concentrations and fluxes based on melt inclusion and volcanic gas data. *J. Volc. Geotherm. Res.*, 140:217–240, 2005.

P. J. Wallace, S. A. R. Carn, I. William, G. J. S. Bluth, and T. M. Gerlach. Integrating petrologic and remote sensing perspectives on magmatic volatiles and volcanic degassing. *Eos, Transactions, American Geophysical Union*, 84:446–447, 2003.

E. B. Watson. Diffusion of dissolved CO_2 and Cl in hydrous silicic to intermediate magmas. *Geochim. Cosmochim. Acta*, 55:1897–1902, 1991.

E. B. Watson. Diffusion in volatile-bearing magmas. *Rev. Mineral.*, 30:371–411, 1994.

S. Webb. Silicate melts: Relaxation, rheology, and the glass transition. *Rev. Geophys.*, 35:191–218, 1997.

S. L. Webb and D. B. Dingwell. The Onset Of Non-Newtonian Rheology Of Silicate Melts - A Fiber Elongation Study. *Phys. Chem. Miner.*, 17:125–132, 1990a.

S. L. Webb and D. B. Dingwell. Non-Newtonian rheology of igneous melts at high stresses and strain rates: experimental results for rhyolite, andesite, basalt, and nephelinite. *J. Geophys. Res.*, 95:15,695–15,701, 1990b.

A. G. Whittingon, B. M. Hellwig, H. Behrens, B. Joachim, A. Stechern, and F. Vetere. The viscosity of hydrous dacitic liquids: implications for the rheology of evolving silicic magmas. *Bull. Volcanol.*, 71:185–199, 2009.

L. Wilson. Volcanic Eruptive Conditions - the Influence of Magma Gas Content and Conduit Geometry. *Journal of the Geological Society*, 137:111–111, 1980a.

L. Wilson. Relationships Between Pressure, Volatile Content And Ejecta Velocity In 3 Types Of Volcanic Explosion. *Journal Of Volcanology And Geothermal Research*, 8:297–313, 1980b.

L. Wilson. Explosive volcanic eruptions - X. The influence of pyroclast size distributions and released magma gas contents on the eruption velocities of pyroclasts and gas in Hawaiian and Plinian eruptions. *Geophysical Journal International*, 136:609–619, 1999.

L. Wilson, R. S. J. Sparks, and G. P. L. Walker. Explosive Volcanic-Eruptions .4. The Control Of Magma Properties And Conduit Geometry On Eruption Column Behavior. *Geophysical Journal Of The Royal Astronomical Society*, 63:117–148, 1980.

J. Wong and C. A. Angell. *Glass structure by spectroscopy*. Dekker, New York, 1976.

A. W. Woods and S. S. S. Cardoso. Triggering basaltic volcanic eruptions by bubble-melt separation. *Nature*, 385:

518–520, 1997.

A. W. Woods and T. Koyaguchi. Transitions between explosive and effusive eruption of silicic magmas. *Nature*, 370:641–644, 1994.

S. Yoshida and T. Koyaguchi. A new regime of volcanic eruption due to the relative motion between liquid and gas. *Journal Of Volcanology And Geothermal Research*, 89:303–315, 1999.

Y. Z. Yue and R. Brückner. A New Description And Interpretation Of The Flow Behavior Of Glass-Forming Melts. *J. Non-Cryst. Solids*, 180:66–79, 1994.

Y. X. Zhang. A criterion for the fragmentation of bubbly magma based on brittle failure theory. *Nature*, 402: 648–650, 1999.

Y. X. Zhang and H. Behrens. H_2O diffusion in rhyolitic melts and glasses. *Chem. Geol.*, 169:243–262, 2000.

Y. X. Zhang, Z. J. Xu, M. F. Zhu, and H. Y. Wang. Silicate melt properties and volcanic eruptions. *Reviews of Geophysics*, 45, 2007.

CIDER 2019 Lecture Notes
Appendix: Conservation Equations

Helge M. Gonnermann, *Earth, Environmental and Planetary Sciences, Rice University*

Contents

1. Preliminaries

1.1. Derivatives in one dimension

We distinguish between independent variables, such as spatial location and time, and dependent variables which vary in space or time. For example, take some quantity such as pressure, P, or temperature, T. Usually we are interested to learn about how this variable varies in space and/or over time. Typically in problems of mass and energy transport the rate at which such quantities change with respect to time depends on the spatial derivatives (gradients) of these quantities at the given time.

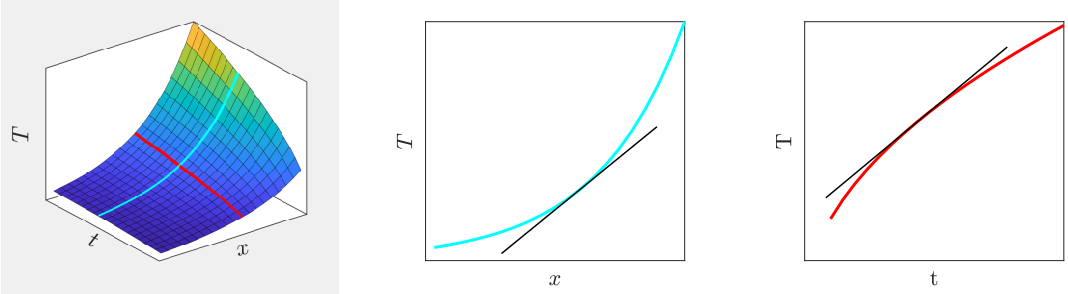

(a) $T(t, x)$ (b) $T(t_a, x)$ (c) $T(t, x_b)$

Figure 1: Example of a function $T(t, x)$ that depends on time, t, and one spatial dimension, x. In (a) the location of the functions $T(t_a, x)$ and $T(t, x_b)$, which are graphed in (b) and (c), respectively, are shown as the cyan and red curves, respectively. In (b) the gradient, $\partial T/\partial x$, at one specific point is shown as a tangent line. In (c) the rate of change, $\partial T/\partial t$, at one specific time is shown as a tangent line.

1.1.1. Dependent on space, but independent of time. The value of the variable is dependent on space, but independent of time. Time independence usually implies that processes that affect our dependent variable have reached a *steady state*, which could also be an *equilibrium state*. In the case of temperature within a one-dimensional Cartesian coordinate system, we have $T = f(x)$, and dT/dx is the *gradient* of temperature.

1.1.2. Dependent on time, but independent of space. The value of the variable changes with time, and is either independent of space or we are interested in its value at specific point in space only. An example for the former would be the average temperature within a dike, $\bar{T}$, which may change in time but there is no dependence on space whatsoever, and an example of the latter would be the temperature at the center

of the dike. In the case of temperature as our dependent variable within a one-dimensional Cartesian coordinate system, we have $T = f(t)$, and dT/dt is the *rate of change* of temperature with respect to time.

1.1.3. Dependent on time and space. The value of the variable depends on space and on time. For example the magma temperature at any location within the dike. In the case of temperature as our dependent variable within a one-dimensional Cartesian coordinate system, we have $T = f(t, x)$, and how the value of T changes will require that we account for its rate of change with respect to time $\partial T/\partial t$ at any given point in space. In this case we use a *partial derivative*, because the value of T does not only depend on time, but also on the spatial location we are considering. Moreover, the rate of change in T at any given point may depend on its gradient at that point.

1.2. Derivatives in two dimensions

In this case temperature is defined by a two-dimensional *scalar field*, given either by $\psi = f(x, y)$ or by $\psi = f(t, x, y)$. We have to use partial derivatives for the rate of change with respect to time, and the change in space is given by the gradient $\nabla\psi = \partial\psi/\partial x + \partial\psi/\partial y$. Variables that have magnitude and direction, of which velocity ($\mathbf{U}$) is an example, are defined by a *vector field*, $\mathbf{U} = [u, v]$. Vector fields can be obtained from the gradient of a scalar field and their spatial variability can be described by the divergence, $\nabla \cdot \mathbf{U} = \partial u/\partial x + \partial v/\partial y$, and the curl, $\nabla \times \mathbf{U} = (\partial v/\partial x - \partial u/\partial y)\mathbf{e_3}$.

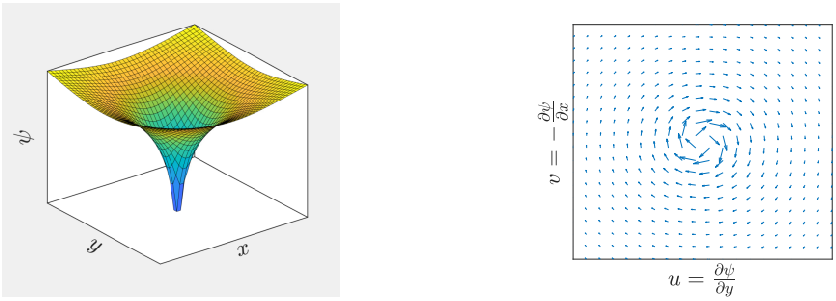

(a) $\psi(x, y)$ (b) $U = [u, v]$

Figure 2: Example of a two-dimensional scalar field, that is a potential function $\psi(x, y)$ that depends on the two spatial coordinates x and y, together with the vector field that results from defining a vector function $\mathbf{U}(x, y) = [u(x, y), v(x, y)]$, where $u \equiv \partial\psi/\partial y$ and $v \equiv -\partial\psi/\partial x$. Note, that in the case of $\psi = f(t, x, y)$, we could show graphs of the functions $\psi(x, y)$ and $\mathbf{U}(x, y)$ at different times, t. Furthermore, given the definitions of u and v as velocity components that are based on the function ψ as stated, the function ψ is referred to as the *streamfucnction*.

2. Fick's first law (flux)

Flux, in general, refers to the rate at which some quantity passes through a surface, per unit area of that surface. This surface can, for example, be the interface between two *domains*. Surfaces across which quantities such as mass, momentum or energy, are passing are also invoked for small representative elemental volumes, also referred to as *control volumes*, that are conceptualized representations of a point within a continuous material. The sum of fluxes in and out of such a control volume result in mathematical expressions for the conservation of quantities of interest within the control volume, that is at a given point within the continuous medium.

The following derivation of *diffusive flux* is based on the work of H.C. Berg, Random Walks in Biology, Princeton (1977), which results in a transport equation for a diffusive process. Consider a collection of particles performing a random walk in one-dimensional system of size Δx and a time interval of Δt. There are $N(x, t)$ particles at position x and time t, and there are $N(x + \Delta x, t)$ particles at position $x + \Delta x$. Assume that the particles undergo random motions of $\pm\Delta x$. Consequently, $1/2$ of the particles at x move to $x + \Delta x$ and $1/2$ of the particles at $x + \Delta x$ move to x. So the net movement to $x + \Delta x$ (to the right) is

given by

$$-\tfrac{1}{2}\left[N(x+\Delta x,t)-N(x,t)\right]. \tag{1}$$

During time interval Δt the number of particles moving across an area A is the *flux* of particles, denoted as J

$$J=-\tfrac{1}{2}\left[\frac{N(x+\Delta x,t)}{A\Delta t}-\frac{N(x,t)}{A\Delta t}\right]. \tag{2}$$

Multiplying both sides by $(\Delta x)^2$ gives

$$J=-\frac{(\Delta x)^2}{2\Delta t}\left[\frac{N(x+\Delta x,t)}{A(\Delta x)^2}-\frac{N(x,t)}{A(\Delta x)^2}\right]. \tag{3}$$

Next, we define the particle concentration as $c=N/A\Delta x$, that is the number of particles per unit volume. Furthermore, we define a constant $D\equiv(\Delta x)^2/2\Delta t$, which is referred to as *diffusivity*. We thus obtain

$$J=-D\,\frac{c(x+\Delta x,t)-c(x,t)}{\Delta x}, \tag{4}$$

which for $\Delta x\to 0$ becomes

$$J=-D\frac{dc}{dx}. \tag{5}$$

This equation is also known as *Fick's first law*, after A. Fick (On liquid diffusion, *Annalen der Physik und Chemie*, 94, 1855; *Journal of Membrane Science*, 100, 33-38, 1995, doi:10.1016/0376-7388(94)00230-v).

3. Fick's second law (conservation of mass for a diffusing substance)

As already mentioned, the sum of fluxes of some quantity into and out of a control volume yield a mathematical expression for the conservation of that quantity, referred to as a *conservation equation*. Conservation equations are general expressions that can be applicable to any quantity of interest, such as mass, momentum or energy, for example. Below we will derive the conservation equation for mass.

Once again we invoke a *control volume*, denoted by subscript 'cv', and denote the mass of our substance of interest that is contained in the control volume as $M_{\rm cv}$. For example, our $M_{\rm cv}$ could be the mass of a solute that is dissolved within a solvent that occupies our control volume. We assume that the control volume represents a point within a continuum and that the control volume is small enough that all properties within it can be treated as constant. Therefore, $M_{\rm cv}$ is given by the density of the substance occupying the control volume multiplied by its volume. In other words,

$$M_{\rm cv}=\rho\,\Delta x\,\Delta y\,\Delta x, \tag{6}$$

where x, y and z denote the (Cartesian) spatial coordinates and Δx, Δy and Δz are the width, height and depth of the control volume. In the absence of sinks or sources, for example chemical reactions, the local rate of change in mass contained within the control volume is given by

$$\frac{M_{\rm cv}}{\partial t}=\sum_{\rm in}\mathbf{J}-\sum_{\rm out}\mathbf{J}, \tag{7}$$

where

$$\mathbf{J}=[J_x,J_y,J_z] \tag{8}$$

For a three-dimensional control volume we obtain

$$\begin{aligned}\frac{\partial}{\partial t}(\rho\Delta x\Delta y\Delta z) = {} & \underbrace{J_x\Delta y\Delta z+J_y\Delta x\Delta z+J_z\Delta x\Delta y}_{\rm in} \\ & \underbrace{-\left[J_x+\frac{\partial J_x}{\partial x}\Delta x\right]\Delta y\Delta z-\left[J_y+\frac{\partial J_y}{\partial y}\Delta y\right]\Delta x\Delta z-\left[J_z+\frac{\partial J_z}{\partial z}\Delta z\right]\Delta x\Delta y}_{\rm out}.\end{aligned} \tag{9}$$

If our mass transport process is two-dimensional, for example with no mass transport or other changes in the z-direction, we can reduce this equation to two dimensions. For such a two-dimensional control volume of width Δx and height Δy we have

$$\frac{\partial}{\partial t}(\rho \Delta x \Delta y \Delta z) = \underbrace{J_x \Delta y \Delta z + J_y \Delta x \Delta z}_{\text{in}} - \underbrace{\left[J_x + \frac{\partial J_x}{\partial x}\Delta x\right]\Delta y \Delta z - \left[J_y + \frac{\partial J_y}{\partial y}\Delta y\right]\Delta x \Delta z}_{\text{out}} \tag{10}$$

and for a one-dimensional transport process we have

$$\frac{\partial}{\partial t}(\rho \Delta x \Delta y \Delta z) = \underbrace{J_x \Delta y \Delta z}_{\text{in}} - \underbrace{\left[J_x + \frac{\partial J_x}{\partial x}\Delta x\right]\Delta y \Delta z}_{\text{out}}. \tag{11}$$

Taking the two-dimensional system, which is illustrated in Figure 3, let's expand Equation (10) to yield

$$\Delta x \Delta y \Delta z \frac{\partial \rho}{\partial t} = J_x \Delta y \Delta z - J_x \Delta y \Delta z + J_y \Delta x \Delta z - J_y \Delta x \Delta z - \left[\frac{\partial J_x}{\partial x}\right]\Delta x \Delta y \Delta z - \left[\frac{\partial J_y}{\partial y}\right]\Delta x \Delta y \Delta z \tag{12}$$

or equivalently

$$\Delta x \Delta y \Delta z \frac{\partial \rho}{\partial t} = -\left[\frac{\partial J_x}{\partial x}\right]\Delta x \Delta y \Delta z - \left[\frac{\partial J_y}{\partial y}\right]\Delta x \Delta y \Delta z. \tag{13}$$

Dividing by $\Delta x \Delta y \Delta z$ finally gives

$$\frac{\partial \rho}{\partial t} + \frac{\partial J_x}{\partial x} + \frac{\partial J_y}{\partial y} = 0. \tag{14}$$

If we now revert to our definition of $\mathbf{J}$

$$J_x = -D_x \frac{\partial c}{\partial x} \tag{15}$$

$$J_y = -D_y \frac{\partial c}{\partial x} \tag{16}$$

we obtain

$$\frac{\partial \rho}{\partial t} = \frac{\partial}{\partial x}\left(D_x \frac{\partial c}{\partial x}\right) + \frac{\partial}{\partial y}\left(D_y \frac{\partial c}{\partial y}\right), \tag{17}$$

which is known as *Fick's second law*. If the diffusivity tensor is isotropic (i.e., $D_x = D_y = D$) then

$$\frac{\partial \rho}{\partial t} = \frac{\partial}{\partial x}\left(D \frac{\partial c}{\partial x}\right) + \frac{\partial}{\partial y}\left(D \frac{\partial c}{\partial y}\right), \tag{18}$$

If, furthermore D does not vary with respect to x, that is if D is constant, then

$$\frac{\partial \rho}{\partial t} = D\left(\frac{\partial^2 c}{\partial x^2} + \frac{\partial^2 c}{\partial y^2}\right). \tag{19}$$

4. Conservation of mass (continuity equation)

As already mentioned, the concept of *flux* and conservation of some quantity at some point within a continuous medium can be applied to other quantities than the mass of a solute. For example, lets assume a mass flux of fluid, $\dot{\mathbf{m}} = \rho \mathbf{U}$, due to the motion of the fluid with velocity $\mathbf{U}$ and of density ρ, both at some point x, y and z. In the absence of any sources or sinks, the change in mass, M_{cv}, inside the control volume (cv) is given by

$$\frac{dM_{\text{cv}}}{dt} = \sum_{\text{in}} \dot{\mathbf{m}} - \sum_{\text{out}} \dot{\mathbf{m}}, \tag{20}$$

where $\dot{\mathbf{m}}$ are the mass flow rates associated with the flow into and out of the control volume. Such a control volume in two dimensions is illustrated in Figure 3. The control volume has a width Δx and a height Δy

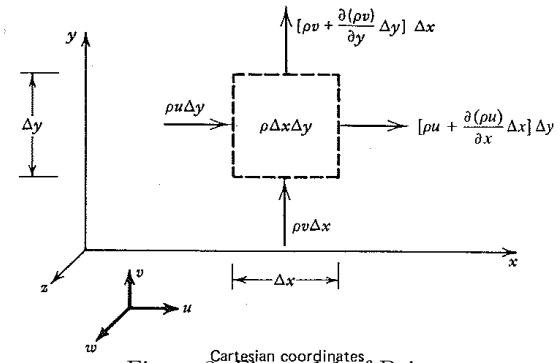

Figure 3: Figure 1.1 of Bejan

and the fluid velocity vector $\mathbf{U}$ has x- and y-components denoted as u and v, respectively. Conservation of mass requires that

$$\frac{\partial}{\partial t}(\rho\Delta x\Delta y\Delta z) = \underbrace{\rho u\Delta y\Delta z + \rho v\Delta x\Delta z}_{\text{in}} - \underbrace{\left[\rho u + \frac{\partial(\rho u)}{\partial x}\Delta x\right]\Delta y\Delta z - \left[\rho v + \frac{\partial(\rho v)}{\partial y}\Delta y\right]\Delta x\Delta z}_{\text{out}}. \tag{21}$$

Because we are dealing with a two-dimensional system, there is no flow in the z-direction and there are no changes in the z-direction. It is therefore possible to simply neglect the third dimension altogether from the get-go, which is equivalent to dividing the previous equation by Δz. This which would give

$$\frac{\partial}{\partial t}(\rho\Delta x\Delta y) = \underbrace{\rho u\Delta y + \rho v\Delta x}_{\text{in}} - \underbrace{\left[\rho u + \frac{\partial(\rho u)}{\partial x}\Delta x\right]\Delta y - \left[\rho v + \frac{\partial(\rho v)}{\partial y}\Delta y\right]\Delta x}_{\text{out}}, \tag{22}$$

which can be related more easily to Figure 3. Dividing the previous equation by $\Delta x\Delta y$ gives

$$\frac{\partial\rho}{\partial t} + \frac{\partial(\rho u)}{\partial x} + \frac{\partial(\rho v)}{\partial y} = 0. \tag{23}$$

or equivalently

$$\underbrace{\frac{\partial\rho}{\partial t}}_{\text{local change in mass}} + \underbrace{u\frac{\partial\rho}{\partial x} + v\frac{\partial\rho}{\partial y}}_{\text{advection of mass}} + \underbrace{\rho\left(\frac{\partial u}{\partial x} + \frac{\partial v}{\partial y}\right)}_{\text{divergence}} = 0. \tag{24}$$

This equation is known as the equation of continuity, which describes the time rate of change of the fluid density at a fixed point in space. We define the material or equivalently substantive derivative

$$\underbrace{\frac{D}{Dt}}_{\text{change of material element}} = \underbrace{\frac{\partial}{\partial t}}_{\text{local rate of change}} + \underbrace{\left(u\frac{\partial}{\partial x} + v\frac{\partial}{\partial y}\right)}_{\text{rate of change due to change in position}}. \tag{25}$$

The material derivative denotes the rate of change of a material element as it moves with the flow through the material continuum (*Lagrangian* frame of reference), in contrast to the local rate of change at a fixed point (*Eulerian* frame of reference). Thus, our equation for conservation of mass becomes

$$\underbrace{\frac{D\rho}{Dt}}_{\text{change in mass of material element}} = \underbrace{-\rho\left(\frac{\partial u}{\partial x} + \frac{\partial v}{\partial y}\right)}_{\text{divergence}}. \tag{26}$$

In many applications it is convenient and justifiable to treat the temporal and spatial variations in density negligible, relative to the local variations in velocity. In other words,

$$\frac{\partial\rho}{\partial t} = 0 \quad \text{and} \quad \frac{\partial\rho}{\partial x} = 0 \quad \text{and} \quad \frac{\partial\rho}{\partial y} = 0 \quad \text{and} \quad \frac{\partial\rho}{\partial z} = 0, \tag{27}$$

so that

$$\nabla \cdot \mathbf{U} = \frac{\partial u}{\partial x} + \frac{\partial v}{\partial y} + \frac{\partial w}{\partial z} = 0, \tag{28}$$

where $\mathbf{U} = [u, v, w]$. Equation (28) is known as the *continuity* equation, that is the equation of mass conservation for a fluid whose density does not change or where the change in density is negligibly small. Such a fluid is considered *incompressible*.

5. Equation of motion

5.1. In general to Navier Stokes

Taken liberally from Bird et al. - Transport Phenomena. For a *stationary* volume element $\Delta x \Delta y \Delta z$ through which fluid is flowing the momentum balance is given by

$$\left\{\begin{array}{c}\text{rate of}\\ \text{momentum}\\ \text{accumulation}\end{array}\right\} = \left\{\begin{array}{c}\text{rate of}\\ \text{momentum}\\ \text{in}\end{array}\right\} - \left\{\begin{array}{c}\text{rate of}\\ \text{momentum}\\ \text{out}\end{array}\right\} + \left\{\begin{array}{c}\text{sum of forces}\\ \text{acting on}\\ \text{volume element}\end{array}\right\}. \tag{29}$$

The rate at which the x-component of momentum enters the volume element at x is

$$\left(\rho u_x u_x\right)_x \Delta y \Delta z. \tag{30}$$

The rate at which the x-component of momentum leaves the volume element at $x + \Delta x$ is

$$\left(\rho u_x u_x\right)_{x+\Delta x} \Delta y \Delta z. \tag{31}$$

The rate at which the x-component of momentum enters the volume element across the face perpendicular to the y-direction at y is

$$\left(\rho u_y u_x\right)_x \Delta x \Delta z. \tag{32}$$

Similar expressions may be written for the other three faces. The rate at which the x-component of momentum enters the face at x by molecular transport is

$$\left(\tau_{xx}\right)_x \Delta y \Delta z \tag{33}$$

and the rate at which the x-component of momentum leaves the face at $x + \Delta x$ by molecular transport is

$$\left(\tau_{xx}\right)_{x+\Delta x} \Delta y \Delta z. \tag{34}$$

Here τ_{xx} is the *normal stress* on the surface perpendicular to the x-direction. The rate at which the x-component of momentum enters the face that is perpendicular to the y-direction at y by molecular transport is

$$\left(\tau_{yx}\right)_y \Delta x \Delta z \tag{35}$$

and the rate at which the x-component of momentum leaves the face perpendicular to the y-direction at $y + \Delta y$ by molecular transport is

$$\left(\tau_{yx}\right)_{y+\Delta y} \Delta x \Delta z. \tag{36}$$

Here τ_{yx} is the *tangential* or *shear stress* in the x-direction on the surface perpendicular to the y-direction. Similar expressions can be written for the remaining two faces. The remaining forces acting on the volume element in the x-direction are the force due to fluid pressure, p, which is a scalar quantity and the gravitational force per unit mass $\mathbf{g}$. The sum of these two forces will be

$$\left(p\right)_x - \left(p\right)_{x+\Delta x} \Delta y \Delta z + \rho g_x \Delta x \Delta y \Delta z. \tag{37}$$

Finally, the rat of accumulation of x-momentum with in the volume element is

$$\frac{\partial \rho u_x}{\partial t} \Delta x \Delta y \Delta z. \tag{38}$$

Summing all terms and taking the limit as Δx, Δy and Δz go to zero gives the x-component of the equation of motion

$$\begin{aligned}\frac{\partial \rho u_x}{\partial t} &= -\left(\frac{\partial}{\partial x}\rho u_x u_x + \frac{\partial}{\partial y}\rho u_y u_x + \frac{\partial}{\partial z}\rho u_z u_x\right) \\ &\quad -\left(\frac{\partial}{\partial x}\tau_{xx} + \frac{\partial}{\partial y}\tau_{yx} + \frac{\partial}{\partial z}\tau_{zx}\right) - \frac{\partial p}{\partial x} + \rho g_x.\end{aligned} \tag{39}$$

The y- and z-components may be obtained similarly as

$$\begin{aligned}\frac{\partial \rho u_y}{\partial t} &= -\left(\frac{\partial}{\partial x}\rho u_x u_y + \frac{\partial}{\partial y}\rho u_y u_y + \frac{\partial}{\partial z}\rho u_z u_y\right) \\ &\quad -\left(\frac{\partial}{\partial x}\tau_{xy} + \frac{\partial}{\partial y}\tau_{yy} + \frac{\partial}{\partial z}\tau_{zy}\right) - \frac{\partial p}{\partial y} + \rho g_y.\end{aligned} \tag{40}$$

$$\begin{aligned}\frac{\partial \rho u_z}{\partial t} &= -\left(\frac{\partial}{\partial x}\rho u_x u_z + \frac{\partial}{\partial y}\rho u_y u_z + \frac{\partial}{\partial z}\rho u_z u_z\right) \\ &\quad -\left(\frac{\partial}{\partial x}\tau_{xz} + \frac{\partial}{\partial y}\tau_{yz} + \frac{\partial}{\partial z}\tau_{zz}\right) - \frac{\partial p}{\partial z} + \rho g_z.\end{aligned} \tag{41}$$

We may also re-write all three equations in vector form as

$$\frac{\partial}{\partial t}(\rho \boldsymbol{u}) = -\boldsymbol{\nabla\cdot}(\rho \boldsymbol{u}\boldsymbol{u}) - \boldsymbol{\nabla} p - \boldsymbol{\nabla}\cdot\boldsymbol{\tau} + \rho \mathbf{g}. \tag{42}$$

Here $\rho\boldsymbol{u}$ is the mass velocity vector, $\mathbf{g}$ is the vector of gravitational acceleration, $\boldsymbol{\nabla} p$ is the gradient of pressure vector, and τ is the *stress tensor*, which has nine components. $\boldsymbol{\nabla}\cdot(\rho\boldsymbol{u}\boldsymbol{u})$ and $\boldsymbol{\nabla}\cdot\boldsymbol{\tau}$ are not a simple divergence because of the tensorial nature of $\rho\boldsymbol{u}\boldsymbol{u}$ and $\boldsymbol{\tau}$. Physically $\boldsymbol{\nabla\cdot}(\rho\boldsymbol{u}\boldsymbol{u})$ represents the rate of loss of momentum per unit volume by the fluid flow. Lets expand Equation (39)

$$\begin{aligned}\rho\frac{\partial u_x}{\partial t} + u_x\frac{\partial \rho}{\partial t} &= -u_x\left(\frac{\partial}{\partial x}\rho u_x + \frac{\partial}{\partial y}\rho u_y + \frac{\partial}{\partial z}\rho u_z\right) \\ &\quad -\left(\rho u_x\frac{\partial}{\partial x}u_x + \rho u_y\frac{\partial}{\partial y}u_x + \rho u_z\frac{\partial}{\partial z}u_x\right) \\ &\quad -\left(\frac{\partial}{\partial x}\tau_{xx} + \frac{\partial}{\partial y}\tau_{yx} + \frac{\partial}{\partial z}\tau_{zx}\right) - \frac{\partial p}{\partial x} + \rho g_x.\end{aligned} \tag{43}$$

Note that the terms

$$u_x\frac{\partial \rho}{\partial t} = -u_x\left(\frac{\partial}{\partial x}\rho u_x + \frac{\partial}{\partial y}\rho u_y + \frac{\partial}{\partial z}\rho u_z\right) \tag{44}$$

represent the *continuity equation* multiplied u_x. Therefore,

$$\begin{aligned}\rho\frac{\partial u_x}{\partial t} &= -\left(\rho u_x\frac{\partial}{\partial x}u_x + \rho u_y\frac{\partial}{\partial y}u_x + \rho u_z\frac{\partial}{\partial z}u_x\right) \\ &\quad -\left(\frac{\partial}{\partial x}\tau_{xx} + \frac{\partial}{\partial y}\tau_{yx} + \frac{\partial}{\partial z}\tau_{zx}\right) - \frac{\partial p}{\partial x} + \rho g_x.\end{aligned} \tag{45}$$

Furthermore, note that

$$\rho\frac{Du_x}{Dt} = \rho\frac{\partial u_x}{\partial t} + \rho u_x\frac{\partial}{\partial x}u_x + \rho u_y\frac{\partial}{\partial y}u_x + \rho u_z\frac{\partial}{\partial z}u_x, \tag{46}$$

so that

$$\rho\frac{Du_x}{Dt} = -\left(\frac{\partial}{\partial x}\tau_{xx} + \frac{\partial}{\partial y}\tau_{yx} + \frac{\partial}{\partial z}\tau_{zx}\right) - \frac{\partial p}{\partial x} + \rho g_x, \tag{47}$$

and equivalently,

$$\rho\frac{Du_y}{Dt} = -\left(\frac{\partial}{\partial x}\tau_{xy} + \frac{\partial}{\partial y}\tau_{yy} + \frac{\partial}{\partial z}\tau_{zy}\right) - \frac{\partial p}{\partial y} + \rho g_y, \tag{48}$$

as well as

$$\rho\frac{Du_z}{Dt} = -\left(\frac{\partial}{\partial x}\tau_{xz} + \frac{\partial}{\partial y}\tau_{yz} + \frac{\partial}{\partial z}\tau_{zz}\right) - \frac{\partial p}{\partial z} + \rho g_z, \tag{49}$$

or in three-dimensions

$$\rho\frac{D\boldsymbol{u}}{Dt} = -\boldsymbol{\nabla}p - \boldsymbol{\nabla}\cdot\boldsymbol{\tau} + \rho\mathbf{g}. \tag{50}$$

This form of the equation of motion states that a small volume element moving with the fluid flow is accelerated because fo the forces acting upon it. In other words, Newtons second law in the form *mass* $\times$ *acceleration = sum of forces*. In order to avoid the lengthy derivation of the components of the stress tensor τ, they will be provided below without further ado

$$\tau_{xx} = -2\mu\frac{\partial u_x}{\partial x} + \left(\frac{2}{3}\mu - \kappa\right)(\nabla\cdot\mathbf{u}) \tag{51}$$

$$\tau_{yy} = -2\mu\frac{\partial u_y}{\partial y} + \left(\frac{2}{3}\mu - \kappa\right)(\nabla\cdot\mathbf{u}) \tag{52}$$

$$\tau_{zz} = -2\mu\frac{\partial u_z}{\partial z} + \left(\frac{2}{3}\mu - \kappa\right)(\nabla\cdot\mathbf{u}) \tag{53}$$

$$\tau_{xy} = \tau_{yx} = -\mu\left(\frac{\partial u_x}{\partial y} + \frac{\partial u_y}{\partial x}\right) \tag{54}$$

$$\tau_{yz} = \tau_{zy} = -\mu\left(\frac{\partial u_y}{\partial z} + \frac{\partial u_z}{\partial y}\right) \tag{55}$$

$$\tau_{zx} = \tau_{xz} = -\mu\left(\frac{\partial u_z}{\partial x} + \frac{\partial u_x}{\partial z}\right). \tag{56}$$

The equation of motion in cylindrical coordinates, assuming cylindrical symmetry (i.e., $\partial/\partial\theta = 0$ and $u_\theta = 0$, are

$$\rho\frac{Du_r}{Dt} = \rho\left(\frac{\partial u_r}{\partial t} + u_r\frac{\partial u_r}{\partial r} + u_z\frac{\partial u_r}{\partial z}\right) = -\left(\frac{1}{r}\frac{\partial}{\partial r}(r\tau_{rr}) + \frac{\partial}{\partial z}\tau_{rz}\right) - \frac{\partial p}{\partial r} + \rho g_r, \tag{57}$$

and

$$\rho\frac{Du_z}{Dt} = \rho\left(\frac{\partial u_z}{\partial t} + u_r\frac{\partial u_z}{\partial r} + u_z\frac{\partial u_z}{\partial z}\right) = -\left(\frac{1}{r}\frac{\partial}{\partial r}(r\tau_{rz}) + \frac{\partial}{\partial z}\tau_{zz}\right) - \frac{\partial p}{\partial z} + \rho g_z. \tag{58}$$

The corresponding terms of the stress tensor are

$$\tau_{rr} = -2\mu\frac{\partial u_r}{\partial r} + \left(\frac{2}{3}\mu - \kappa\right)(\nabla\cdot\mathbf{u}) \tag{59}$$

$$\tau_{zz} = -2\mu\frac{\partial u_z}{\partial z} + \left(\frac{2}{3}\mu - \kappa\right)(\nabla\cdot\mathbf{u}) \tag{60}$$

$$\tau_{rz} = \tau_{zr} = -\mu\left(\frac{\partial u_z}{\partial r} + \frac{\partial u_r}{\partial z}\right), \tag{61}$$

where

$$(\boldsymbol{\nabla}\cdot\boldsymbol{u}) = \frac{1}{r}\frac{\partial}{\partial r}(ru_r) + \frac{\partial u_z}{\partial z}. \tag{62}$$

Here κ is the *bulk viscosity*, which is most of the time neglected. Furthermore, for an incompressible fluid ($\nabla\cdot\mathbf{u} = 0$). If in addition μ is constant, then these equations simplify to

$$\rho\frac{D\boldsymbol{u}}{Dt} = -\boldsymbol{\nabla}p + \mu\boldsymbol{\nabla}^2\boldsymbol{u} + \rho\mathbf{g}, \tag{63}$$

known as the *Navier Stokes Equations*.

5.2. Non-Newtonian viscosity

Newton's law of viscosity is given by

$$\tau_{ij} = -\mu\left(\frac{\partial u_j}{\partial x_i} + \frac{\partial u_i}{\partial x_j}\right) + \left(\frac{2}{3}\mu - \kappa\right)\left(\frac{\partial u_x}{\partial x} + \frac{\partial u_y}{\partial y}\frac{\partial u_z}{\partial z}\right)\delta_{ij} \tag{64}$$

or in vector notation

$$\boldsymbol{\tau} = -\mu\left(\boldsymbol{\nabla u} + (\boldsymbol{\nabla u})^{\mathrm{t}}\right) + \left(\frac{2}{3}\mu - \kappa\right)(\boldsymbol{\nabla}\cdot\boldsymbol{u})\,. \tag{65}$$

In this formulation μ may be dependent on pressure or temperature. In the case of viscosities that also depend on the deformation rate - but not normal stresses, time-dependent effects, or elastic effects - then the Newtonian fluid model can be *generalized* by simply replacing the constant viscosity μ by the non-Newtonian viscosity η, a function of the shear rate, $\dot{\gamma} = \sqrt{(\dot{\boldsymbol{\gamma}} : \dot{\boldsymbol{\gamma}})/2}$, where $\dot{\boldsymbol{\gamma}} = \boldsymbol{\nabla u} + (\boldsymbol{\nabla u})^{\mathrm{t}}$. The *generalized Newtonian fluid model* is therefore

$$\boldsymbol{\tau} = -\eta\left(\boldsymbol{\nabla u} + (\boldsymbol{\nabla u})^{\mathrm{t}}\right) \equiv -\eta\,\dot{\boldsymbol{\gamma}} \qquad \text{with} \qquad \eta = \eta(\dot{\gamma}). \tag{66}$$

A common empirical formulation for η is the power law expression

$$\eta = m\dot{\gamma}^{n-1}. \tag{67}$$

5.3. Stokes flow

The Navier Stokes equations, with the dynamic viscosity $\nu = \mu/\rho$, is given by

$$\frac{D\mathbf{u}}{Dt} = -\frac{1}{\rho}\nabla p + \nu\nabla^2\mathbf{u}, \tag{68}$$

where for illustrative purpose we have neglected the body force term due to gravity. To non-dimensionalize we define the following characteristic scales

$$\begin{aligned} U &\quad \text{for velocity} \\ L &\quad \text{for the general distance over which} \mathbf{U} \text{varies} \\ L/U &\quad \text{for time} \\ \nu\rho U/L &\quad \text{for pressure} \end{aligned} \tag{69}$$

Thus

$$\frac{U^2}{L}\frac{D\hat{\mathbf{u}}}{D\hat{t}} = -\frac{\nu U}{L^2}\hat{\nabla}\hat{P} + \frac{\nu U}{L^2}\hat{\nabla}^2\hat{\mathbf{u}}, \tag{70}$$

where $\hat{}$ denotes a dimensionless quantity. Dividing by $\nu U/L^2$ we obtain

$$\mathrm{Re}\frac{D\hat{\mathbf{u}}}{D\hat{t}} = -\hat{\nabla}\hat{P} + \hat{\nabla}^2\hat{\mathbf{u}}, \tag{71}$$

where Re denotes the Reynolds number, which can alternatively be derived form a balance of inertia forces to viscous forces. For $\mathrm{Re} \ll 1$ we find

$$\hat{\nabla}\hat{P} = \hat{\nabla}^2\hat{\mathbf{u}}. \tag{72}$$

This equation is called the *Stokes equation*. It has profound implications. For low Reynolds number flows the velocity anywhere within the domain of interest instantaneously adjusts to changes in body forces or boundary conditions. This is the meaning of *inertial forces are negligible*.

6. Energy balance (first law of thermodynamics)

6.1. Energy flux

This derivation follows closely that of Bird et al. (2002). Consider three mutually perpendicular planes, dS_x, dS_y and dS_z upon which forces are acting and across which kinetic and internal energy are advected. The change in energy for a unit volume bound by surfaces dS_i is equal to the difference in energy advected

into and out of the volume, plus heat added to the volume and work done on the volume. We shall define the *kinetic energy per unit volume* as

$$\tfrac{1}{2}\rho u^2 = \tfrac{1}{2}\rho(\mathbf{u}\cdot\mathbf{u}) = \tfrac{1}{2}\rho\left(u_x^2+u_y^2+u_z^2\right), \tag{73}$$

which is the energy associated with the observable motion of the fluid continuum, whereas the *internal energy per unit volume* is given by

$$\rho U_e, \tag{74}$$

with *internal energy*, U_e, defined as the kinetic energies of the constituent molecules calculated in the frame moving with the velocity $\mathbf{u}$, plus the energies associated with the vibrational and rotational motions of the molecules as well as the energies of interaction among all the molecules. It is assumed that the internal energy for a flowing fluid is the same function of temperature and density as for a fluid at equilibrium. Therefore, the rate at which energy is advected across a surface area of size dS_x, oriented perpendicular to the x-axis, is given by

$$\left(\tfrac{1}{2}\rho u^2+\rho U_e\right)u_x dS_x. \tag{75}$$

The energy advected across three mutually perpendicular surfaces, dS_x, dS_y and dS_z, all of equal size dS, divided by the area dS is called the *convective energy flux vector*

$$\left(\tfrac{1}{2}\rho u^2+\rho U_e\right)\delta_{\mathbf{x}}u_x+\left(\tfrac{1}{2}\rho u^2+\rho U_e\right)\delta_{\mathbf{y}}u_y+\left(\tfrac{1}{2}\rho u^2+\rho U_e\right)\delta_{\mathbf{z}}u_z=\left(\tfrac{1}{2}\rho u^2+\rho U_e\right)\mathbf{u} \tag{76}$$

The rate of work done by molecular motion per unit volume equals the product of forces times velocity on each of the planes bounding the unit volume. The force exerted on each surface defined as

$$\boldsymbol{\pi} = p\boldsymbol{\delta}+\boldsymbol{\tau}, \tag{77}$$

where the first term on the right hand side represents pressure work and the second term represents work due to shear stresses. Furthermore, $\boldsymbol{\pi}_x=[\pi_{xx}+\pi_{xy}+\pi_{xz}]$, $\boldsymbol{\pi}_y=[\pi_{yx}+\pi_{yy}+\pi_{yz}]$, and $\boldsymbol{\pi}_z=[\pi_{zx}+\pi_{zy}+\pi_{zz}]$. Since the fluid is moving with velocity $\mathbf{u}$, the rate at which work is done on each face is $(\boldsymbol{\pi}_i\cdot\mathbf{u})dS_i$. Therefore, the rate of work per unit area equals

$$[\boldsymbol{\pi}\cdot\mathbf{u}] = \boldsymbol{\delta}_x(\boldsymbol{\pi}_x\cdot\mathbf{u})+\boldsymbol{\delta}_y(\boldsymbol{\pi}_y\cdot\mathbf{u})+\boldsymbol{\delta}_z(\boldsymbol{\pi}_z\cdot\mathbf{u}) = p\mathbf{u}+[\boldsymbol{\tau}\cdot\mathbf{u}]. \tag{78}$$

Lastly, we have the rate of heat transport per unit area, $\mathbf{q}$. Combining these terms gives the *combined energy flux vector*

$$\mathbf{e}=\left(\tfrac{1}{2}\rho u^2+\rho U_e\right)\mathbf{u}+[\boldsymbol{\pi}\cdot\mathbf{u}]+\mathbf{q}=\left(\tfrac{1}{2}\rho u^2+\rho U_e\right)\mathbf{u}+p\mathbf{u}+[\boldsymbol{\tau}\cdot\mathbf{u}]+\mathbf{q}=\left(\tfrac{1}{2}\rho u^2+\rho h\right)\mathbf{u}+[\boldsymbol{\tau}\cdot\mathbf{u}]+\mathbf{q}, \tag{79}$$

where the *enthalpy*, h, is defined as

$$\rho h = \rho\left(U_e+\frac{p}{\rho}\right). \tag{80}$$

6.2. Conservation of energy

6.2.1. In general. For a *stationary* volume element $\Delta x\Delta y\Delta z$ through which fluid is flowing the momentum balance is given by

$$\left\{\begin{array}{c}\text{rate of increase in}\\ \text{kinetic and internal}\\ \text{energy}\end{array}\right\} = \left\{\begin{array}{c}\text{net rate of kinetic}\\ \text{and internal energy}\\ \text{by advective transport}\end{array}\right\}+\left\{\begin{array}{c}\text{net rate of}\\ \text{heat addition}\\ \text{by conduction}\end{array}\right\} \tag{81}$$
$$+\left\{\begin{array}{c}\text{rate of work by}\\ \text{molecular mechanisms}\\ \text{(i.e., stresses)}\end{array}\right\}+\left\{\begin{array}{c}\text{rate of work by}\\ \text{external forces}\\ \text{(e.g., gravity)}\end{array}\right\}.$$

Each individual term in the momentum balance is given by the following. For the rate of change

$$\Delta x\Delta y\Delta z\frac{\partial}{\partial t}\left(\tfrac{1}{2}\rho u^2+\rho U_e\right).$$

For the rate of advective transport

$$\begin{aligned} & \Delta y\Delta z\left\{\left[u_x\left(\tfrac{1}{2}\rho u^2+\rho U_e\right)\right]_x-\left[u_x\left(\tfrac{1}{2}\rho u^2+\rho U_e\right)\right]_{x+\Delta x}\right\} \\ + \quad & \Delta x\Delta z\left\{\left[u_y\left(\tfrac{1}{2}\rho u^2+\rho U_e\right)\right]_y-\left[u_y\left(\tfrac{1}{2}\rho u^2+\rho U_e\right)\right]_{y+\Delta y}\right\} \\ + \quad & \Delta x\Delta y\left\{\left[u_z\left(\tfrac{1}{2}\rho u^2+\rho U_e\right)\right]_z-\left[u_z\left(\tfrac{1}{2}\rho u^2+\rho U_e\right)\right]_{z+\Delta z}\right\}. \end{aligned}$$

For conduction

$$\begin{aligned} & \Delta y\Delta z\left\{[q_x]_x-[q_x]_{x+\Delta x}\right\} \\ + \quad & \Delta x\Delta z\left\{[q_y]_y-[q_y]_{y+\Delta y}\right\} \\ + \quad & \Delta x\Delta y\left\{[q_z]_z-[q_z]_{z+\Delta z}\right\}. \end{aligned}$$

For the rate of work against static pressure, p,

$$\begin{aligned} - \quad & \Delta y\Delta z\left\{[pu_x]_x-[pu_x]_{x+\Delta x}\right\} \\ - \quad & \Delta x\Delta z\left\{[pu_y]_y-[pu_y]_{y+\Delta y}\right\} \\ - \quad & \Delta x\Delta y\left\{[pu_z]_z-[pu_z]_{z+\Delta z}\right\}. \end{aligned}$$

For the rate of work against viscous forces

$$\begin{aligned} - \quad & \Delta y\Delta z\left\{[\tau_{xx}u_x+\tau_{xy}u_y+\tau_{xz}u_z]_x-[\tau_{xx}u_x+\tau_{xy}u_y+\tau_{xz}u_z]_{x+\Delta x}\right\} \\ - \quad & \Delta x\Delta z\left\{[\tau_{yx}u_x+\tau_{yy}u_y+\tau_{yz}u_z]_y-[\tau_{yx}u_x+\tau_{yy}u_y+\tau_{yz}u_z]_{y+\Delta y}\right\} \\ - \quad & \Delta x\Delta y\left\{[\tau_{zx}u_x+\tau_{zy}u_y+\tau_{zz}u_z]_z-[\tau_{zx}u_x+\tau_{zy}u_y+\tau_{zz}u_z]_{z+\Delta z}\right\}. \end{aligned}$$

For the rate of work against gravity

$$-\rho\Delta x\Delta y\Delta z\left(u_xg_x+u_yg_y+u_zg_z\right).$$

Using the conventional conservation approach for a representative elemental volume where $\Delta x\to 0$, $\Delta y\to 0$, and $\Delta z\to 0$ we obtain

$$\begin{aligned} \underbrace{\frac{\partial}{\partial t}\left(\tfrac{1}{2}\rho u^2+\rho U_e\right)}_{\text{rate of change}} = & -\underbrace{\left\{\frac{\partial}{\partial x}u_x\left(\tfrac{1}{2}\rho u^2+\rho U_e\right)+\frac{\partial}{\partial y}u_y\left(\tfrac{1}{2}\rho u^2+\rho U_e\right)+\frac{\partial}{\partial z}u_z\left(\tfrac{1}{2}\rho u^2+\rho U_e\right)\right\}}_{\text{advection}} \\ & -\underbrace{\left(\frac{\partial q_x}{\partial x}+\frac{\partial q_y}{\partial y}+\frac{\partial q_z}{\partial z}\right)}_{\text{conduction}}-\underbrace{\left(\frac{\partial}{\partial x}pu_x+\frac{\partial}{\partial y}pu_y+\frac{\partial}{\partial z}pu_z\right)}_{\text{pressure forces}} \\ & -\underbrace{\left\{\frac{\partial}{\partial x}\left(\tau_{xx}u_x+\tau_{xy}u_y+\tau_{xz}u_z\right)+\frac{\partial}{\partial y}\left(\tau_{yx}u_x+\tau_{yy}u_y+\tau_{yz}u_z\right)+\frac{\partial}{\partial z}\left(\tau_{zx}u_x+\tau_{zy}u_y+\tau_{zz}u_z\right)\right\}}_{\text{viscous forces}} \\ & +\underbrace{-\rho\left(u_xg_x+u_yg_y+u_zg_z\right)}_{\text{gravity}}, \end{aligned} \tag{82}$$

or equivalently

$$\begin{aligned} \underbrace{\rho\frac{\partial}{\partial t}\left(\tfrac{1}{2}u^2+U_e\right)}_{\text{rate of change}} = & -\underbrace{\boldsymbol{\nabla}\cdot\rho\boldsymbol{u}\left(\tfrac{1}{2}u^2+U_e\right)}_{\text{advection}}-\underbrace{\boldsymbol{\nabla}\cdot\mathbf{q}}_{\text{conduction}} \\ & -\underbrace{\left(\boldsymbol{\nabla}\cdot p\boldsymbol{u}\right)}_{\text{pressure forces}}-\underbrace{\left(\boldsymbol{\nabla}\cdot[\boldsymbol{\tau}\cdot\boldsymbol{u}]\right)}_{\text{viscous forces}}+\underbrace{\rho\left(\boldsymbol{u}\cdot\mathbf{g}\right)}_{\text{gravity}}. \end{aligned} \tag{83}$$

6.2.2. Steady state in one dimension without conductive heat loss/addition and no viscous heating.

$$\begin{aligned}\frac{\partial}{\partial t}\rho\left(\tfrac{1}{2}u^2+U_e\right)+\boldsymbol{\nabla}\cdot\rho\boldsymbol{u}\left(\tfrac{1}{2}u^2+U_e\right)\;=\\ -\boldsymbol{\nabla}\cdot\mathbf{q}-(\boldsymbol{\nabla}\cdot p\boldsymbol{u})-(\boldsymbol{\nabla}\cdot[\boldsymbol{\tau}\cdot\boldsymbol{u}])+\rho\left(\boldsymbol{u}\cdot\mathbf{g}\right).\end{aligned} \tag{84}$$

Expanding the left hand side gives

$$\begin{aligned}\rho\left[\frac{\partial}{\partial t}\left(\tfrac{1}{2}u^2+U_e\right)+\boldsymbol{u}\cdot\boldsymbol{\nabla}\left(\tfrac{1}{2}u^2+U_e\right)\right]+\left(\tfrac{1}{2}\rho u^2+\rho U_e\right)\left[\frac{\partial\rho}{\partial t}+(\boldsymbol{\nabla}\cdot\rho\boldsymbol{u})\right]=\\ -\boldsymbol{\nabla}\cdot\mathbf{q}-(\boldsymbol{\nabla}\cdot p\boldsymbol{u})-(\boldsymbol{\nabla}\cdot[\boldsymbol{\tau}\cdot\boldsymbol{u}])+\rho\left(\boldsymbol{u}\cdot\mathbf{g}\right).\end{aligned} \tag{85}$$

Here, the second term on the right hand side is the continuity equation and is equal to zero, therefore,

$$\rho\left[\frac{\partial}{\partial t}\left(\tfrac{1}{2}u^2+U_e\right)+\boldsymbol{u}\cdot\boldsymbol{\nabla}\left(\tfrac{1}{2}u^2+U_e\right)\right]=-\boldsymbol{\nabla}\cdot\mathbf{q}-(\boldsymbol{\nabla}\cdot p\boldsymbol{u})-(\boldsymbol{\nabla}\cdot[\boldsymbol{\tau}\cdot\boldsymbol{u}])+\rho\left(\boldsymbol{u}\cdot\mathbf{g}\right). \tag{86}$$

Assuming steady state and neglecting conductive heat transport and energy addition due to viscous dissipation, gives

$$\rho\boldsymbol{u}\cdot\boldsymbol{\nabla}\left(\tfrac{1}{2}u^2+U_e\right)=-\left(\boldsymbol{\nabla}\cdot p\boldsymbol{u}\right)+\rho\left(\boldsymbol{u}\cdot\mathbf{g}\right) \tag{87}$$

and upon expansion

$$\rho\boldsymbol{u}\cdot\boldsymbol{\nabla}\left(\tfrac{1}{2}u^2+U_e\right)=-p\left(\boldsymbol{\nabla}\cdot\boldsymbol{u}\right)-\boldsymbol{u}\cdot\boldsymbol{\nabla}p+\rho\left(\boldsymbol{u}\cdot\mathbf{g}\right). \tag{88}$$

Using $U_e = h - p/\rho$ gives

$$\rho\boldsymbol{u}\cdot\boldsymbol{\nabla}\left(\tfrac{1}{2}u^2+h-(p/\rho)\right)=-p\left(\boldsymbol{\nabla}\cdot\boldsymbol{u}\right)-\boldsymbol{u}\cdot\boldsymbol{\nabla}p+\rho\left(\boldsymbol{u}\cdot\mathbf{g}\right) \tag{89}$$

or

$$\rho\boldsymbol{u}\cdot\boldsymbol{\nabla}\left(\tfrac{1}{2}u^2+h\right)+(p/\rho)\boldsymbol{u}\cdot\boldsymbol{\nabla}\rho=-p\left(\boldsymbol{\nabla}\cdot\boldsymbol{u}\right)+\rho\left(\boldsymbol{u}\cdot\mathbf{g}\right). \tag{90}$$

From steady-state continuity

$$\rho(\boldsymbol{\nabla}\cdot\boldsymbol{u})=-\boldsymbol{u}\cdot\boldsymbol{\nabla}\rho\quad\text{ or equivalently }\quad-p(\boldsymbol{\nabla}\cdot\boldsymbol{u})=(p/\rho)\boldsymbol{u}\cdot\boldsymbol{\nabla}\rho,$$

so that

$$\rho\boldsymbol{u}\cdot\boldsymbol{\nabla}\left(\tfrac{1}{2}u^2+h\right)=+\rho\left(\boldsymbol{u}\cdot\mathbf{g}\right) \tag{91}$$

or

$$\boldsymbol{\nabla}\left(\tfrac{1}{2}u^2+h\right)=\mathbf{g}. \tag{92}$$

In the case of a one-dimensional system oriented in the z-direction with $g_z = -g$, we have

$$u_z\frac{du_z}{dz}+\frac{dh}{dz}=-g \tag{93}$$

or equivalently

$$u_z du_z+dh+gdz=0, \tag{94}$$

which is the equation used in *Conflow* [Mastin and Ghiorso, 2000].

6.2.3. Steady state in one-dimensional cylindrical symmetry without conductive heat loss/addition and with viscous heating.

$$u_z\frac{du_z}{dz}+\frac{dh}{dz}=\frac{\partial}{\partial r}(\tau_{rz}u_z)+\frac{\partial}{\partial z}\left(\tau_{zz}u_z\right)-g. \tag{95}$$

Often the second term on the right hand side is neglected, whereas τ_{rz} cannot be calculated explicitly for a one-dimensional system. Instead τ_{rz} can be estimated by assuming a velocity profile based either Newtonian or non-Newtonian rheology.

6.2.4. Conservation of mechanical energy. The equation of mechanical energy can be obtained by forming the scalar product of the local velocity $\boldsymbol{u}$ with the equation of motion

$$\rho \frac{D}{Dt}\left(\tfrac{1}{2}u^2\right) = -\left(\boldsymbol{u}\cdot\boldsymbol{\nabla}p\right) - \left(\boldsymbol{u}\cdot\left[\boldsymbol{\nabla}\cdot\boldsymbol{\tau}\right]\right) + \rho\left(\boldsymbol{u}\cdot\mathbf{g}\right), \tag{96}$$

which describes the rate of change of kinetic energy per unit mass, $(\frac{1}{2}u^2)$. This equation can be expanded, together with making use of the continuity equation, to give

$$\begin{aligned}
\underbrace{\frac{\partial}{\partial t}\left(\tfrac{1}{2}\rho u^2\right)}_{\substack{\text{rate of increase}\\ \text{in kinetic energy}\\ \text{per unit volume}}} &= -\underbrace{\left(\boldsymbol{\nabla}\cdot\tfrac{1}{2}u^2\boldsymbol{u}\right)}_{\substack{\text{rate of input of}\\ \text{kinetic energy by}\\ \text{the bulk flow}}} \\
&- \underbrace{\left(\boldsymbol{\nabla}\cdot p\boldsymbol{u}\right)}_{\substack{\text{rate of work done by}\\ \text{pressure of surroundings}\\ \text{on volume element}}} + \underbrace{p\left(\boldsymbol{\nabla}\cdot\boldsymbol{u}\right)}_{\substack{\text{rate of } \textit{reversible}\\ \text{conversion to}\\ \text{internal energy}}} \\
&- \underbrace{\left(\boldsymbol{\nabla}\cdot\left[\boldsymbol{\tau}\cdot\boldsymbol{u}\right]\right)}_{\substack{\text{rate of work done by}\\ \text{viscous forces on}\\ \text{volume element}}} + \underbrace{\left(\boldsymbol{\tau}\!:\!\boldsymbol{\nabla}\boldsymbol{u}\right)}_{\substack{\text{rate of } \textit{irreversible}\\ \text{convesion to}\\ \text{internal energy}}} \\
&+ \underbrace{\rho\left(\boldsymbol{u}\cdot\mathbf{g}\right)}_{\substack{\text{rate of work done}\\ \text{by gravity force on}\\ \text{volume element}}}
\end{aligned} \tag{97}$$

where

$$\boldsymbol{\nabla}\cdot\tfrac{1}{2}u^2\boldsymbol{u} = \tfrac{1}{2}u^2\left(\boldsymbol{\nabla}\cdot\boldsymbol{u}\right) + \boldsymbol{\nabla}\left(\tfrac{1}{2}u^2\right)\cdot\boldsymbol{u}$$

and

$$\left(\boldsymbol{\tau}\!:\!\boldsymbol{\nabla}\boldsymbol{u}\right) = \left(\left[\boldsymbol{\tau}\cdot\boldsymbol{u}\right]\cdot\boldsymbol{u}\right) = -\mu\Phi = -\tfrac{1}{2}\mu\sum_i\sum_j\left[\left(\frac{\partial u_i}{\partial x_j}+\frac{\partial u_j}{\partial x_i}\right) - \tfrac{2}{3}\left(\boldsymbol{\nabla}\cdot\boldsymbol{u}\right)\delta_{ij}\right]^2$$

is the conversion of mechanical to thermal energy, also known as *viscous heating*.

6.2.5. Equation of energy in terms of fluid temperature. Subtracting Equation (97) from Equation (83) gives

$$\underbrace{\rho\frac{DU_e}{Dt}}_{\substack{\text{rate of gain}\\ \text{of internal}\\ \text{energy}\\ \text{per unit volume}}} = -\underbrace{\left(\boldsymbol{\nabla}\cdot\mathbf{q}\right)}_{\substack{\text{rate of internal}\\ \text{energy input}\\ \text{by conduction}\\ \text{per unit volume}}} - \underbrace{p\left(\boldsymbol{\nabla}\cdot\boldsymbol{u}\right)}_{\substack{\textit{irreversible} \text{ rate of}\\ \text{internal energy increase}\\ \text{per unit volume}\\ \text{by compression}}} - \underbrace{\left(\boldsymbol{\tau}\!:\!\boldsymbol{\nabla}\boldsymbol{u}\right)}_{\substack{\textit{irreversible} \text{ rate of}\\ \text{internal energy increase}\\ \text{per unit volume}\\ \text{by viscous dissipation}}} \tag{98}$$

Using the relation $U_e = h - p/\rho$, together with the equation of continuity, we obtain

$$\rho\frac{Dh}{Dt} = -\left(\boldsymbol{\nabla}\cdot\boldsymbol{q}\right) - \left(\boldsymbol{\tau}:\boldsymbol{\nabla}\boldsymbol{u}\right) + \frac{Dp}{Dt}. \tag{99}$$

For Newtonian fluids, where enthalpy is a function of p and T, we have from equilibrium thermodynamics

$$dh = \left(\frac{\partial h}{\partial T}\right)_p dT + \left(\frac{\partial h}{\partial p}\right)_T dp = C_p dT + \left[\hat{V} - T\left(\frac{\partial\hat{V}}{\partial T}\right)_p\right]dp, \tag{100}$$

where $\hat{V} = 1/\rho$ and C_p is the heat capacity at constant pressure per unit mass. Therefore,

$$\begin{aligned}
\rho\frac{Dh}{Dt} &= \rho C_p\frac{DT}{Dt} + \rho\left[\hat{V} - T\left(\frac{\partial\hat{V}}{\partial T}\right)_p\right]\frac{Dp}{Dt} \\
&= \rho C_p\frac{DT}{Dt} + \rho\left[\frac{1}{\rho} - T\left(\frac{\partial 1/\rho}{\partial T}\right)_p\right]\frac{Dp}{Dt} \\
&= \rho C_p\frac{DT}{Dt} + \left[1 + \left(\frac{\partial\ln(\rho)}{\partial\ln(T)}\right)_p\right]\frac{Dp}{Dt}.
\end{aligned} \tag{101}$$

Equating Equations (99) and (101) gives

$$\rho C_p \frac{DT}{Dt} = -\left(\boldsymbol{\nabla}\cdot\boldsymbol{q}\right) - \left(\boldsymbol{\tau}:\boldsymbol{\nabla}\boldsymbol{u}\right) - \left(\frac{\partial \ln(\rho)}{\partial \ln(T)}\right)_p \frac{Dp}{Dt}, \tag{102}$$

where the use of Fourier's law gives $(\boldsymbol{\nabla}\cdot\boldsymbol{q}) = (\boldsymbol{\nabla}\cdot k\boldsymbol{\nabla}T)$. For and ideal gas $\partial\ln(\rho)/\partial\ln(T) = -1$. Furthermore $C_p - C_v = R$ and using the equation of state $pM = \rho RT$, together with continuity gives,

$$\rho C_v \frac{DT}{Dt} = -\left(\boldsymbol{\nabla}\cdot\boldsymbol{q}\right) - \left(\boldsymbol{\tau}:\boldsymbol{\nabla}\boldsymbol{u}\right) - p\left(\boldsymbol{\nabla}\cdot\boldsymbol{u}\right), \tag{103}$$

where C_v is the heat capacity at constant volume and per unit mass. Lastly, for a fluid with constant density

$$\rho C_p \frac{DT}{Dt} = -\left(\boldsymbol{\nabla}\cdot\boldsymbol{q}\right) - \left(\boldsymbol{\tau}:\boldsymbol{\nabla}\boldsymbol{u}\right). \tag{104}$$

7. Some useful references

Bejan, A., *Convection Heat Transfer, Fourth Edition*, John Wiley & Sons, Inc., 2013. To learn about scaling analysis in heat transfer.

Bird, R. B., Stewart, W. E. and Lightfoot, E. N., *Transport Phenomena Second Edition*, John Wiley & Sons, Inc., 2002. To learn about mass and energy transport. (*The First Edition is also useful*)

Kundu, P. K. and Cohen, I. M., *Fluid Mechanics Third Edition*, Elsevier Academic Press, 2004. To learn about fluid mechanics.

Mastin, L. G. and Ghiorso, M. S., 2000, *A Numerical Program for Steady-State Flow of Magma-Gas Mixtures through Vertical Eruptive Conduits* USGS Open-File Report 00-209

CIDER 2019 Lecture Notes Appendix: Compressible Flow

Helge M. Gonnermann, *Earth, Environmental and Planetary Sciences, Rice University*

Contents

1. Steady adiabatic flow of frictionless ideal gas

THINGS TO REMEMBER

- Euler's equation: $u\,du + dp/\rho = 0$.
- Bernoulli's equation: $(\rho u^2)/2 + p = \text{constant}$.
- Enthalpy: $h \equiv e + pv$.
- Mach number: $M = u/c$, is velocity of the medium divided by its speed of sound.
- Incompressible flow: $M < 0.3$.
- Subsonic flow: $0.3 < M < 1$ somewhere in the flow.
- Transsonic flow: $0.8 < M < 1.2$.
- Supersonic flow: $1 < M < 3$.
- Hypersonic flow: $M > 3$
- For supersonic flow the relationship between velocity and conduit diameter is opposite that of incompressible flow.
- Adiabatic: energy does not enter or leave a system.
- Isentropic: adiabatic and frictionless.
- Flow work: pv, is required to push matter across a section within an adiabatic flow.
- Ratio of specific heats: $\gamma = C_p/C_v$.
- Speed of sound: $c = \sqrt{\gamma RT}$ (perfect gas).

1.1. Continuity equation

For steady flow of an ideal and frictionless gas in a conduit of variable cross sectional area, A, mass conservation dictates that

$$\rho_1 A_1 u_1 = \rho_2 A_2 u_2. \tag{1}$$

In other words, the mass flow rate is constant, or

$$\dot{m} = \rho A u = \text{constant}, \tag{2}$$

or in terms of the *continuity equation*

$$\frac{d}{dx}(\rho A u) = 0. \tag{3}$$

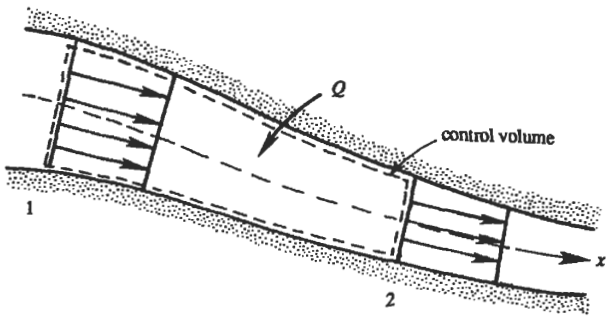

Figure 1

Control volume for a one-dimensional flow. Copied from Kundu & Cohen, *Fluid Mechanics*.

1.2. Euler's and Bernoulli's equations

Assuming a straight channel, so that the velocity vector reduces to a single component u in the x-direction, the conservation of linear momentum for an inviscid fluid with no body forces is given by *Euler's equation*

$$\frac{\partial u}{\partial t} + u\frac{\partial u}{\partial x} + \frac{1}{\rho}\frac{\partial p}{\partial x} = 0. \tag{4}$$

Assuming steady state gives

$$u\frac{du}{dx} + \frac{1}{\rho}\frac{dp}{dx} = u\,du + \frac{dp}{\rho} = 0, \tag{5}$$

and integration gives *Bernoulli's equation*

$$\frac{1}{2}\rho u^2 + p = \text{constant}. \tag{6}$$

1.3. Momentum equation

Multiplying Euler's equation (Eq. (5)) by ρA and the continuity equation (Eq. (3)) by u gives, respectively

$$\rho u A\frac{\partial u}{\partial x} = -A\frac{\partial p}{\partial x} \tag{7}$$

and

$$u\frac{\partial}{\partial x}(\rho A u) = 0. \tag{8}$$

Adding both equations gives the one-dimensional momentum equation

$$\rho u A\frac{\partial u}{\partial x} + u\frac{\partial}{\partial x}(\rho A u) = -A\frac{\partial p}{\partial x}, \tag{9}$$

Okay, now it gets tricky. Note that

$$u\frac{\partial}{\partial x}(\rho A u) = \rho u A\frac{\partial u}{\partial x} + A u^2\frac{\partial \rho}{\partial x} + \rho u^2\frac{\partial A}{\partial x}, \tag{10}$$

and that

$$\frac{\partial}{\partial x}\left(\rho A u^2\right) = 2u\rho A\frac{\partial u}{\partial x} + A u^2\frac{\partial \rho}{\partial x} + \rho u^2\frac{\partial A}{\partial x}. \tag{11}$$

Subtracting these two equations gives

$$\frac{\partial}{\partial x}\left(\rho A u^2\right) = u\rho A\frac{\partial u}{\partial x} + u\frac{\partial}{\partial x}(\rho A u) \tag{12}$$

Therefore we can write Equation (9) as

$$\frac{\partial}{\partial x}\left(\rho A u^2\right) = -A\frac{\partial p}{\partial x}. \tag{13}$$

Note that

$$\frac{\partial}{\partial x}(pA) = A\frac{\partial p}{\partial x} + p\frac{\partial A}{\partial x}. \tag{14}$$

Therefore the one-dimensional momentum equation becomes

$$\frac{\partial}{\partial x}\left(\rho A u^2\right) = -\frac{\partial}{\partial x}(pA) + p\frac{\partial A}{\partial x}. \tag{15}$$

1.4. Speed of sound

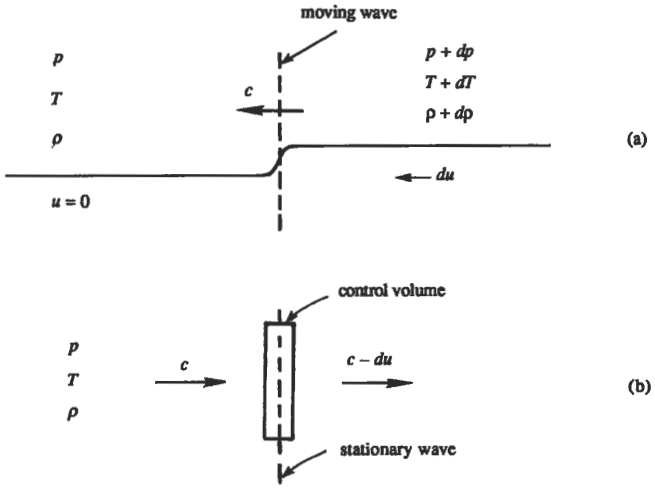

Figure 2

Propagation of a sound wave: (a) wave propagating into still fluid; and (b) stationary wave. Copied and modified from Kundu & Cohen, *Fluid Mechanics*, who reprinted from Liepmann & Roshko, *Elements of Gas Dynamics*.

A pressure pulse in an incompressible flow displaces all particles simultaneously and the pressure effect is instantaneous throughout the medium, as in a rigid body. A compressible fluid behaves similarly to an elastic solid. The displacement causes a local densification that propagates through the medium by displacing adjacent particles one after another. This pressure wave travels through the medium with a speed that is proportional to the rigidity of the medium. If the amplitude of the wave is infinitesimal it is called an acoustic wave, or equivalently, a sound wave. This scenario is depicted in Figure 2a. Imposing a velocity c directed opposite to the direction of the propagating sound wave, the wave becomes stationary, which is depicted in Figure 2b.

For the wave we find mass balance, which gives

$$A\rho c = A\,(\rho + d\rho)\,(c - du) \tag{16}$$

or

$$A\rho c = Ac\rho + Ac\,d\rho - A\rho\,du - A\,d\rho\,du. \tag{17}$$

Because the amplitude is small, we neglect second order terms and obtain

$$A\rho c = Ac\rho + Ac\,d\rho - A\rho\,du \tag{18}$$

or

$$du = c\,\frac{d\rho}{\rho}. \tag{19}$$

$du > 0$ thus requires that $d\rho > 0$, which means that the passage of the wave leaves behind a fluid that is moving in the direction of the wave, as shown in Figure 2a.

Momentum balance for the stationary wave is given by

$$(p + dp)A - pA + (A\rho c)(c - du) - (A\rho c)c = 0, \tag{20}$$

where viscous stresses have been neglected. Upon simplification one obtains

$$dp = \rho c\,du. \tag{21}$$

Substituting the expression for du obtained from mass balance (Equation (19)) gives

$$c^2 = \frac{dp}{d\rho}. \tag{22}$$

1.5. Area-velocity relation

The continuity equation (3) can be rewritten as

$$\frac{d}{dx}(\rho A u) = uA\frac{d\rho}{dx} + \rho u\frac{dA}{dx} + \rho A\frac{du}{dx} = 0, \tag{23}$$

or

$$\frac{d\rho}{\rho} + \frac{dA}{A} + \frac{du}{u} = 0. \tag{24}$$

For incompressible flow $d\rho = 0$, and velocity is inversely proportional to area. For compressible, adiabatic, nonviscous, nonconducting and isentropic flow Euler's equation (5) gives

$$u\,du = -\frac{dp}{\rho} = -\frac{dp}{d\rho}\frac{d\rho}{\rho} = -c^2\frac{d\rho}{\rho}, \tag{25}$$

where c is the *speed of sound*, given by

$$c^2 = \left(\frac{\partial p}{\partial \rho}\right)_s. \tag{26}$$

Introducing the *Mach number*,

$$M = u/c, \tag{27}$$

gives

$$\frac{d\rho}{\rho} = -M^2\frac{du}{u}. \tag{28}$$

Substituting this into equation (24) gives

$$\frac{dA}{A} + \left(1 - M^2\right)\frac{du}{u} = 0. \tag{29}$$

STEADY, FRICTIONLESS COMPRESSIBLE FLOW

Rearrangement of the above gives the following important relation for stead, frictionless compressible flow

$$\frac{1}{1-M^2}\frac{dA}{A} = -\frac{du}{u}, \tag{30}$$

which implies the following:

- At $M = 0$, that is incompressible flow, a change velocity and in area are inversely correlated.
- For $0 < M < 1$, that is subsonic speeds, the relation is qualitatively the same as incompressible flow, except the effect on velocity is relatively greater.
- At supersonic speeds an increase in u requires and increase in A.
- $M = 1$ can only be attained at a section of the conduit where $dA/A = 0$, which is called a *throat*.
- $M = 1$ is not a necessary condition at $dA/A = 0$, rather, $du = 0$ at a throat, implying that u attains a maximum (minimum) at the throat if the flow is subsonic (supersonic).
- Near $M = 1$ the flow is very sensitive to changes in A.

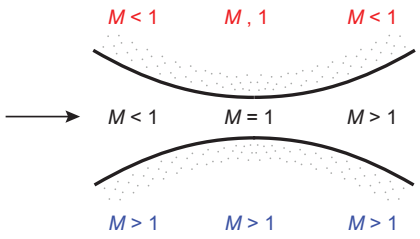

Figure 3

The three possible regimes for a convergeng-divergent nozzle.

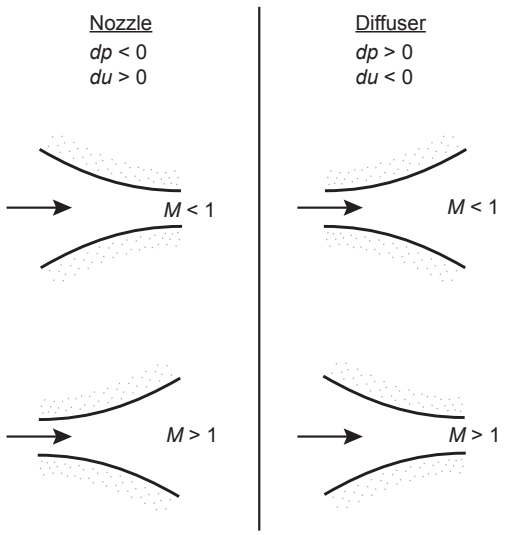

Figure 4

Shapes of nozzles and diffusers in subsonic and supersonic regimes.

1.6. Energy equation

The first law of thermodynamics states that the change in the internal energy of a closed system is equal to the amount of heat supplied to the system, minus the amount of work done by the system on its surroundings. For a control volume fixed in space it is given by

$$\underbrace{\frac{d}{dt}\int \rho\left(e+\frac{u^2}{2}\right)dV}_{\text{Change in stored energy}} + \underbrace{\int\left(e+\frac{u^2}{2}\right)\rho u_j dA_j}_{\text{energy flux out}} = \underbrace{\int u_i \tau_{ij} dA_j}_{\text{rate of work done on surface}} - \underbrace{\int \mathbf{q}\cdot d\mathbf{A}}_{\text{heat flux in}}, \tag{31}$$

where e is the internal energy per unit mass and $u^2/2$ is the kinetic energy per unit mass. $\mathbf{q}$ is the heat flux across surface area $\mathbf{A}$. The first term on the left-hand side represents the change of *stored energy*, which is the sum of internal and kinetic energies within the control volume. The second term on the left-hand side represents the flux of energy out of the control volume. The first term on the right-hand side represents the rate of work done on the control surface (i.e., shear stress due to *friction*). The second term on the right hand side represents heat input *through* the control *surface*.

Assuming steady state ($d/dt = 0$) and defining $\dot{m} = \rho_1 u_1 A_1 = \rho_2 u_2 A_2$ gives

$$\int\left(e+\frac{u^2}{2}\right)\rho u_j dA_j = \dot{m}\left[e_2 + \frac{1}{2}u_2^2 - e_1 - \frac{1}{2}u_1^2\right]. \tag{32}$$

Neglecting frictional stresses

$$\int u_i \tau_{ij} dA_j = u_1 p_1 A_1 - u_2 p_2 A_2. \tag{33}$$

Neglecting any external heat addition or loss (i.e., adiabatic), we obtain

$$e_2 + \frac{1}{2}u_2^2 - e_1 - \frac{1}{2}u_1^2 = \frac{1}{\dot{m}}\left[u_1 p_1 A_1 - u_2 p_2 A_2\right] \tag{34}$$

Defining the specific volume v, which has units of m^3/kg gives

$$\frac{uA}{\dot{m}} = v \tag{35}$$

and

$$e_2 + \frac{1}{2}u_2^2 - e_1 - \frac{1}{2}u_1^2 = p_1 v_1 - p_2 v_2. \tag{36}$$

Here $p_1 v_1$ is the work done (per unit mass) by the surroundings in pushing fluid into the control volume. Similarly, $p_2 v_2$ is the work done by the fluid inside the control volume on the surroundings by pushing fluid out of the control volume.

ENTHALPY AND CONSERVATION OF ENERGY

Defining enthalpy as

$$h \equiv e + pv, \tag{37}$$

gives for the conservation of energy (under aforementioned assumptions)

$$h_2 + \frac{1}{2}u_2^2 = h_1 + \frac{1}{2}u_1^2. \tag{38}$$

This equation states that the sum of enthalpy and kinetic energy remains constant in an adiabatic (no heat leaves or enters the system) flow. Relative to a *static* system, in a flowing system *flow work*, pv, is required to push matter across the surface of a control volume.

1.7. Thermodynamic relations

For a reversible process, the entropy change, dS is given by

$$TdS = dQ, \tag{39}$$

where Q is the heat added. Recalling that enthalpy is defined as

$$h \equiv e + pv, \tag{40}$$

Gibbs obtains for the change in entropy

$$TdS = de + pdv = dh - vdp. \tag{41}$$

Furthermore, the specific heat at constant pressure is defined as

$$C_p \equiv \left(\frac{\partial h}{\partial T}\right)_p, \tag{42}$$

whereas the specific heat at constant volume is defined as

$$C_v \equiv \left(\frac{\partial e}{\partial T}\right)_v. \tag{43}$$

and Isentropic flow of a perfect gas with constant specific heats obeys the relation

$$\underbrace{\frac{p}{\rho^\gamma} = \text{constant}}_{\text{(isentropic)}}. \tag{44}$$

USEFUL THERMODYNAMIC RELATIONS

For a perfect gas with constant specific heats

$$p = \rho RT, \tag{45}$$

where $R = 8314.36$ J mol^{-1} K^{-1} is the universal gas constant. The speed of sound is given by

$$c = \sqrt{\gamma RT}, \tag{46}$$

where the ratio of specific heats, γ, is defined as

$$\gamma = \frac{C_p}{C_v}. \tag{47}$$

For example, for air at ordinary temperatures, $\gamma \approx 1.4$ and $C_p \approx 1000$ J kg^{-1} K^{-1}. Furthermore,

$$e = C_v T, \tag{48}$$

$$h = C_p T, \tag{49}$$

$$C_p = \frac{\gamma R}{\gamma - 1}, \tag{50}$$

$$C_v = \frac{R}{\gamma - 1}, \tag{51}$$

and

$$R = C_p - C_v. \tag{52}$$

1.8. Effect of back pressure on exit plane pressure

RECALL THE FOLLOWING

Equation (25):

$$u\,du = -\frac{dp}{\rho}.$$

Equation (30):

$$\frac{dA}{A} + \left(1 - M^2\right)\frac{du}{u} = 0.$$

1.8.1. For $M_e < 1$.

- $p_e > p_b$: For p_e to equilibrate to p_b requires that $dp < 0$. The higher pressure of the jet will cause an expansion, that is $dA > 0$. Given Equation (30), this requires that $du < 0$. But according to Equation (25) this would mean that $dp > 0$, which contradicts the initial premise. Therefore, $p_e > p_b$ is not feasible if $M_e < 1$.
- $p_e < p_b$: For p_e to equilibrate to p_b requires that $dp > 0$. The higher pressure outside of the jet causes the jet to contract, that is $dA < 0$. Given Equation (30), this requires that $du > 0$. But according to Equation (25) this would mean that $dp < 0$, which contradicts the initial premise. Therefore, $p_e < p_b$ is not feasible if $M_e < 1$.

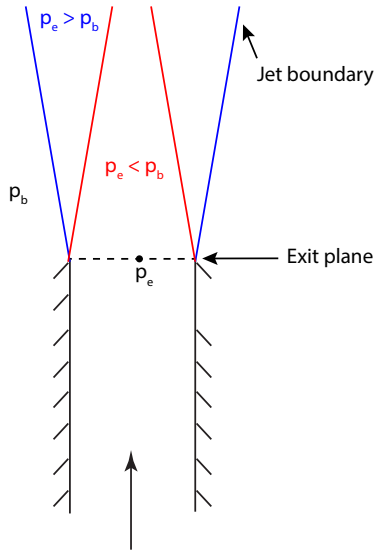

Figure 5

Discharge from a conduit into a large region of fixed back pressure, p_b. The case $p_e > p_b$ causes an expansion of the jet, because the pressure inside the jet is higher than for the surrounding fluid. The case $p_e < p_b$ causes a contraction of the jet, because of the higher pressure of the surrounding fluid.

1.8.2. For $M_e > 1$.

- $p_e > p_b$: For p_e to equilibrate to p_b requires that $dp < 0$. The higher pressure of the jet will cause an expansion, that is $dA > 0$. Given Equation (30), this requires that $du > 0$ and according to Equation (25) this would mean that indeed $dp < 0$.
- $p_e < p_b$: For p_e to equilibrate to p_b requires that $dp > 0$. The higher pressure outside of the jet causes the jet to contract, that is $dA < 0$. Given Equation (30), this requires that $du < 0$. But according to Equation (25) this would mean indeed that $dp > 0$.

1.8.3. For $M_e = 1$.

- In this case $dA = 0$ and $p_e = p_b$. This is referred to as **choked flow**.
- If $dA_e < 0$, then it is possible that $p_e > p_b$.

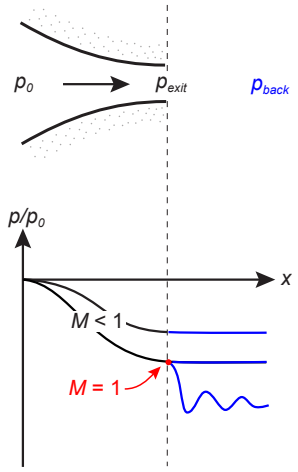

Figure 6

Pressure distribution along a convergent nozzle for different values of back pressure, p_{back}. Once $M = 1$ is reached at the exit lowering the back pressure will not increase the flow inside the nozzle, but instead result in an expansion wave outside the nozzle.

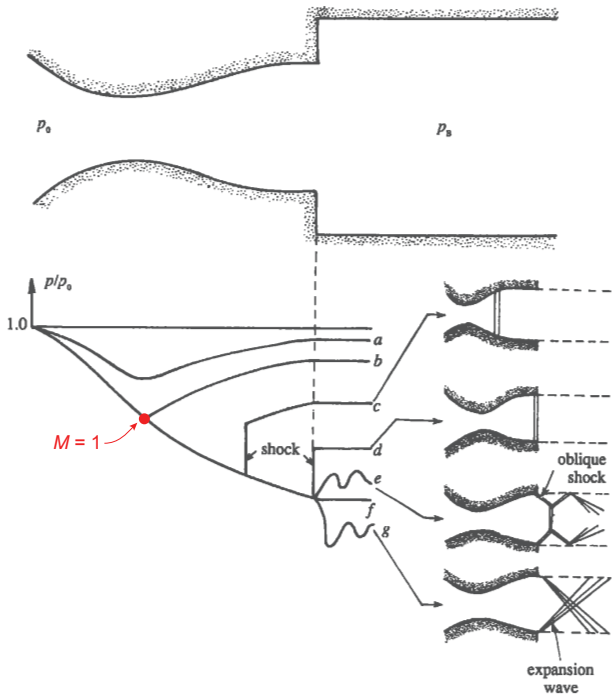

Figure 7

Pressure distribution along a divergent nozzle for different values of back pressure, p_B. Copied and modified from Kundu & Cohen, *Fluid Mechanics*, who reprinted from Liepmann & Roshko, *Elements of Gas Dynamics*.

2. Effect of friction in constant-area conduits

2.1. Derivations

Define the following: $M_{\text{upstream}} \equiv M_1$ and $M_{\text{downstream}} \equiv M_2$. Assuming steady state, the equations of mass, momentum and energy conservation are given by

$$p_1 u_1 = p_2 u_2 \tag{53}$$

$$p_1 + \rho_1 u_1^2 = p_2 + \rho_2 u_2^2 + p_1 f \tag{54}$$

$$h_1 + \frac{1}{2}u_1^2 + h_1 q = h_2 + \frac{1}{2}u_2^2, \tag{55}$$

where f is a dimensionless friction parameter and q is a dimensionless heating parameter. Assuming a perfect gas and using the relations $c = \sqrt{\gamma RT}$ and $M = u/c$ and $p = \rho RT$

$$\rho u^2 = p\gamma M^2. \tag{56}$$

Thus, writing the momentum equation in terms of M gives

$$p_1\left(1 + \gamma M_1^2 - f\right) = p_2\left(1 + \gamma M_2^2\right), \tag{57}$$

or

$$\frac{p_1}{p_2} = \frac{\left(1 + \gamma M_2^2\right)}{\left(1 + \gamma M_1^2 - f\right)}. \tag{58}$$

Furthermore, using the relations $c = \sqrt{\gamma RT}$ as well as $M = u/c$ with $p = \rho RT$ and $h = \gamma p/\rho(\gamma - 1)$ gives

$$u^2 = \gamma M^2 RT = \gamma M^2 p/\rho = h(\gamma - 1)M^2 \tag{59}$$

and thus

$$h_1\left(1 + \frac{\gamma - 1}{2}M_1^2 + q\right) = h_2\left(1 + \frac{\gamma - 1}{2}M_2^2\right), \tag{60}$$

or

$$\frac{h_1}{h_2} = \frac{1 + (\gamma - 1)M_2^2/2}{1 + (\gamma - 1)M_1^2/2 + q}. \tag{61}$$

Conservation of mass,

$$\frac{\rho_1}{\rho_2} = \frac{u_2}{u_1}, \tag{62}$$

together with the equation of state give

$$\frac{p_1 RT_2}{p_2 RT_1} = \frac{u_2}{u_1} \tag{63}$$

or

$$\frac{p_1}{p_2} = \frac{u_2}{u_1}\frac{\gamma RT_1}{\gamma RT_2} = \frac{u_2}{u_1}\frac{c_1^2}{c_2^2} = \frac{u_1}{u_2}\frac{M_2^2}{M_1^2}. \tag{64}$$

Using $h = \gamma p/\rho(\gamma - 1)$, together with conservation of mass gives

$$\frac{h_1}{h_2} = \frac{\rho_2 p_1}{\rho_1 p_2} = \frac{u_1 p_1}{u_2 p_2} \tag{65}$$

and substituting from the previous relation

$$\frac{h_1}{h_2} = \frac{\rho_2 p_1}{\rho_1 p_2} = \frac{u_1^2 M_2^2}{u_2^2 M_1^2} \tag{66}$$

or

$$\left[\frac{h_1}{h_2}\right]^{1/2} = \frac{u_1}{u_2}\frac{M_2}{M_1}. \tag{67}$$

Combining the expressions for h and p with our momentum and energy equations gives

$$\frac{u_1}{u_2} = \frac{M_1^2}{M_2^2}\frac{\left(1 + \gamma M_2^2\right)}{\left(1 + \gamma M_1^2 - f\right)} \tag{68}$$

and

$$\frac{u_1}{u_2} = \frac{M_1}{M_2}\left[\frac{1+(\gamma-1)M_2^2/2}{1+(\gamma-1)M_1^2/2+q}\right]^{1/2}. \tag{69}$$

Combining both equations gives

$$\frac{M_1^2}{M_2^2}\frac{\left(1+\gamma M_2^2\right)}{(1+\gamma M_1^2-f)} = \frac{M_1}{M_2}\left[\frac{1+(\gamma-1)M_2^2/2}{1+(\gamma-1)M_1^2/2+q}\right]^{1/2} \tag{70}$$

or

$$\frac{M_2}{M_1} = \left[\frac{\left(1+\gamma M_2^2\right)}{(1+\gamma M_1^2-f)}\right]\cdot\left[\frac{1+(\gamma-1)M_1^2/2+q}{1+(\gamma-1)M_2^2/2}\right]^{1/2}. \tag{71}$$

Bringing M_2 to the left-hand side and assuming q and f are specified, along with M_1, gives

$$\frac{M_2^2\left[1+(\gamma-1)M_2^2/2\right]}{\left(1+\gamma M_2^2\right)^2} = \frac{M_1^2\left[1+(\gamma-1)M_1^2/2+q\right]}{\left(1+\gamma M_1^2-f\right)^2} \equiv A \tag{72}$$

This is a biquadratic equation for M_2 with the solution

$$M_2^2 = \frac{-(1-2A\gamma)\pm\left[1-2A(\gamma+1)\right]^{1/2}}{(\gamma-1)-2A\gamma^2}, \tag{73}$$

which is plotted in Figure 8 for $q = 0$. For an equivalent figure in terms of q with $f = 0$, the reader is referred to Kundu & Cohen, *Fluid Mechanics*, or other texts dealing with compressible flow.

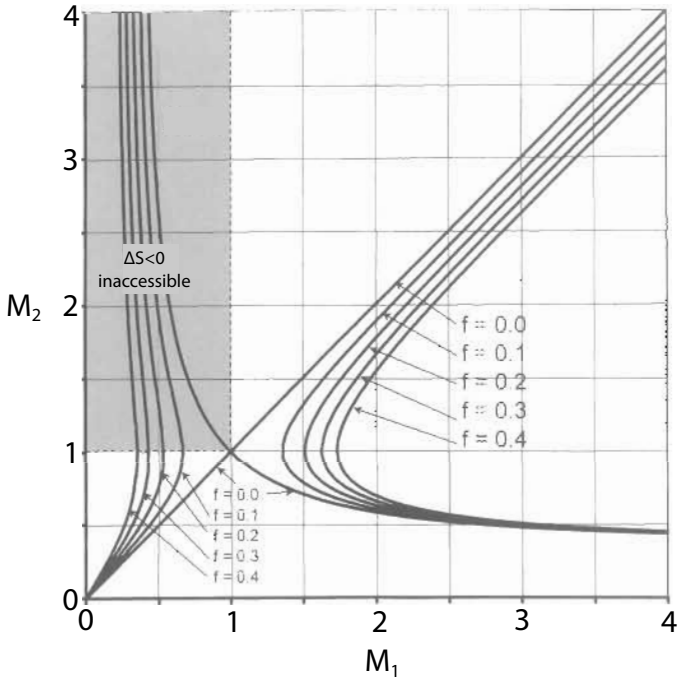

Figure 8

Flow in a constant-area duct with friction, f as parameter and $q = 0$. Upper left shaded quadrant is inaccessible because the change in entropy is < 1. Copied from Kundu & Cohen, *Fluid Mechanics*.

2.2. Implications: $M_1 < 1$

For $M_1 < 1$, friction requires that p decreases with x. As p decreases, so does ρ, which requires that u increases. Consequently, M increases as well.

Once subsonic always subsonic

It is not possible to go from $M_1 < 1$ to $M_2 > 1$, because it requires that entropy decreases.

2.3. Implications: $M_1 > 1$

For $M_1 > 1$ two solutions are possible: One for which $1 < M_2 < M_1$. In this case u decreases, whereas p and ρ increase downstream. The other solution is $M_2 < 1$. The two solutions coalesce when $M_2 = 1$, at which the flow is choked.

Supersonic to subsonic

- Pass from $M_1 > 1$ to $M_2 < 1$ via $M_2 = 1$.
- At $M_2 = 1$ the maximum mass flow rate is reached.

3. Conduit flow with magma compressibility

3.1. Governing equations

This section follows closely the approach outlined by Mastin (USGS OFR-00-209, 2000). Assuming one-dimensional steady flow in a vertical conduit, no heat loss/gain across the conduit walls and thermal equilibrium overall, and no gas loss through the conduit walls or upward within the magma, gives the following equations for mass, momentum and energy conservation, respectively,

$$\frac{d(\rho u A)}{dz} = 0, \tag{74}$$

$$\rho u \frac{du}{dz} = -\rho g - \rho u^2 \frac{f}{a} - \frac{dp}{dz}, \tag{75}$$

and

$$dh + u du + g dz = 0, \tag{76}$$

where ρ is magma density, u velocity, f the Fanning friction factor, a conduit radius, p pressure, g acceleration due to gravity, h enthalpy, and z the vertical coordinate.

FRICTION FACTOR

Recall that the Fanning friction factor, $f = f_\mathrm{F} = f_\mathrm{D}/4$, where f_D is the Darcy-Weissbach friction factor. For laminar flow $f_\mathrm{D} = 64/\mathrm{Re}$ and, hence, $f = 16/\mathrm{Re}$. At $\mathrm{Re} \gg 1000$ the friction factor will asymptotically approach a constant value, f_0, that can be calculated using existing formulas (e.g., Colebrook). A convenient approximation is to assume that $f = 16/Re + f_0$, where f_0 is obtained from the Mood Chart, which is a graph of f_D as a function of Re.

3.2. Pressure and velocity

Substituting the derivative of u from conservation of mass, that is

$$\frac{du}{dz} = -\frac{u}{A}\frac{dA}{dz} - \frac{u}{\rho}\frac{d\rho}{dz}, \tag{77}$$

into the momentum equation gives

$$-\frac{dp}{dz} = \rho g + \rho u^2 \frac{f}{a} - \frac{\rho u^2}{A}\frac{dA}{dz} - u^2 \frac{d\rho}{dz}. \tag{78}$$

Next approximate

$$\frac{d\rho}{dz} = \left(\frac{\partial \rho}{\partial p}\right)_S \frac{dp}{dz} = c^2 \frac{dp}{dz}, \tag{79}$$

where c is the speed of sound. Now substitute to obtain

$$-\frac{dp}{dz}\left(1-M^2\right)=\rho g+\rho u^2\frac{f}{a}-\frac{\rho u^2}{A}\frac{dA}{dz}, \tag{80}$$

or

$$-\frac{dp}{dz}=\left(\rho g+\rho u^2\frac{f}{a}-\frac{\rho u^2}{A}\frac{dA}{dz}\right)\left(1-M^2\right)^{-1}, \tag{81}$$

where $M=u/c$ is the Mach number. Equations (81) and (77) are integrated in terms of a constant mass discharge rate $Q_m=\rho uA$.

In most volcanically realistic cases $M<1$ at depth, but it may approach 1 as the magma reaches shallow depths and high gas fractions at low pressures. To avoid physically unrealistic solutions or singularities as $M\to 1$, the numerator in Equation (81) must approach zero, which leads to the following condition

$$\rho g+\rho u^2\frac{f}{a}=\frac{\rho u^2}{A}\frac{dA}{dz} \tag{82}$$

or

$$\frac{da}{dz}=\frac{1}{2}\left(\frac{ga}{u^2}+f\right). \tag{83}$$

Because the right-hand side of Equation (83) is always positive, the vent must be widening in the upward direction as $M\to 1$. The flow, if it does indeed approach $M=1$ at the vent is called *choked*. Typically, the exit pressure is greater than atmospheric and will equilibrate to atmospheric abruptly above the vent through a series of shock waves.

In a gradually widening conduit, it is possible that the fluid will accelerate to supersonic velocity and pressure can drop to lower than 1 atm before reaching the conduit exit. In this case a stationary shock wave will develop within the diverging section of the conduit and the velocity will drop abruptly to subsonic with pressure rising so that the mixture exits the conduit at 1 atm.

THE SPEED OF SOUND FOR A GAS-PYROCLAST MIXTURE

The speed of sound of a multiphase mixture (i.e., gas, liquid, solid) is given by

$$c^2=\frac{K}{\rho}, \tag{84}$$

where K is the bulk modulus. For a multiphase fluid consisting of gas, melt and crystals of volume fractions ϕ_g, ϕ_m and ϕ_x, respectively,

$$\frac{1}{K}=\frac{\phi_g}{K_g}+\frac{\phi_m}{K_m}+\frac{\phi_x}{K_x}. \tag{85}$$

For and ideal gas the isothermal and isentropic bulk moduli are, respectively,

$$K_T=P \tag{86}$$

and

$$K_S=\gamma P. \tag{87}$$

Neglecting compressibility of melt and crystals (i.e., $K_m=K_x=\infty$) and assuming isothermal conditions the speed of sound of a gas-pyroclast mixture can be approximated as

$$c^2\approx\frac{P}{\rho\phi_g}. \tag{88}$$

Note that the ideal gas law can also be expressed in terms of mass and volume fractions of the gas, n_g and ϕ_g, respectively. In other words

$$\rho PV_g=\frac{m_{\text{total}}}{V_{\text{total}}}PV_g=\rho m_{\text{H}_2\text{O}}R_{\text{H}_2\text{O}}T, \tag{89}$$

or

$$\phi_g=\frac{\rho n_g R_{\text{H}_2\text{O}}T}{P}, \tag{90}$$

where $R_{\text{H}_2\text{O}}=462$ J kg^{-1} K^{-1} is the gas constant for H_2O gas. Thus,

$$c\approx\frac{P}{\rho\sqrt{n_g R_{\text{H}_2\text{O}}T}}. \tag{91}$$

MACH NUMBER ISSUES

- Choked flow refers to an upward widening conduit with $M = 1$ at the exit.
- If exit pressure is greater than 1 atm, there will be expansion waves above the vent.
- For a gradually widening conduit it is possible to reach $M > 1$, in which case pressure might drop to below 1 atm, and internal shock (i.e., compression) waves allow the flow velocity to decrease so that the flow exists at 1 atm pressure.

3.3. Temperature

Temperature is calculated by integration of the energy balance, Equation (76), from the base of the conduit at $z = z_0$ to z

$$h = h_0 + \frac{1}{2}\left(u_0^2 - u^2\right) + g\left(z_0 - z\right), \tag{92}$$

where the initial enthalpy, h_0, is calculated for the known pressure, temperature, and composition of the melt using

$$h = m_g h_g + m_m h_m + m_x h_x. \tag{93}$$

Here, h_g, h_m and h_x are the specific enthalpies of the gas, melt and crystals, respectively. Details for calculating these quantities are provided in Appendix A of Mastin (USGS OFR-00-209, 2000).